Surface phenomena associated with thermal cycling of copper and their impact on the service life of particle accelerator structures

Dissertation
zur
Erlangung des Grades
Doktor–Ingenieur

der
Fakultät für Maschinenbau
der Ruhr–Universität Bochum

von
Dipl.-Ing. Dipl.-Ing(FH) Markus Aicheler
aus Tübingen

Bochum 2010

CERN-THESIS-2010-189
17/12/2010

Submitted: 15th November 2010
Defended: 17th December 2010
First referee: Prof. Dr.-Ing Gunther Eggeler
Second referee: Prof. Dr.-Ing Werner Theisen
Third referee: Dr. Stefano Sgobba (CERN)

Preface

I was working on this PhD thesis from 2007 to 2010 mainly in the European Organization for Nuclear Research CERN in Geneva, Switzerland in the Metallurgy Section of the Engineering Department and partly at the Ruhr-University Bochum, Germany in the group of Material Science of the Mechanical Engineering Faculty.

I primarily thank Prof. Dr.-Ing. Gunther Eggeler and Dr. Stefano Sgobba for offering me the possibility of conducting a PhD study on a very interesting topic and in an extremely international and interesting environment. I greatly profited of this chance by developing and improving technical and language skills and by broadening my scientific and, above all, my personal horizon.

My thanks go also to Prof. Dr.-Ing Werner Theisen for remembering me after this long period of absence and his participation in the thesis committee.

For an extremely fruitful and multidisciplinary environment and the funding for my studies I would like to thank the CLIC study at CERN, especially Dr. Walter Wünsch for his broad view and his clever ideas.

My special gratitude goes to all my colleagues from the Ruhr-University for making my stays at the University memorable, in particular Dr.-Ing. Deniz Kurumlu and Dipl.-Ing. Alexander Luithle for excellent scientific, moral, organisational and personal support.

The members of the metallurgy section here at CERN where I spent most of my time, I thank for the support in all professional issues, but above all for making my everyday life a lot more colorful and funny. Here Mr. Alexandre Gerardin has to be named whose good mood is infectious.

Last but not least I thank my parents and my family, all my friends and of course my better half Anne-Laure who all shared good times as well as less good times during the thesis.

"Die Natur verstösst nie gegen ihre eigenen Gesetze"
"Nature never violates her own laws"

Leonardo Da Vinci (1452-1519); engineer, painter, philosopher, medic, architect, writer, visionary, ...

Executive Summary

The performance of accelerating structures (AS) in the Compact LInear Collider (CLIC) is sensitive to a variety of parameters, including the surface quality of key elements of the AS. Processes which affect the surface quality are therefore of particular concern. The present work addresses surface modifications associated with thermal cycling during operation. This type of operating condition represents a specific type of fatigue loading.

Four fatigue test procedures were used in the present study in order to investigate the fatigue behaviour of oxygen–free–electronic (OFE) copper, the candidate material of the CLIC–AS: conventional fatigue (CVF), ultrasonic swinger (USS), laser fatigue (LAF) and radio–frequency fatigue (RFF). During operation of the accelerator the material of the AS will be subjected to cyclic temperature changes of approx. Δ T = 56 K, from about 40° C to about 100° C. These temperature changes will result in cyclic biaxial strains in the surface of the order of $\Delta\epsilon_{biax} = 9.2$ x 10^{-4} at a macro equivalent stress of 110 MPa.

Characterisation and quantification of roughening and hardening phenomena on cycled samples revealed a strong dependence on the orientation of individual grains of the polycrystalline material. Orientation imaging with a scanning electron microscope showed that roughness and hardness increased less in grains oriented in [1 0 0] direction than grains oriented in the [1 1 0] direction, with the [1 1 1] grains falling in between. A detailed analysis of the slip systems of the different orientations clarified the origin of the roughening phenomena and their dependence on crystallographic orientation. This dependence arises from the different number of active slip systems. Additionally, grain boundaries need to be considered in fine structures (grain sizes as fine as 1 μm – 5 μm). High local stresses related to elastic anisotropy in the polycrystal average out on the macroscopic scale.

Analysis of the results obtained by different fatigue test techniques indicates that similar elementary processes govern the material response in all cases. The two mechanical loading methods CVF and USS have experimental advantages in terms of standardisation and in terms of the capability of addressing high cycle numbers. Unfortunately, the results obtained cannot be directly related to thermal fatigue data obtained by LAF and RFF.

Given the importance of electrical conductivity for the CLIC AS material, copper is the only material that comes in to consideration. On the basis of the results obtained in the present study, the two possible candidates for the material are:

1) A strongly textured and fine grained OFE copper, e.g. equal–channel–angular–pressed (ECAPed) OFE copper.

2) A strongly [1 0 0] orientation textured pure copper thin film.

Either material would offer fatigue characteristics that should be compatible with the demanding requirements of the CLIC–AS.

The results obtained in the present study provide a framework for discussing material selection and material pretreatments, developing alternative engineering designs and working out monitoring strategies for long–term operation of the CLIC–AS.

Contents

1. Introduction **1**

2. State of the Art **3**

2.1. A Brief Description of the Compact Linear Collider (CLIC) . . . 3
2.2. Copper: Facts and Figures 7
2.3. Fatigue 10
    2.3.1. Fatigue in Single Crystals by Single Slip 12
    2.3.2. Fatigue in Single Crystals by Multiple Slip 13
    2.3.3. Fatigue in Polycrystals 13
    2.3.4. Different Fatigue Regimes and the Fatigue Limit 15
    2.3.5. Role of Surfaces for Crack Initiation 17
2.4. Thermal Fatigue 18

3. Motivation and Objectives **21**

4. Experimental **23**

4.1. Material and Characterisation 23
    4.1.1. Heat Treatments of Oxygen–Free–Electric Copper 23
    4.1.2. Surface Finishing 25
    4.1.3. Cleaning Procedure for Vacuum Heat Treatments 26
    4.1.4. Tensile and Compression Testing 27
    4.1.5. Macrohardness 27
    4.1.6. Electrical Conductivity 28
4.2. Surface Analysis 29
    4.2.1. Metallography and Optical Microscopy 29
    4.2.2. Roughness Analysis 29
    4.2.3. Orientation Imaging in Scanning Electron Microscopy . . 30

4.2.4. Local Hardness 31
4.3. Copper Coatings 32
4.3.1. Fabrication 33
4.3.2. X-Ray Diffraction 35
4.4. Fatigue Test Benches 40
4.4.1. Conventional Fatigue (CVF) 40
4.4.2. Ultrasonic Swinger (USS) 41
4.4.3. Laser Fatigue (LAF) 44
4.4.4. Radio Frequency Fatigue (RFF) 47

5. Results 51

5.1. Morphology of Fatigue Modified Surfaces 51
5.1.1. Morphology after Laser Fatigue 51
5.1.2. Morphology after Radio Frequency Fatigue 55
5.1.3. Morphology after Ultrasonic Cycling 57
5.1.4. Fatigue Induced Roughness versus Grain Orientation . . 59
5.1.5. Morphology of Surface Features near Grain Boundary . . 63
5.2. Fatigue–Induced Hardening 65
5.2.1. Hardness as a Function of Cycle Number 66
5.2.2. Hardness as a Function of Max. Equivalent Strain 67
5.2.3. Hardness as a Function of Grain Orientation 69
5.3. Combined Roughening and Hardening 70
5.3.1. Roughening and Hardening as a Function of Cycle Number 70
5.3.2. Roughening and Hardening as a Function of Grain Orientation 71
5.4. Thin Film Characterisation 73
5.4.1. Grain Size Measurements 73
5.4.2. Texture Analysis 75
5.5. Fatigue Data 78
5.5.1. Thin Films 78
5.5.2. Bulk Material 79

6. Discussion **81**

- 6.1. Comparison of Different Fatigue Test Procedures 81
  - 6.1.1. Load Ratio Dependency 81
  - 6.1.2. Type of Loading 82
  - 6.1.3. Stress States 84
  - 6.1.4. Cycling Frequencies: Low versus High 86
  - 6.1.5. Surface Degradation as a Function of Grain Orientation and Effects of Grain Boundaries 87
- 6.2. Fatigue Effects 89
  - 6.2.1. Fatigue Induced Roughness and Crystallographic Orientation 89
  - 6.2.2. Grain Size and the Effect of Grain Boundaries 92
  - 6.2.3. Fatigue Induced Hardening 95

7. Summary and Conclusions **97**

Bibliography **99**

List of Figures **113**

List of Tables **121**

A. Appendix **123**

- A.1. Schmid Factors 124
- A.2. Thin Film Characterisation 129

Nomenclature

Acronyms

AS	Accelerating Structure
ATLAS	A Toroidal LHC ApparatuS
BCC	Body–Centered–Cubic
BDS	Beam Delivery System
c.m.	center–of–mass
CERN	European Organization for Nuclear Research
CLIC	Compact Linear Collider
CMS	Compact Muon Solenoid
CVF	Conventional Fatigue
EBSD	Electron–Back–Scattered–Diffraction
ECAP	Equal–Channel–Angular–Pressing
ECC	Electron–Channeling–Contrast
EP	Ending Point damage criterion
FCC	Face-Centered-Cubic
FEM	Finite Element Method
GB	Grain Boundary
H02	Half hard temper according to ASTM B601 [1]

HCF	High-Cycle-Fatigue
HEP	High-Energy-Physics
HV	Vickers Hardness
IACS	Inernational Annealed Copper Standard
ILC	International Linear Collider
IP	Interaction Point
KEK	High Energy Research Organization Japan
LAF	Laser Fatigue
LCF	Low-Cycle-Fatigue
LEP	Large Electron–Positron Collider
LHC	Large Hadron Collider
LINAC1	Linear Proton Accelerator 1
LINAC2	Linear Proton Accelerator 2
LINAC4	Linear Proton Accelerator 4
MUD	Multiples of Uniform Distribution
OFE	Oxygen Free Electronic
PDF	Powder Diffraction File
PETS	Power Extraction and Transfer Structures
PS	Proton Synchrotron
PS-B	PS Booster
PSB	Persistent Slip Band
PVD	Physical Vapor Deposition

RF	Radio Frequency
RFF	Radio Frequency Fatigue
RT	Room Temperature
S–N	Stress–Number of cycles
SB	Slip Band
SEM	Scanning–Electron–Microscopy
SF	Schmid Factor
SLAC	Stanford Linear Accelerator Center
SP	Starting Point damage criterion
SPS	Super Proton Synchrotron
TBA	Two–Beam Acceleration
TEM	Transmission–Electron–Microscopy
TERA	Fondanzione per Adroterapia Oncologica
UHCF	Ultra-High-Cycle-Fatigue
USS	Ultrasonic Swinger
VSI	Vertical Scanning Interferometry
XRD	X–Ray Diffraction

Greek Symbols

ϵ_{eq}	Equivalent Von Mises strain	m/m
κ	Electrical conductivity	MS/m
λ	Wavelength	m
τ	Penetration depth X-Ray beam	m

θ	Angle between incident beam and sample	°

Latin Symbols

a	Lattice parameter	m
A_{deff}	Effective diffusion area	cm^2
D	Diffusion Coefficient	cm^2/s
D_0	Temperature independent constant	cm^2/s
d_{eff}	Effective penetration depth	mm
f	Frequency	Hz
$f_{hkl_{film}}$	Fraction diffracted by the film	-
G	Shear Modulus	GPa
I'_{hkl}	Integrated intensities randomly oriented sample	-
$I_{hkl_{bulk}}$	Integrated intensity from bulk	-
$I_{hkl_{FCcorr}}$	Corrected integrated intensity	-
$I_{hkl_{MIcorr}}$	Corrected integrated intensity	-
I_{hkl}	Integrated intensities textured sample	-
Q	Activation Energy	cal/mol
R	Load Ratio	-
R_g	Ideal gas constant: 8.31	J/K·mol
Ra	Roughness Parameter	μm
Rz	Roughness Parameter	μm
SI	Surface Index	-
T	Absolute Temperature	K

T_{hkl}	Texture Index	-
N_{gl}	Stress exponent for slip	-

1. Introduction

The Compact Linear Collider (CLIC) is an electron–positron collider for energies of 1.5 TeV – 3 TeV, currently under study at the European Organization for Nuclear Research (CERN) in Geneva [2, 3]. It is considered as a possible successor for the Large Hadron Collider (LHC) [4]. Its task will be to conduct experiments to validate and improve precision of LHC data by colliding elementary electrons and positrons. The planned accelerating gradient of 100 MV/m will be the highest ever achieved in non–superconducting accelerating cavities [5]. This extremely high gradient is required to minimise the costs for expensive underground civil engineering for the accelerator construction [6]. The accelerating fields for the particles are induced in the Accelerating Structures (AS) by high–intensity pulsed Radio Frequency (RF) waves. Materials used for the AS are subject to pulsed surface heating arising from the electrical currents induced by the RF fields. Since CLIC will operate at room temperature, good electrical conductivity of the AS material is of paramount importance [5]. Pure electrical copper, an excellent, commercial electrical conductor has therefore been chosen as the baseline material for the AS. The drawback of this type of pure copper, however, is its low mechanical strength. For CLIC, a specific high fatigue strength is needed to prevent surface degradation arising from pulsed surface heating. A technical solution is needed for CLIC which takes these two demands into account [7].

For the electrical and mechanical properties of pure copper, the maximum pulsed temperature rise expected is calculated as $\Delta \mathrm{T} = 56$ K and the resulting thermal strain $\Delta\epsilon_{th} = 9.2 \text{ x } 10^{-4}$ [5]. CLIC is designed to operate for 20 years, 9 months a year, 7 days a week and 24 hours a day. At a frequency of 50 Hz, the total amount of pulses will exceed 2.3 x 10^{10} [8]. This cycle number is at the limit of classical engineering fatigue studies, which extend normally up to a number of cycles of 10^7 [9]. Very little data for higher cycle numbers (Ultra-High-Cycle-

Fatigue (UHCF) for copper can be found in the literature. Only in the past few years has the UHCF regime become a topic of scientific and engineering interest [10]. It is believed that fatigue mechanisms known in classic regimes (Low-Cycle-Fatigue (LCF) and High-Cycle-Fatigue (HCF)) change if loads are further decreased and cycle numbers increased. Since it is known that in HCF and UHCF the limiting factor for fatigue life is crack initiation rather than crack propagation [11], microstructural and morphological surface processes play a major role for the fatigue performance of the CLIC AS.

In the present work the term fatigue is used in a broad sense. We consider not only mechanical failure due to the initiation and growth of cracks, leading to rupture, but rather all elementary processes which degrade the performance of the CLIC AS as a result of cyclic loading. When thermomechanical cycling affects the functionality of an electromagnetic device we may also use the term functional fatigue. This is analogous to functional fatigue in shape memory alloys [12].

Current CLIC operating parameters envisage a RF frequency of 12 GHz [5, 8]. In copper, the resulting skin depth [13], a measure of the penetration depth of the electromagnetic field into the material, is 0.6 μm. Since the associated surface currents are sensitive to surface defects and roughness, the initial general surface quality requirements are set at Ra = 0.02 μm [5]. As the probability of electrical breakdown in the high fields of the AS is sensitive to the presence of surface features, which may evolve over time, serious performance limiting issues can arise from any deterioration in surface quality. Surface fatigue, hence evolution of roughness during thermal cycling, is therefore considered as a critical long–term issue for the AS of CLIC. Thus it is important to understand the behaviour of pure copper surfaces under these specific operating conditions.

In this study, copper will be tested using four different fatigue methods.The aim of the present work is to use the understanding obtained from the mechanical and microstructural fatigue test program for improvements in three areas: materials selection and material pretreatments, design procedures and surveillance methodologies.

2. State of the Art

This chapter introduces the present knowledge and understanding on which the current study is based on. It starts with an overview of CLIC and its AS. Next, it provides a brief historical introduction on the use of pure copper for particle accelerators as an introduction to challenges and restrictions that apply to the material selection for the CLIC AS. A review of fatigue research in general is specifically followed by an introduction to thermal fatigue.

2.1. A Brief Description of the Compact Linear Collider (CLIC)

CLIC is a planned high-energy (0.5 TeV – 3 TeV center–of–mass (c.m.)) and high-luminosity (10^{34} – 10^{35} cm^{-2}s^{-1}) positron–electron collider [3, 6]. It is intended as a possible successor to the Large Hadron Collider (LHC) [4], which is currently pushing the energy limit with proton collisions at 7 TeV c.m., heralding a new area of High-Energy-Physics (HEP). Experiments performed by colliding elementary particles, such as electrons and positrons, allow much higher precision to be obtained in describing the energy and position of the colliding particles and collision products, compared to non–elementary particles like protons in the LHC [14]. For the field of HEP, hadron colliders therefore traditionally alternate with lepton colliders: the hadron machines open up new energy regimes, while lepton machines are used to confirm results and make more precise measurements. Since the events being studied are extremely rare, a very high integrated luminosity is needed [15]. The physics experiments in CLIC (multi–layer particle detectors similar to “A Toroidal LHC ApparatuS” (ATLAS) [16] or the “Compact Muon Solenoid” (CMS) [17] in LHC) thus require a luminosity of at least 10^{34} cm^{-2}s^{-1} at 1 TeV c.m., which CLIC must deliver.

CLIC is based on the Two–Beam Acceleration (TBA) method [6]. Energy from the drive beam, a low-energy, high-intensity electron beam, is extracted and converted to RF power with the help of Power Extraction and Transfer Structures (PETS) and fed to active sections of the main linear accelerator, where it imparts a high energy to a passing bunch of accelerated particles [18]. The overall layout of CLIC is shown in Fig. 2.1. At the Interaction Point (IP), the beams collide in the center of a particle detector. Given a c.m. energy of 3 TeV, an accelerating gradient of 100 MV/m and a length of 5.5 km for the Beam Delivery System (BDS), CLIC would cover a total length of approx. 48.3 km [8, 18]. The big advantage of the TBA scheme is its relative compactness: since no active components such as modulators or klystrons are necessary along the machine, both linear accelerators can be housed in a single small–diameter tunnel as shown in Fig. 2.2, significantly reducing the need for underground civil engineering.

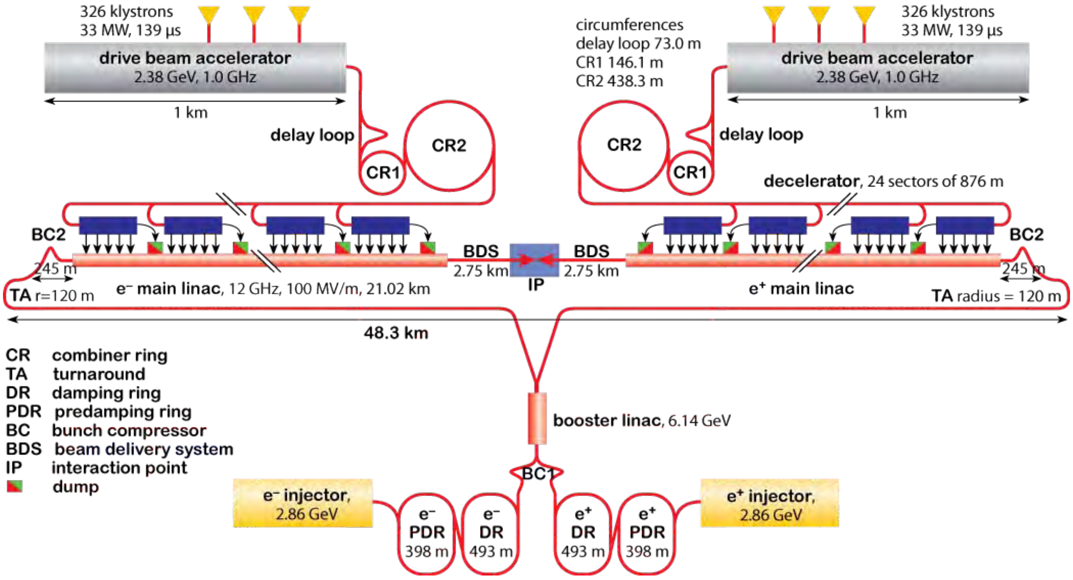
326 klystrons
33 MW, 139 μs
drive beam accelerator
2.38 GeV, 1.0 GHz
1 km
delay loop
CR2
CR1
circumferences
delay loop 73.0 m
CR1 146.1 m
CR2 438.3 m
326 klystrons
33 MW, 139 μs
drive beam accelerator
2.38 GeV, 1.0 GHz
1 km
CR2
CR1
delay loop
decelerator, 24 sectors of 876 m
BC2
245 m
TA r=120 m
e⁻ main linac, 12 GHz, 100 MV/m, 21.02 km
BDS
2.75 km
IP
BDS
2.75 km
e⁺ main linac
BC2
245 m
TA radius = 120 m
48.3 km
CR combiner ring
TA turnaround
DR damping ring
PDR predamping ring
BC bunch compressor
BDS beam delivery system
IP interaction point
dump
booster linac, 6.14 GeV
BC1
e⁻ injector, 2.86 GeV
e⁻ PDR 398 m
e⁻ DR 493 m
e⁺ DR 493 m
e⁺ PDR 398 m
e⁺ injector, 2.86 GeV

Figure 2.1.: Overall layout CLIC 3 TeV. Generation, acceleration and delivery of the main beams in the lower half. The drive-beam complex and the production of 12 GHz RF–power are situated in the upper half [3].

Among the different technological solutions for building a linear collider, the

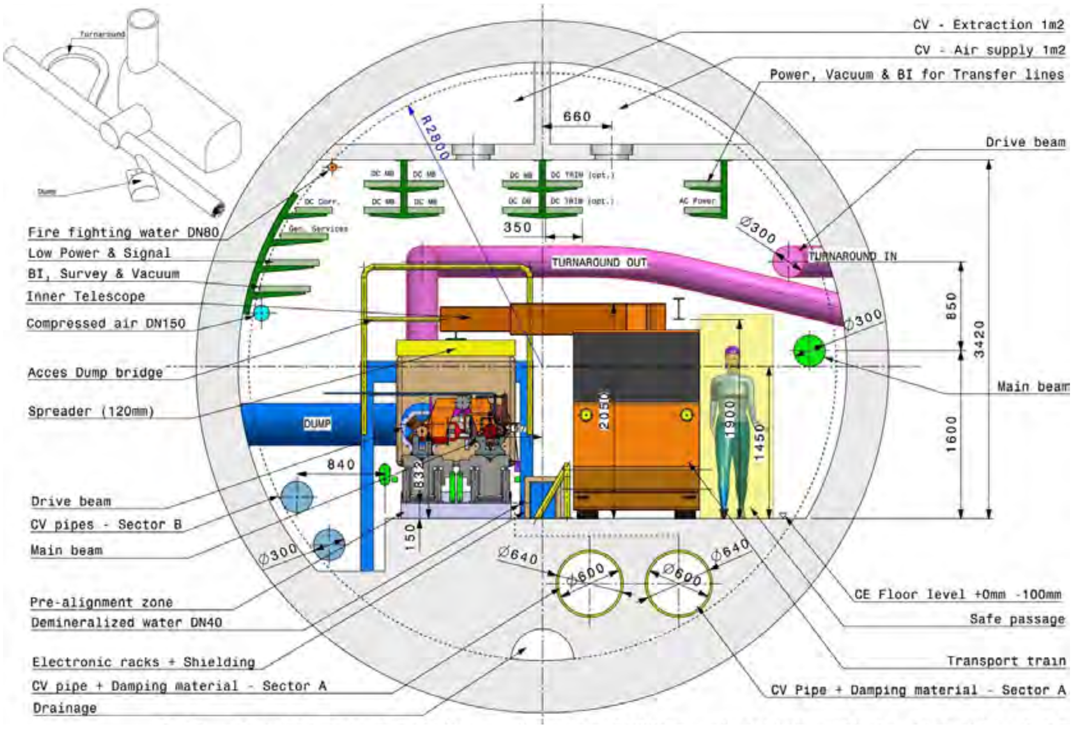
Turnaround
Dump
CV - Extraction 1m2
CV - Air supply 1m2
Power, Vacuum & BI for Transfer lines
Drive beam
660
R2800
DC MB
DC MB
DC MB
DC MB
DC MB
DC TRIM (opt.)
DC DB
DC TRIM (opt.)
AC Power
DC Corr.
Gen. Services
350
Ø300
TURNAROUND OUT
TURNAROUND IN
Fire fighting water DN80
Low Power & Signal
BI, Survey & Vacuum
Inner Telescope
Compressed air DN150
Ø300
850
3420
Main beam
Acces Dump bridge
Spreader (120mm)
DUMP
2050
1900
1450
1600
840
832
Drive beam
CV pipes - Sector B
Main beam
150
Ø300
Ø640
Ø600
Ø600
Ø640
Pre-alignment zone
Demineralized water DN40
CE Floor level +0mm -100mm
Safe passage
Electronic racks + Shielding
Transport train
CV pipe + Damping material - Sector A
CV Pipe + Damping material - Sector A
Drainage

Figure 2.2.: Proposed CLIC tunnel cross section. The main beam linac and the drive beam are installed on individual girders on a common concrete base. Transfer lines carry the main- and drive-beams from the generation complexes to their respective injection points and connect cooling and ventilation facilities [19].

CLIC study explores the technical feasibility of TBA using high–frequency, room–temperature, traveling–wave accelerating structures. In contrast, the International Linear Collider (ILC) study uses the known Tesla–Technique [20], based on klystron–fed superconducting niobium cavities operating at cryogenic temperatures [21]. This technique is currently limited to c.m. energies of 500 GeV due to the complexity of the power delivery system, while CLIC is not subject to those limitations and currently designed for 3 TeV. The two communities are collaborating closely to find the most suitable solution for the HEP community. Depending on the physics discoveries from the LHC, a choice will have to be made as to which of the accelerators will be built.

The CLIC AS must meet a complex set of demanding interrelated criteria as a high–performance, cost–effective linear collider design. Fig. 2.3 shows a sketch of a part of an AS consisting of joint discs, machined to 2 μm – 4 μm dimensional tolerance and with a surface roughness of $Ra = 0.002$ μm. The irises where the highest electric fields accelerate the passing particle beam are visible in the cut–out. The present CLIC parameter set [5, 8] specifies that accelerating structures operate at 100 MV/m accelerating gradient in the presence of the particle beam (called loaded gradient) with a maximum allowed electrical breakdown rate in the order of 10^{-7} (per structure) at a pulse length of 240 ns. The performance limiting factor is the breakdown rate. Raising either the accelerating gradient or the pulse length would make the machine more compact and increase luminosity, but it would also increase the breakdown rate. When a breakdown occurs, the beam is lost and the AS suffers damage, both from particle impacts and from the breakdown itself. This risk must minimised to avoid critical damage to the accelerator and to ensure the specified luminosity of 10^{35} cm^{-2}s^{-1} to be maintained. However, the main effect that limits the lifetime of the AS is fatigue damage caused by pulsed surface heating. The severity of damage is determined by the surface magnetic field, pulse length and material properties.

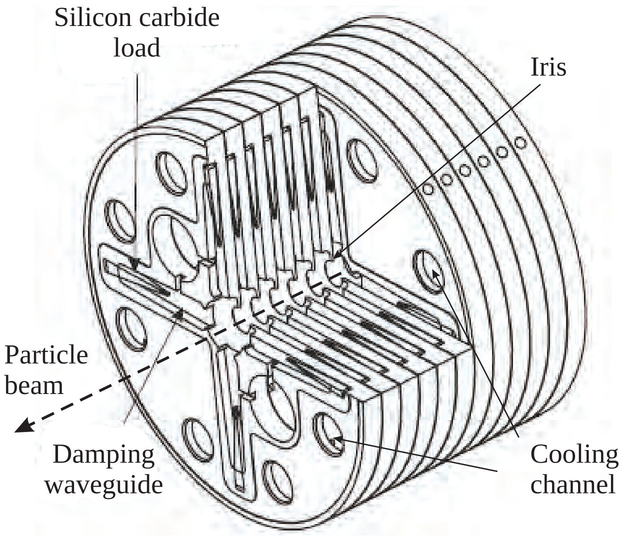

Figure 2.3.: Scheme of AS consisting of brazed discs. Bunches of particles are accelerated by the RF fields and pass in center of irises. The particle beam induces wake fields, which are transported away from the center by the damping wave guides and are damped in the silicon carbide loads [3].

This effect is addressed in the current study.

Past experience and understanding do not provide a satisfactory explanation of how the evolving surface roughness caused by thermal cycling degrades the Quality Factor (Q-factor) of the AS. In general, the Q-factor describes the damping characteristics of a resonator [22]. A high Q-factor means that the waveform decay in a resonator is small (low damping) and it can therefore oscillate longer. For the CLIC AS, a high Q-factor is a requirement based on beam dynamics simulations.

Surfaces exposed to thermal cycling caused by RF–fields can develop increasing roughness which may contribute to electrical breakdown [23]. This phenomenon is a key point of interest of other CLIC–related studies [24, 25, 26]. Also here, past experience and understanding do not provide a satisfactory explanation to which extent the developing surface roughness decreases breakdown resistance of a material. Both effects, Q-factor sensitivity and breakdown resistance, as the result of fatigue induced by pulsed surface heating, are considered as a critical long–term performance limiting issue and are currently being studied.

2.2. Copper: Facts and Figures

Pure copper is one of the oldest materials used by mankind [27], with the earliest estimates of its use going back to 9000 B.C. in the Middle East [27]. It was the first metal to be smelted from ore, and was later alloyed with zinc and tin. Its excellent electrical and thermal conductivity and extremely high ductility are the main reasons for its extensive use in modern society [28].

In particle accelerator development at CERN, copper has always been a mainstay of accelerator construction. In the late 1950's, the first Linear Proton Accelerator (LINAC1), sending protons of the energy of 50 MeV to the Proton Synchrotron (PS), was based on accelerating structures (drift tubes) made of copper. In the 1970's, LINAC2 provided protons to the PS Booster (PS-B) at 800 MeV with an acceleration gradient of 2.5 MV/m. The accelerating components of LINAC2 were made of copper, whereas those of PS were made of copper–plated stainless steel. The steel substrate was necessary because of the forces arising from large–diameter accelerating cavities under vacuum, while the copper was used for its superior electrical conductivity. During the same time the Super Proton Synchrotron (SPS) was opening a new field of physics, reaching a particle energy of 450 GeV. Its copper accelerating cavities accelerated the protons by 3 MeV at each turn. In the 1980's, superconducting accelerating cavities made of niobium–coated copper were developed specially for the Large Electron–Positron Collider (LEP) [29]. The big advantage of this technology compared to bulk niobium structures was its significantly higher thermal stability, due to the higher thermal conductivity of the copper substrate compared to niobium [30]. The same technology is also used in the LHC accelerating cavities [31]. Of the projects currently under way at CERN, LINAC4 [32] and the medical accelerator project of "Fondazione per Adroterapia Oncologica" (TERA) [33] are technologically closest to the CLIC concept. The accelerating cavities of LINAC4 are currently in the prototype phase and will be made of bulk OFE copper, with a comparatively low accelerating gradient of 4 MV/m. The bulk copper cavities used in the TERA's project will have a much higher accelerating gradient (40 MV/m). Though it is still far below that planned for CLIC, it will nonetheless possess a significant challenge in terms of breakdown risk due to it extremely hight surface electric fields.

Table 2.1 shows the electrical conductivities in %IACS (Inernational Annealed Copper Standard) and thermal conductivitys for different pure metals and alloys. Since pure copper possesses an extremely high electrical conductivity, it is used as the reference and is the most common material in numerous applications, including electrical applications like cables or integrated circuits [35, 36]. Furthermore, it is classically used in non–cryogenic RF applications, where electrical losses play a major role [7]. Its low yield strength and ductile behaviour are also useful for the manufacturing of numerous components of particle accelerators.

The mechanical properties of high–purity copper can be enhanced by work hardening and alloying. The increase in dislocation density through work hardening only marginally influences its electrical and thermal conductivity at room temperature [34, 37]. The electrical conductivity of copper is also independent of the crystallographic orientation and does not vary significantly with grain size [34, 38]. Applications which, in addition to the high electrical conductivity of pure copper, also demand enhanced mechanical properties are based on cold

Material	El. cond. / %IACS	Th. cond. / W/m·K
Pure silver	106	428
Pure copper (99.999 w% Cu)	103	398
C10100 (oxygen-free electronic, OFE)	101	391
C15000 (Cu with 0.10 w%–0.20 w%Zr)	93	367
C15700 (dispers.–strength. with 0.15 w% Al_2O_3)	93	360
Coin silver (90 w% Ag + 10 w% Cu)	85	
Pure gold	73.4	318
Pure aluminum	65	247
Pure nickel	25.2	83
Pure iron	17.6	80

Table 2.1.: Electrical and thermal conductivity values for various metals and alloys (from [34]).

rolled or cold forged pure copper. Any heating cycle suffered during manufacturing (e.g. brazing) would degrade these properties, making other hardening methods necessary. For example, alloying pure copper with a limited amount of zirconium (0.05 w% – 0.15 w%) enhances its mechanical properties through solid solution hardening and precipitation hardening. The enhanced mechanical properties, along with a possible coldworking step, can then resist exposure to medium temperatures (e.g. 450 °C in low–temperature brazing) for short times (up to several hours) through dislocation pinning at the precipitates [39]. Higher temperatures (e.g. 825 °C in high–temperature brazing) make it necessary to use thermo–mechanical stable phases (e.g. dispersoids in alumina strengthened copper [39]) to enhance the mechanical properties of pure copper. Fig. 2.4 shows the yield strength at room temperature (RT) of pure copper and two high electrical conductivity copper alloys, exposed to various temperatures for one hour. It can be seen that cold–worked copper softens significantly already at temperatures as low as 300 °C, whereas cold–worked copper zirconium alloy keeps its strength up to 550 °C. Most notably, the dispersion strengthened copper GlidCop© softens only slowly at temperatures higher than 700-800 °C.

The major drawback to the use of alloyed copper is the dramatic deterioration

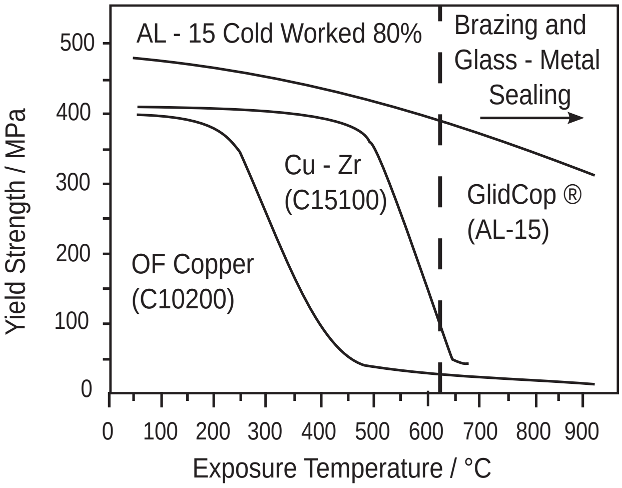

Figure 2.4.: Softening resistance of GlidCop Al-15© (C15700) versus cold-worked OF copper and cold–worked Zirconium Copper. Properties measured at RT, after exposure to elevated temperatures for one hour. From [39]

of electrical conductivity [34]. Fig. 2.5 shows how electrical conductivity falls off for various alloy elements and proportions at room temperature. While the effect varies widely from element to element, even silver, with its higher electrical conductivity, has a negative effect.

Copper is a Face-Centered-Cubic (FCC) metal. As with all cubic materials, the symmetries of the elementary cell mean that all properties which can be described with a second rank tensor are isotropic [38]. Accordingly, the electrical conductivity, the thermal conductivity and the thermal expansion coefficient are independent of crystallographic orientation [38].

2.3. Fatigue

Fatigue is generally referred to as material degradation related to cyclic loading. Irreversible processes inside the material, particularly at the microstructural level, cause "fatigue damage". ASTM Standard E1823 defines fatigue of materials as follows [40]: "Fatigue – the process of progressive localized permanent structural change occurring in a material subjected to conditions that produce fluctuating stresses and strains at some point or points and that may culminate

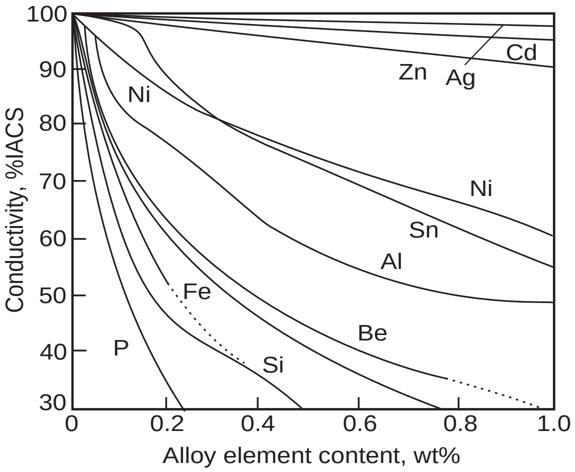

Figure 2.5.: Influence of alloying element and content on electrical conductivity of pure copper. From [34]

in cracks or complete fracture after a sufficient number of fluctuations."

When a material is loaded beyond the elastic limit, plastic deformation occurs through the creation and motion of dislocations. Dislocations are 1–dimensional crystal lattice line–defects and represent carriers of plastic deformation in crystalline materials. Under cyclic loading, the dislocations in the crystal move. Further plastic deformation then requires that either formerly pinned dislocations be freed or new dislocations be produced, whereby in the second process the dislocation density increases. Classically, the deformed material increases in hardness during loading, while ductility decreases. At the end of fatigue life, the dislocation density in the cycled material becomes so high that dislocations strongly hinder each other and therefore dislocation motion is almost impossible [41].

This simplified approach does not explain all phenomena observed in relation with cyclic loading. For example when cyclic loads remain below the elastic limit, the macro deformation remains elastic. Nevertheless it is believed that irreversible processes take place at regions of local stress/strain concentrations, in the form of microplasticity at a very local scale ($\leq 1\ \mu$m). These regions are prone to initiate failure and are normally located around inhomogeneities, either withing in the lattice (inclusions or accumulation of dislocations) or at the surface (geometrical stress enhancement factor) [41].

2.3.1. Fatigue in Single Crystals by Single Slip

When observing the fatigue behaviour of single crystals, the above mentioned processes can be shown experimentally very clearly with the help of Transmission–Electron–Microscopy (TEM) and Scanning–Electron–Microscopy (SEM) with Electron–Channeling–Contrast (ECC) [42].

For pure copper single crystals, Zhang et al. [43] and Hirao et al. [44] showed that cyclic stress far below the elastic limit can cause microplasticity due to local dislocation activity, while the signs of accumulated damage are hardly visible on the surface. After a certain incubation time, the dislocations create so much internal stress through pile–up, that small intrusions and extrusions evolve on an initially smooth surface [41]. These intrusions and extrusions represent locations where stresses are concentrated, and therefore dislocation motion is favored. The sites where this self–enhancement of microplasticity takes place are therefore preferred locations for crack initiation [45]. The deformation through dislocation motion is generally possible only on the easy slip planes (e.g. for copper, the four (1 1 1)–type planes) in three different directions of the [1 1 0]–type [46]. The 12 possible combinations of slip planes and slip directions are called slip systems. Depending on how samples are oriented with respect to the loading axis, different fatigue behaviour can be expected. When single crystals are oriented for single slip (meaning, only one slip system will be active in the crystal), fully reversed cyclic loading produces approximately equal numbers of positive and negative edge dislocations [47, 48]. As these dislocations are able to move only on one active slip system, positive and negative dislocations can attract one another and form dislocation dipoles [41]. This process can be observed externally by examining the stress–strain curves, where hysteresis indicates cyclic hardening. The networks of these edge dislocation dipole arrangements are called veins, while the low–dislocation regions between the veins are called channels [49]. Through further cycling, the strain accommodation capacity of the vein structure becomes saturated and a structural change has to take place in the matrix. The vein structure transforms into a wall structure of a Persistent Slip Band (PSB), which may propagate through an entire crystal [41].

2.3.2. Fatigue in Single Crystals by Multiple Slip

If a single crystal is oriented for multiple slip, the developing dislocation substructure changes [50]. The same effect is observable for single slip orientation when the plastic strains get large and secondary slip plays a more pronounced role. More complex arrangements of the edge dislocation dipoles develop due to their accumulation, which is now possible on more than one slip system. The resulting networks are generally referred to as labyrinth and cell structures [51]. In particular, the labyrinth structure is known to harden cyclically faster, to be more stable on a larger number of cycles and to be able to accommodate higher imposed plastic strains with reversible dislocation motion when compared to the vein structure [41].

However, the reported experimental results are contradictory. Thus, Hoeppner and Salviar [52] performed fatigue tests with uniaxial loading of copper single crystals. They varied the angle between the primary slip system ((1 1 1) plane, [-1 1 0] direction) and the principal loading axis. Different samples were tested under the same uniaxial stress. Due to different Schmid Factors (SF), different shear stresses acted on the primary slip systems. They found that the samples with lower shear stress had a much longer fatigue life than those under higher shear stresses. Some years later, Cheng and Liard [53, 54] stated that uniaxial fatigue tests performed under plastic strain control on copper single crystals cycled under different Q–factors (defined as the ratio of the SF of the secondary slip system to that of the primary one) did not show any difference in fatigue life within the experimental error margin. Results on polycrystalline copper obtained in the current study and presented in Chap. 5.1.4 show that grains of particular grain orientations behave differently when subjected to the same loading cycles.

2.3.3. Fatigue in Polycrystals

Far from being single crystals, ordinary technical materials are polycrystalline, so a huge variety of slip orientations is present in the material. Grain Boundaries (GB) represent defects in the crystal lattice and therefore strongly influence the dislocation motion in their direct vicinity, depending on the crystallographic orientation of the adjacent grains. Two studies experimentally showed this role of GB in polycrystalline copper submitted to fatigue [45, 50]. Large–angle GB are known to be obstacles to dislocation motion. During cycling, a pileup of dislocations at these GB can induce high local stress concentrations and therefore promote crack initiation. In contrast, low–angle GB represent less severe obstacles for dislocations, and are therefore considered less critical [41, 45, 50].

Although the presence of GB and other lattice defects, such as precipitates or impurities, can significantly change the mechanisms of the material's response to cyclic deformation, the considerations noted for the fatigue behaviour of single crystals can generally be applied to cyclic deformation of near–surface grains of metals of high purity [41]. The formation of PSB can be observed, as in single crystals, but with the significant difference that PSB can cross low–angle GBs whereas large–angle GBs are impervious to them. Under certain conditions, dislocation substructures, such as labyrinth and cell structures, can be observed, as with single crystals [41]. Additionally, the deformation continuity condition at GBs can create locally multi–axial loading with different stress levels. Thus, multiple slip can arise due to different deformation responses between adjacent grains. For materials with fine grain structure, this behaviour can be predominant. For materials with coarse grain structure, where the majority of the grains is not perfectly oriented for multiple slip, a single crystal behaviour, oriented for single slip, can be assumed [41].

In contrast to single crystals, in polycrystalline metals the Bauschinger effect can be observed. In 1886, Bauschinger found experimentally that in polycrystalline material, submitted to a certain amount of forward plastic deformation (in tension or compression), the yielding of the material takes place earlier when the loading direction is reversed than for continued forward deformation [55]. Grains oriented with a high SF deform plastically first and therefore harden through production and arrangement of dislocations. Other grains with lower SF follow later and undergo therefore a lower plastic deformation. When the load is reversed, the grains which deformed first are already stress free before traversing the macro zero strain level because of residual plastic deformation. The yielding of these grains will then occur at a lower macroscopic stress level than in the forward deformation direction. The macro behaviour of the polycrystal shows therefore a higher yield strength in tension as compared to compression if the first loading direction was tension. The Bauschinger effect will be discussed further with respect to the results of the current study on pure polycristalline copper in Chap. 6.1.1.

2.3.4. Different Fatigue Regimes and the Fatigue Limit

Woehler, in 1860, was the first to systematically acquire and analyse fatigue data. He performed rotation–bending tests and plotted the points of rupture in a diagram of stress–amplitude versus the number of cycles to failure, which he used to predict the fatigue behaviour of different steels for railroad wheel applications. This way of illustrating fatigue data is the basis of most of the fatigue considerations today. The diagram is named after its inventor and often also referred to as Stress–Number of cycles (S–N) plot.

Depending on the stress/strain level and the resulting fatigue cycle numbers, a general distinction between different regimes of fatigue mechanisms is made. Fig. 2.6 shows a generalised S-N plot. High loads with severe plastic deformation result in low cycle number to failure. This regime is called Low–Cycle–Fatigue (LCF). High–Cycle–Fatigue (HCF) is the regime characterised by cycle num-

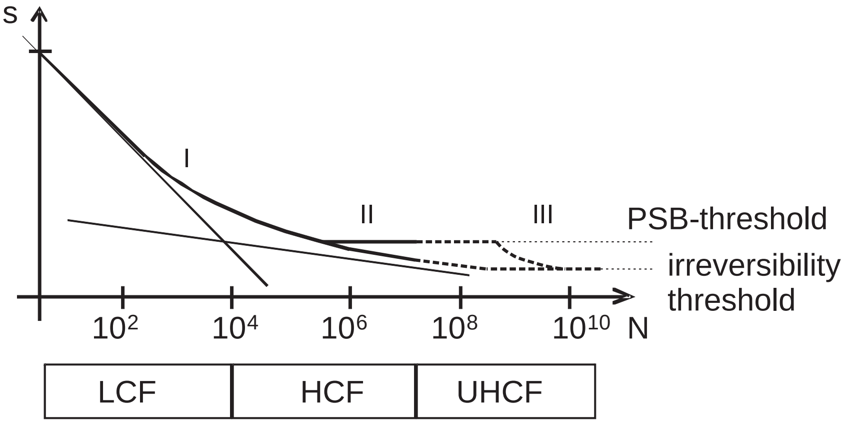

Figure 2.6.: Determination of the different fatigue regimes in S-N Woehler plot according to [11]. Material with or without a plastic strain fatigue limit in the HCF regime (range II), terminated by a further decrease of fatigue life with decreasing strain amplitude below the PSB-threshold in the UHCF regime (range III).

bers above 10^4 under predominantly elastic strains. This regime ends at 10^7 cycles under classical engineering approaches. Toward the end of this regime, a continuously decreasing trend can be observed. This gives rise to the idea that even if the stress is reduced further, the material will undergo failure at a certain number of cycles. The stress corresponding to a cycle number of 10^7 is therefore commonly referred to as the fatigue strength of a material. In contrast, it was found that some materials show a flat behaviour rather than this continuous decrease toward 10^7 cycles. The corresponding stresses are called fatigue limits. It was expected that cycling these materials at stresses below the fatigue limit would not accumulate damage. Generally, it is observed that Body–Centered–Cubic (BCC) materials show fatigue limits, whereas FCC (including copper) materials do not. More recent observations using high–speed fatigue testing devices extend the experimentally exploitable regimes to cycle–numbers beyond 10^{10} [56]. This cycle regime is commonly referred to as Ultra–High–Cycle–Fatigue (UHCF), and has become the object of studies [11, 57], motivated by industrial demands e.g. springs in automotive or industrial suspensions [58]. Despite the increasing use of high–speed testing techniques are more and more applied [59, 60, 61, 62], a lack of available fatigue data to date has made it impossible conclusively to verify the extrapolated trend from former HCF fatigue data. However, it is believed that materials offer a wider variety of possible behaviours than originally suspected (see dashed lines in Fig. 2.6). For pure soft copper (99.88%, 750 °C for 75 minutes in vacuum), a “fatigue life threshold” was defined and measured by Stanzel-Tschegg et al. [63] in 2007. By taking replicas of sample surfaces of interrupted ultrasonic–swinger fatigue tests they defined the thresholds for the appearance of Persistent Slip Bands (PSB) (62.6 MPa) and Slip Bands (SB) (34 MPa). They stated that while cycling the samples with stress amplitudes as low as the SB-threshold, irreversible cyclic slip still occurs and, as a result, SB features can be observed. The plastic strain amplitude was calculated to be approximately 4 x 10^{-6}, corresponding to approximately 1 % of the total strain amplitude only. Nevertheless, they observed that, even under stress levels 50 % higher than the PSB-limit, no fracture occured after 10^{10} cycles. They therefore defined this point as the “fatigue life threshold”, eventhought the sample surface at these stress levels is almost completely covered with PSBs. It is generally recognized that PSBs are a pre–requirement for the formation of fatigue cracks in pure crystals [41]. Observations of threshold stress for PSB formation hence automatically imply the existence of a fatigue (stress or strain) limit, below which no failure occurs [64, 65].

2.3.5. Role of Surfaces for Crack Initiation

In 1958, Wood proposed a mechanism which explains how fatigue cracks in metals and alloys of high purity occur [66]. Repeated cyclic straining of the material produces different amounts of slip on the individual slip systems. The shear deformation along slip bands is irreversible and results in roughening of the surface: microscopic "hills and valleys" form in those places where the slip bands reach the free surface. These features are referred to as extrusions and intrusions, and represent micronotches, where stresses concentrate. Fatigue processes are aggravated in these regions, which are prone to be sites for fatigue crack nucleation.

A more recent model of Essman et al. from 1981 [67] pointed out another important aspect in the role of PSB in fatigue crack formation. The interface between a PSB and the matrix can be seen as a plane of discontinuity with very abrupt gradients in density and distributions of dislocations. Indeed, it was observed by Hunsch et al. in 1986 [68] that the strain within a PSB is highly non–homogeneous and very localized at the PSB–matrix interface.

Based on Wood's model and Essman's models, it is thought that fatigue crack initiation is strongly biased by the roughening of the surface. Experiments on polycrystalline copper performed by Thompson et al. in 1956 [69] showed that at a certain point of fatigue life removing surface roughness by electro polishing leads to a significant enhancement in total fatigue life. This was experimentally shown by Basinski et al. in 1983 [70] even for copper single crystals with PSBs traversing the whole bulk.

In both HCF and UHCF, it is known that the material may spend more than 90 % of its lifetime with crack initiation processes, which are therefore the limiting factor for fatigue life [41]. In contrast, in LCF, crack propagation plays the major role [41]. For this reason, in the HCF adn UHCF regimes, particular attention must be paid to the evolution of the surface at cycle numbers above 10^4 [63, 71].

2.4. Thermal Fatigue

The classical example for thermal fatigue was already observed in the early 1960s. During the starting and stopping processes of gas turbines, temperature gradients in the turbine blades, particularly between the blade surface and the bulk, cause thermal stresses [72, 73]. The more abrupt these starting and stopping processes are, the higher is the temperature gradient and hence the higher are the thermal stresses.

Generally, thermal stresses arise wherever different thermal expansions have to be accommodated. This can be the case of the mentioned turbine blades where surface and bulk material are similar and the temperature gradient causes differences in thermal strain. When temperature gradients become very large, the thermal stress can exceed the tensile strength of the material. In brittle materials, fracture can occur in a single thermal cycle. This is referred to as thermal shock. Materials which exhibit a good thermal shock resistance, generally have high thermal conductivity, high toughness, high yield strength, a low thermal expansion coefficient and low Young's modulus in the range of temperatures applied. These characteristics are also beneficial for withstanding repeated temperature cycles hence for thermal fatigue resistance.

However, thermal stresses can also arise where materials with different thermal expansion coefficients are joined together. At high temperatures, a resulting mismatch of thermal expansion has to be compensated at the joint and its surrounding area. Ceramic thermal barrier coatings, developed for increasing combustion temperatures in gas turbines, have to cope with this difficulty [74]. In general, they are very thin and have very high melting points. Unfortunately, the thermal expansion coefficient of the coatings are is generally very different from that of the bulk substrate material. A multi–layer approach was developed in order to ensure the adhesion of these ceramic coatings to the substrate over a very wide temperature range.

In general, it can be said that thermal fatigue represents a multi–axial load case. In very specialized tests, biaxial loading can be assumed; for example thermal cycling of thin films in [75] or in laser fatigue tests, as will be shown in Chap. 4.4.3. In most cases, due to the three dimensional–shape of samples and the presence of thermal gradients, triaxial stess/strain models have to be considered. For highly anisotropic materials, such as copper, the stresses have to be broken down into different, strongly orientation–dependent components in order to provide an analytical description of a thermal fatigue problem.

Fissolo et al. in 2009 published results of thermal fatigue experiments where tubes made of 316L steel and 304L steel in a furnace were cyclically quenched with water injections on the inner surface [76, 77]. With the help of numerical models they calculated the resulting cyclic equivalent strains and compared the resulting lifetimes to uniaxial mechanical fatigue data. They clearly showed that thermal fatigue is more damaging than uniaxial isothermal fatigue, and explained this by its multi–axial character.

3. Motivation and Objectives

The need for high accelerating gradients for CLIC imposes considerable constraints on the materials of the AS. The design accelerating fields (100 MV/m [5, 8]) will be the highest ever achieved in room temperature accelerating cavities. It is clear that this complex technology requires careful monitoring and verification by tests and experiments.

The object of the present study is to perform a systematic investigation of the thermo-mechanical surface fatigue phenomena occurring in copper and copper–based alloys under the severe operating conditions anticipated for the CLIC–AS. For the first time, the combination of the complex loading conditions and the very high cycle numbers is considered from a materials engineering point of view. The objective is to predict material fatigue behaviour and select the most suitable material for use in the CLIC–AS.

The surfaces of the AS exposed to high levels of RF–induced currents are subject to cyclic thermal stresses, which could induce surface breakup by fatigue within the 2.3 x 10^{10} cycles foreseen for 20 years of operation [5, 8]. Fatigue failure is therefore a significant risk to the operation of CLIC. Interpolating the available fatigue data for uniaxial fatigue testing to the foreseen cycle numbers and comparing this data to the complex loading conditions in the AS is far from trivial. In order to cope with this lack, this study considers four different fatigue techniques applied to pure copper, as described in detail in Chap. 4.4:

1) conventional fatigue using a mechanical universal testing machine (low repetition rate, uniniaxial loading)

2) ultrasound swinger fatigue device (very high repetition rate, uniaxial loading)

3) laser fatigue, where an area on a sample surface is repeatedly heated through irradiation (low repetition rate, thermal fatigue close to CLIC parameters)

4) RF–fatigue device, where alternating electromagnetic fields are used to repeatedly heat the surface (low repetition rate, thermal fatigue induced by the same mechanisms as in CLIC)

The main topics handled by the current work are:

(1) understanding the basic mechanism of fatigue observed when low loads induced by cyclic shallow–surface heating are applied to copper alloys

(2) relating those fatigue mechanisms to conventional fatigue induced by bulk cyclic loads

(3) determining if pulsed laser, RF-fatigue and bulk ultrasonic fatigue tests can provide a basis for extrapolations for the choice of a suitable material for he fabrication of the CLIC ASs

4. Experimental

This chapter gives details about the experiments conducted for the purposes of the present study. In the first part, the sample material in its different tempers is described and the necessary characterization methods are introduced. Since the surface state is of paramount importance the second part describes the surface analysis methods in detail. Copper thin films and their fabrication and characterisation methods are treated in the third part. The chapter close with a detailed description and analysis of the four fatigue techniques used.

4.1. Material and Characterisation

4.1.1. Heat Treatments of Oxygen–Free–Electric Copper

The baseline material used for the experiments is high conductivity–oxygen free–copper min 99.99 % (Cu–OFE REF. UNS C10100 Grade 1) complying with different international standards [78, 79, 80, 81] and CERN specifications [82]. Reception form is a cold drawn rod of diameter 40 mm. Table 4.1 summarises the properties measured for the tempers considered here.

Temper	$R_{p0.2}$ /MPa	R_m /MPa	Grain size /μm	Hardness /HV10	A /%
"half–hard" (H02)	315	325	110	110	18
"brazing annealed"	72	270	400	41	37
"dead soft annealed"	70	255	1400	35	28

Table 4.1.: Comparison of measured mechanical properties of copper tempers used for the experiments.

1) The "half-hard" temper (H02 according to ASTM B601 [1]) is obtained by

cold drawing and shows a yield strength of approx. $R_{p0.2} = 316$ MPa (compared with 200 - 240 MPa specified in [82]). Fig. 4.1 shows the micro structure of the H02 temper, with an average grain size of 110 μm (rougher than the 90 μm specified in [82]). This state represents the reference for the CLIC AS as machined from bulk material, prior to brazing.

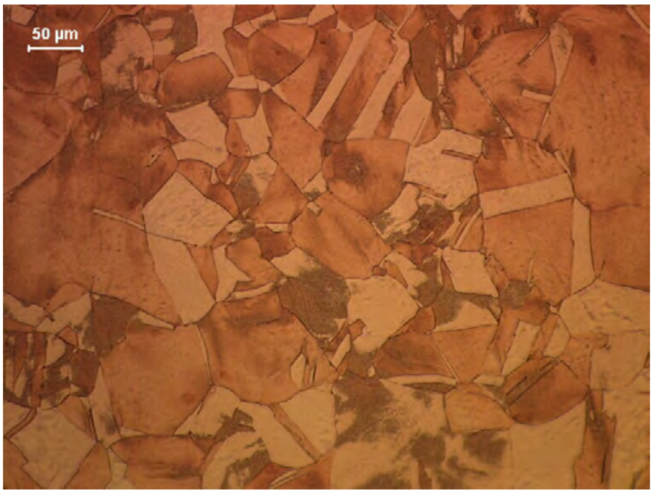

Figure 4.1.: Microstructure of cold drawn OFE copper in temper state H02

2) The "brazing annealed" temper reproduces the standard vacuum brazing cycle routinely used for copper joining at CERN. The treatment parameters for the brazing cycle are: heat to 795 °C at a rate of 300 K/h and hold at that temperature for 60 min, then heat to 825 °C at a rate of 100 K/h and hold for 6 min, followed by natural cooling in vacuum. The resulting microstructure is presented in Fig. 4.2. As expected the yield strength $R_{p0.2}$ decreased significantly after the treatment, from 316 MPa (H02 temper) to 72 MPa, while the average grain size increased from 110 μm (H02 temper) to 400 μm. The microstructure shows numerous annealing twins. This state represents the material state of a CLIC AS after a 825 °C brazing cycle.

3) The "dead soft annealed" temper is achieved by applying the following annealing cycle in vacuum: heat to 1000 °C at a rate of 300 K/h and hold for 2 h followed by natural cooling in vacuum. The resulting yield strength $R_{p0.2}$ of 70 MPa corresponds to a fully annealed product and is as low as for "brazing annealing" (72 MPa). This treatment resulted in the microstructure shown in Fig. 4.3. The average grain size increased significantly from 110 μm

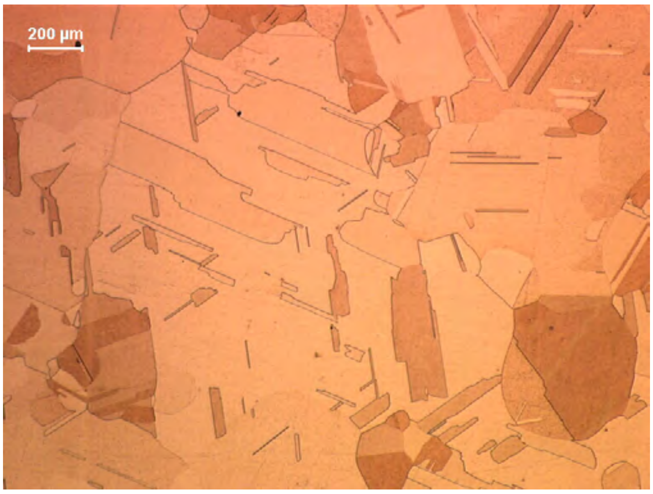

Figure 4.2.: Microstructure of "brazing annealed" OFE copper obtained by standard (825 °C) vacuum brazing cycle.

(H02 temper) to 1400 μm. It contains a significant amount of larger annealing twins as compared to Fig. 4.2. This temper state is used to quantify fatigue damage through roughness measurements on different crystallographic orientations. For this, grains of a minimum size of 1 mm are needed to perform surface characterisation following fatigue experiments.

4.1.2. Surface Finishing

As mentioned in Chap. 2.3, in HCF and UHCF, special attention is paid to the evolution of the surface state during fatigue lifetime. Features developing are of microscopical size. In Fig. 4.4a the SEM picture of Cretegny et al. [45] shows the size of surface features developing on polycrystalline copper submitted to a cyclic strain of $\Delta\epsilon_{tot}/2 = 2.5 \text{ x } 10^{-3}$. Fig. 4.4b shows the SEM picture of Stanzel et al. [63] of the smaller developed surface features when compared to Fig. 4.4a for a lower cyclic strain of $\Delta\epsilon_{tot}/2 = 4.8 \text{ x } 10^{-4}$. Since in the present study the applied strain loads in the fatigue test bench (see Chap. 4.4) are comparable to those of these two studies, the expected sizes of surface features developing during cycling are 0.2 μm - 1 μm in height and 0.5 μm - 10 μm in width. Therefore, the initial surface before fatigue testing needs to be extremely smooth. Two methods of surface finishing were used:

1) Diamond fly–cut is an advanced machining technique performed with ultra

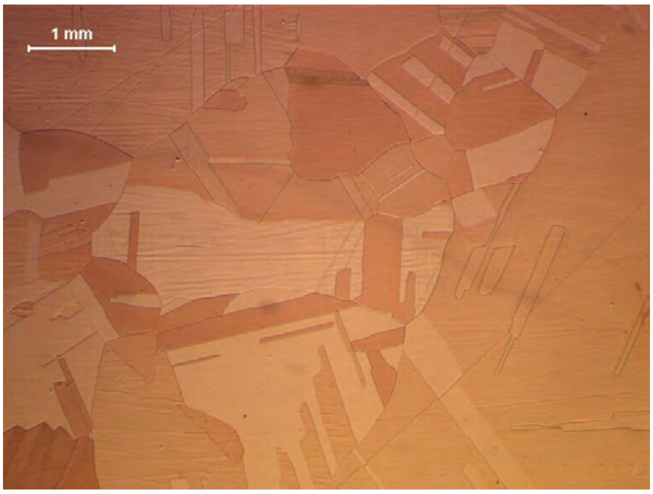

Figure 4.3.: Microstructure of “dead soft annealed” OFE copper obtained by annealing at 1000 °C for 2 h in vacuum.

precise machine tools equipped with single crystal diamond tools. It is suitable for flat surfaces only. Layers of decreasing thickness are removed, with only a few microns being removed in the the final cut. The resulting roughness value Ra of as–machined samples is between 1 nm and 4 nm and also satisfies the current specified roughness for the machining of the CLIC AS, at $Ra = 0.02$ μm.

2) Electro–polishing, applicable also to curved surfaces, induces no surface deformation at all. By removing a layer of 80 μm – 100 μm, it is ensured that the deformed surface layer created by machining is entirely removed and the new surface is completely undeformed. The resulting roughness values are comparable to those obtained with the diamond fly–cut finishing method.

4.1.3. Cleaning Procedure for Vacuum Heat Treatments

All parts which undergo a treatment in a vacuum furnace were thoroughly cleaned. For copper parts, this cleaning procedure consisted of two steps:

1) chemical degreasing with the alkaline detergent NGL 17.40 Alu (10 g/l) from NGL Cleaning Technologies (Switzerland) at 50 - 60 °C for 30 - 60 minutes in an ultrasonic bath followed by water rinsing and

2) pickling with 50 % hydrochloric acid at 20 °C for 10 -30 seconds followed by water rinsing.

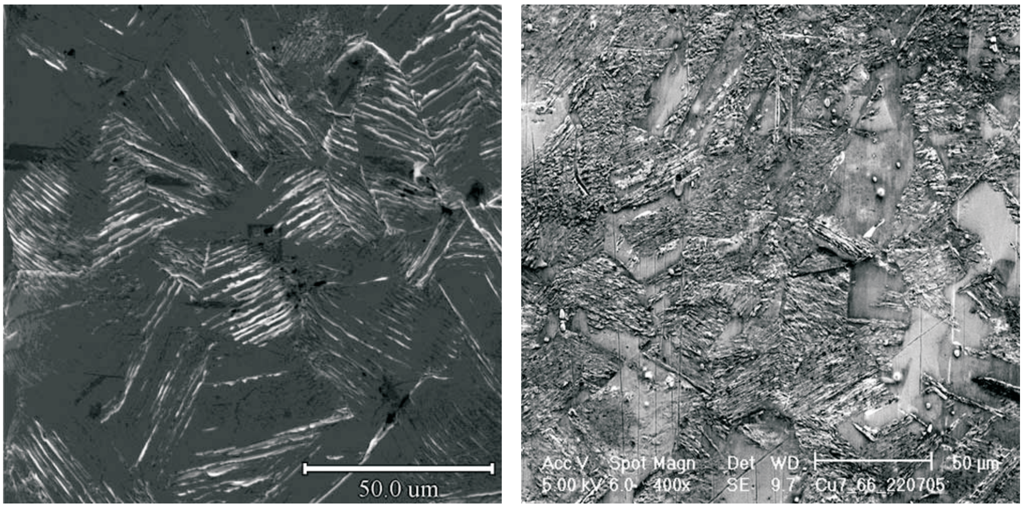
50.0 um
Acc.V Spot Magn Det WD 50 µm
5.00 kV 6.0 400x SE 9.7 Cu7_66_220705

a) b)

Figure 4.4.: a) from [45] fatigued polycrystalline copper for 6900 cycles at $\Delta\epsilon_{tot}/2 = 2.5 \text{ x } 10^{-3}$. Individual feature size in the order of 1 μm in height and 10 μm width. b) from [63] fatigued polycrystalline copper for 1.3 x 10^{10} cycles at $\Delta\epsilon_{tot}/2 = 4.8 \text{ x } 10^{-4}$. Individual feature size in the order of 0.2 μm in height and 0.5 μm width.

4.1.4. Tensile and Compression Testing

For the tensile and compression tests, a UTS 200 universal testing machine from UTS Testsysteme GmbH was used. Tests were conducted in accordance with ASTM E8 / E8M–09 [83] and ASTM E9–09 [84], respectively. Samples were machined by turning from the rods so that the drawing axis is parallel to the sample axis. The geometry and dimensions are shown in Fig. 4.5.

4.1.5. Macrohardness

For the macrohardness test, a Dia Testor 2Rc from Otto Wolpert–Werke with a Vickers diamond pyramid was used. Tests were conducted in accordance with to ISO 409–1 and ISO 409–2 [85, 86]. All values given are averages of five valid measurements in either HV10 (e.g. annealed copper) or HV30 (e.g. copper in H02 temper).

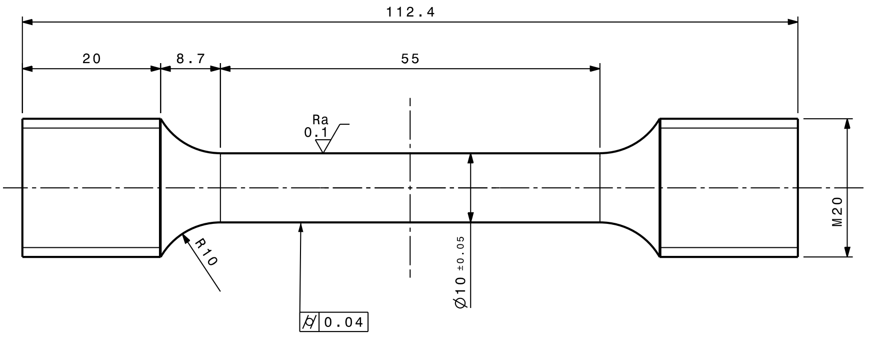

Figure 4.5.: Sample geometry and dimensions of standard tensile test sample complying [83, 84]

4.1.6. Electrical Conductivity

For characterizing the materials in terms of electrical conductivity, a Sigmatest 2.069 from Foerster was used. This portable device is an eddy–current based instrument suitable for non-ferromagnetic metals. It measures the electrical conductivity based on the complex impedance of its measuring probe. The values are generally given in % IACS (International Annealed Copper Standard). The testing frequency can be varied between 60 kHz and 960 kHz. The higher the frequency is, the smaller becomes the penetration depth of the eddy currents in the material due to the skin effect. All electrical conductivity measurements are performed at the lowest testing frequency of 60 kHz, in order to average the measurement over a great depth. The *effective penetration depth* d_{eff} (in mm) is calculated from this *frequency* f (in Hz) and the *electrical conductivity* κ (in MS/m) of copper using the empirical formula from [87]

$$d_{eff} = \frac{503}{\sqrt{\kappa \cdot f}} \tag{4.1}$$

The value obtained is 270 μm, which essentially rules out effects such as influences on the measurement from surface oxide layer.

4.2. Surface Analysis

4.2.1. Metallography and Optical Microscopy

For the light microscopy observations, a Leica DMRME reflected-light microscope was used. The sample preparation for optical observations consisted of conventional grinding (SiC paper) followed by polishing with diamond emulsion, ending, for optical microscopy observations, with a 1 μm diamond diameter emulsion. To reveal grain structure, macro etching with ammonium peroxodisulfate was performed, in accordance with ASTM standard E407–07 [88]. For determining the average grain size, measurements in accordance with ASTM standard E112–96(2004) [89], using the Lineal Intercept Procedure, were performed.

4.2.2. Roughness Analysis

Roughness measurements were performed with the help of a 3D VeecoNT3300 in Vertical Scanning Interferometry (VSI) mode, as described in detail in [90]. For the characterization of the surface roughening during cycling, several roughness parameters were used. In order to keep the results comparable to those of previous studies [91], the standard parameter Ra [92] was chosen for the roughness threshold in the laser fatigue test bench (described in Chap. 4.4.3). Ra is an average over integrated roughness values and therefore is not very sensitive to isolated features. As a parameter more sensitive to single local features, the standard parameter Rz [92] was also used. It represents an average of peak–to–valley values, taking extreme local effects into account better. Ra and Rz are direction–dependent parameters defined originally for regular machining traces. Since the surface profile depends on the orientation of the measuring plane with respect to machining traces or fatigue features, very different roughness results are obtained [92]. An additional, direction independent parameter, Surface Index (SI), is introduced [90]. The SI value is defined as the ratio between true surface and projected surface. Its value is 1 on an ideally smooth surface. the parameter $SI - 1$ is used here for reasons of easier illustration (for a perfectly smooth surface, $SI - 1 = 0$).

4.2.3. Orientation Imaging in Scanning Electron Microscopy

Specimens were examined ex–situ with a Scanning–Electron–Microscope (SEM) using Electron–Back–Scattered–Diffraction (EBSD) to observe surface features resulting from fatigue. Two different microscopes were used:

1) For the determination of the grain orientations on the bulk samples, a Leo 1530 VP SEM with an EBSD unit from EDAX TSL was used, equipped with TSL OIM Data Collection© software.

2) For thin film characterization, a Sigma SEM from Zeiss equipped with a Oxford Instruments HKL Technology EBSD unit was used. Since expected minimum grain sizes were below 10 μm, a step size of 0.1 μm was used for the observations. Acquisition and analysis of EBSD data was performed using Channel 5©.

For a detailed description of the EBSD technique, see [93, 94, 95]. Essentially, the back–scattered electrons create a Kikuchi pattern on a phosphoric screen, which is recorded by means of a digital camera. For the analysis, a computational algorithm is used. With the help of the so called Hough Transformation, the Kikuchi lines can be transformed into points of high intensity in Hough Space. These maxima of intensity are easier to detect by mathematical algorithms. After a back transformation, the recreated Kikuchi pattern can be illustrated. With the help of several material parameters, automatic indexing can be performed. In this way areas can be scanned, giving orientation maps of crystalline surfaces. This data can be analysed for grain size measurements, texture analysis, misorientation measurements between adjacent grains, etc. The orientation data identified by EBSD is expressed using either the common [h k l] notation or the more complete Euler Angles notation (see [96]). The Euler notation represents a sequence of three rotations of the elementary cell described by the Euler angles. The common "zXZ" convention used in this study signifies the sequence for the rotation axis: *original* z-axis → *new* x-axis → *new* z-axis. Tab. 4.2 shows the correspondence of the two notations for the main crystallographic orientations.

For texture analysis with EBSD the Multiples of Uniform Distribution factor (MUD–factor) is used. The principle of the MUD factor is the same as that of the T_{hkl} used for the XRD technique. It is a measure of the frequency of occurrence

hkl notation	Euler notation		
	Eu1	Eu2	Eu3
1 0 0	x	0 °	x
1 1 0	x	45 °	0 °
1 1 1	x	54.7 °	45 °

Table 4.2.: Correspondence between hkl notation and Euler notation for main orientations. “x” means arbitrary value possible.

of an orientation, but, unlike T_{hkl}, takes into account all grain orientations. Since T_{hkl} is limited to orientations possessing a Bragg angle in the measuring range, a high fraction of grain orientations is therefore neglected in T_{hkl}. This is not the case for the MUD–factor. Like T_{hkl}, the MUD–factor equals 1 for a homogeneous orientation distribution. Values smaller than 1 indicate a lower frequency of occurrence, values greater than 1 indicate a higher frequency of occurrence [97].

In the present study, EBSD scans performed in fatigued areas made it possible to assign grain orientations to regions with fatigue–induced surface features and to assess their shape, size and orientation with respect to the grain lattice. EBSD maps were produced with step sizes of 10 μm on the dead soft annealed samples (average grain size 1400 μm) and 2 μm on the as–received samples (average grain size 110 μm). Analysis of EBSD data was conducted using TSL OIM Data Analysis©. Only values for grain orientations with a confidence index higher than 0.1 (i.e. 95 % probability) were considered.

4.2.4. Local Hardness

Classically, fatigue alters the mechanical properties of a material. Hardness was measured in order to characterize the influence of the applied thermal/mechanical cycling on the mechanical properties. The local hardness observations were performed in two different regimes. The nano–indentation measurement, performed with the help of a MTS NanoIndenter XP, detects extremely small indentation depths, hence indentation diameters, which results in high lateral accuracy and resolution. It was therefore possible to monitor surface hardness at different stages of fatigue on thermally cycled samples of the LA-fatigue test bench. Tests were performed with a 200 mN load on the fatigued and hence rough surface. No supplementary preparation was applied before hardness testing. This technique also made it possible to record the distribution of hardness in depth on a cross section of a fatigued surface. The cross section was cut from the sample with a water cooled abrasive cutting machine. It was then embedded in an epoxy resin, followed by a metallographical polishing down to 1 μm diamond suspension.

The micro hardness observations were performed with the help of a micro hardness tester MHT-4 from PAAR, mounted to an optical microscope Aristomet from Leitz. Measurements were conducted in accordance with ASTM standard E384 [98]. This method was used to determine the hardness distribution on RF fatigued samples, for example.

4.3. Copper Coatings

Coatings or thin films sometimes exhibit unusual properties compared to their bulk counterparts: for example, superior mechanical strength. Pure copper coatings are considered in this study for three reasons:

(1) The results of observations on the dependence of the surface degradation during thermal cycling on grain orientation of pure copper made it desirable to test highly textured copper. Depending on the coating method and parameters, it is possible to produce a strong textured coating. The available techniques in house allow the fabrication of highly textured pure copper films as an alternative to strongly textured bulk material.

(2) Theoretical and experimental results from other researchers provide contradictory findings as to whether the fatigue life can be enhanced through submicrometric grain structures or not [99, 100, 101, 102]. Depending on process parameters, thin films with very fine grain sizes and even nanocrystalline and amorphous structures can be produced.

(3) Among all the materials that are potential candidates for use in the ASs, attention has to be paid to materials and techniques which may be applicable in the production process of CLIC–AS. Coating relevant surfaces of the AS with a thin film is considered as a possible procedure for enhancing properties,

particularly as regards resistance to electrical breakdown and pulsed surface heating.

4.3.1. Fabrication

For the production of the copper thin films, the principle of plasma enhanced Physical Vapor Deposition (PVD) is used. The process is explained in detail elsewhere [103, 104]; only a short introduction will be given here. As PVD is a line of sight process, careful arrangement of the samples with respect to the target has to be assured [103]. We used a custom made CERN device with a GENCOA [105] magnetron sputtering unit. Discs from round bars of diameter 40 mm in OFE copper in H02 temper were used as substrates. In order to observe the influence of the substrate morphology on the resulting film properties, stainless steel 304L discs were selected as additional substrates. Before coating the samples were metallographically polished and underwent the standard cleaning procedure as described in Chap. 4.1.3. Since PVD coatings tend to grow epitaxially the continuity of a copper coating on copper has to be broken. For this purpose a 250 nm titanium film was deposited before the copper coating. In order to guarantee the same initial coating conditions for both substrates, the stainless steel samples were also precoated with a titanium film of the same thickness. Every coating process thus involved a twin pair of samples of both substrates, coated at the same time and with the same process parameters. Fig. 4.6 shows a sketch of the setup used for coating.

The chamber was evacuated to 10^{-8} mbar and then filled with argon gas to working pressure (approx. 10^{-3} mbar). Since the copper target is connected to a negative voltage of 380 V, argon ions are attracted and hit the surface. The sputter current was 400 mA in all coating processes. During the argon ion bombardment numerous processes occur in parallel, as summarised in [103, 104]. Two important processes should be mentioned here:

1) Extraction (sputtering) of a surface atom when the energy transmitted from the argon ion to the surface atom is high enough (called *sputtering threshold* [103, 106]).

2) Emission of secondary electrons from the surface.

The emitted electrons are trapped close to the target surface by the magnetic

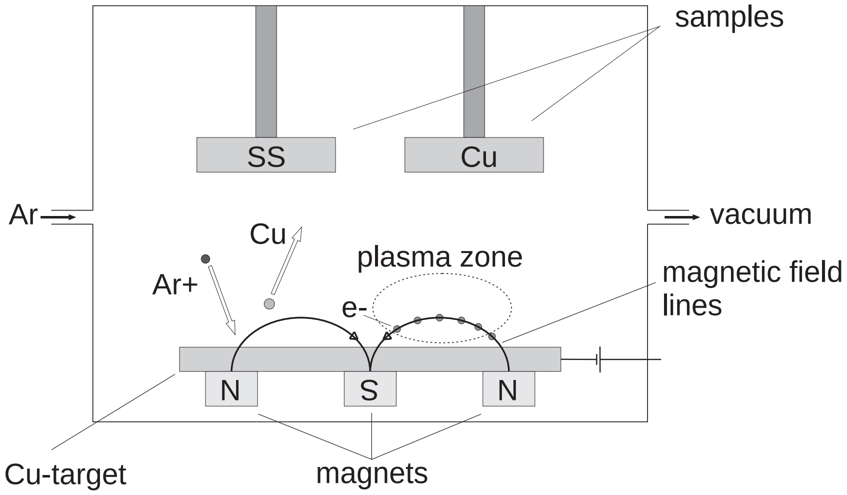

Figure 4.6.: Plasma enhanced PVD setup applied.

field and therefore increase the ionization rate of the neutral argon atoms, which directly increases the sputtering rate [107]. A plasma builds up near the target surface, with the characteristic glow caused by argon ions falling back on lower energy levels and emitting photons. Since the sputtered copper atoms are mainly neutral they are not influenced by the magnetic field. The energy needed for the sputtered copper atoms to be ionized is significantly higher than for the argon atoms. The sputtered copper atoms are deposited atom by atom on the sample surface and on the inner surface of the vacuum chamber. When the atom reaches the surface of deposition, it does not necessarily adhere the point of impact [108]. The possibility of the atom to migrate to a place of lower potential energy is governed by the development of interatomic attractive forces, kinetic energy, surface defects and substrate temperature (thermal mobility) [109]. For example, when the atom is deposited on a substrate at low temperature, the migration distance is shorter because of the lower thermal mobility [109]. A similar effect can be observed when high deposition rates are used and atoms do not have enough time to migrate before being covered by other atoms [109].

Table 4.3 summarizes the process parameters for the different samples.

Sample pair	Film thickness /μm	Argon pressure /10^{-4} mbar	Sputtering time /min	Ti film thickness /nm	Sputter power /W
Cu2+SS2	9	11	135	250	150
Cu3+SS3	20	11	310	250	150
Cu4+SS4	9	50	135	250	150
Cu5+SS5	9	11	100	250	200
Cu6+SS6	9	5.2	145	250	200

Table 4.3.: Process parameters for plasma sputtering of copper thin films on twin sample pairs (copper substrate "Cux" and stainless steel substrate "SSx", coated at the same time). Film thicknesses are derived from process parameters.

4.3.2. X-Ray Diffraction

For the X–Ray Diffraction (XRD) observations, a Cristalloflex D5000 from Siemens was used in the Bragg-Brentano configuration, sketched in Fig. 4.7. The X–Ray tube and the detector aperture are on the common measuring circle, withthe X–Ray tube mounted on the device. As the sample is tilted around θ, a precise movement of the detector lever ensures the corresponding 2θ position. In oder to narrow the divergence of the X–Ray beam, the aperture slits can be closed. The Soller slits consist of a stack of radiation–absorbing metal sheets that reduce axial divergence of the secondary X-Ray beam. Before entering in the detector, the secondary X-Ray beam passes a monochromator to ensure the detector only counts signals diffracted from the sample, excluding noise of other wave lengths. The diffraction intensity as a function of 2θ can be illustrated as shown in Fig. 4.8, where diffraction data from pure copper powder is shown. The intensity maxima at the so called "Bragg angles" indicate that Bragg's conditions are met. According to Bragg's law

$$n\lambda = 2a\sin\theta \tag{4.2}$$

each *Bragg angle* θ corresponds to a certain distance between the lattice planes (*lattice parameter* a) linked through the *wavelength* λ of the X-Rays. When Bragg conditions are met, constructive interference occurs and a strong signal is

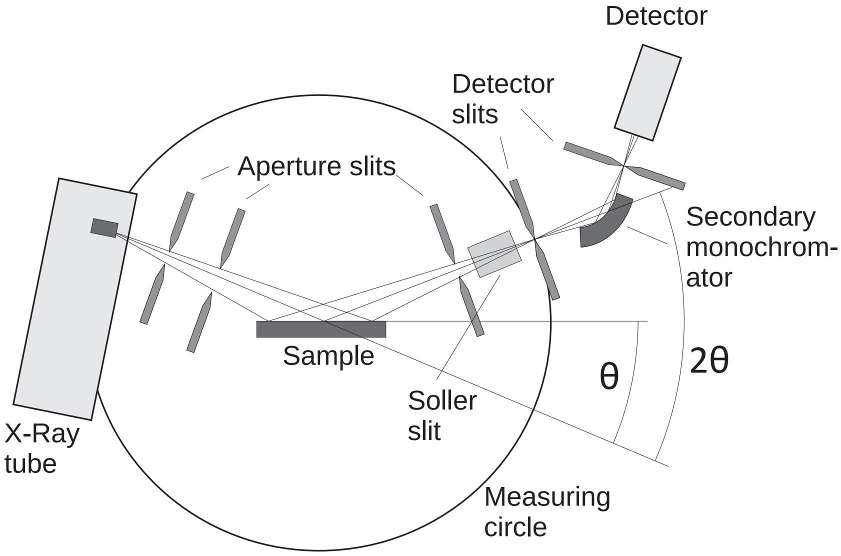

Figure 4.7.: X-Ray diffractometer in Bragg-Brentano configuration

diffracted. Through the measurement of the *lattice parameter a* and a catalog of Powder Diffraction Files (PDF) [110], it is possible to identify different chemical and crystallographical phases.

In the present study, the X–Ray diffraction technique is used for describing preferred orientations in the copper thin films. For bulk material, this was done first by Harris in 1951 [111], using rolled uranium bars. Here, a slightly modified form was use in order to characterise the degree of preferred orientation of a thin film [112]. This method was successfully applied by Peck [113] for PVD deposited niobium thin films: the *texture index* T_{hkl} for a given reflection is defined by the ratio [112]

$$T_{hkl} = \frac{I_{hkl}/I'_{hkl}}{\frac{1}{n}\sum I_{hkl}/I'_{hkl}} \tag{4.3}$$

where *I'* is the *integrated intensities* of *randomly* oriented samples (ideal powder) and I is the *integrated intensities* of samples with *preferential* orientations. The calculation is done for n reflections. Higher order reflections need not be considered, if the first order reflection is counted. The value for T_{hkl} is therefore a measure of the frequency of occurrence of a certain crystallographic orientation with respect to a random distribution [112]. Where all values of T_{hkl} equal 1, the distribution of orientations is uniform (powder spectrum). Values of T_{hkl}

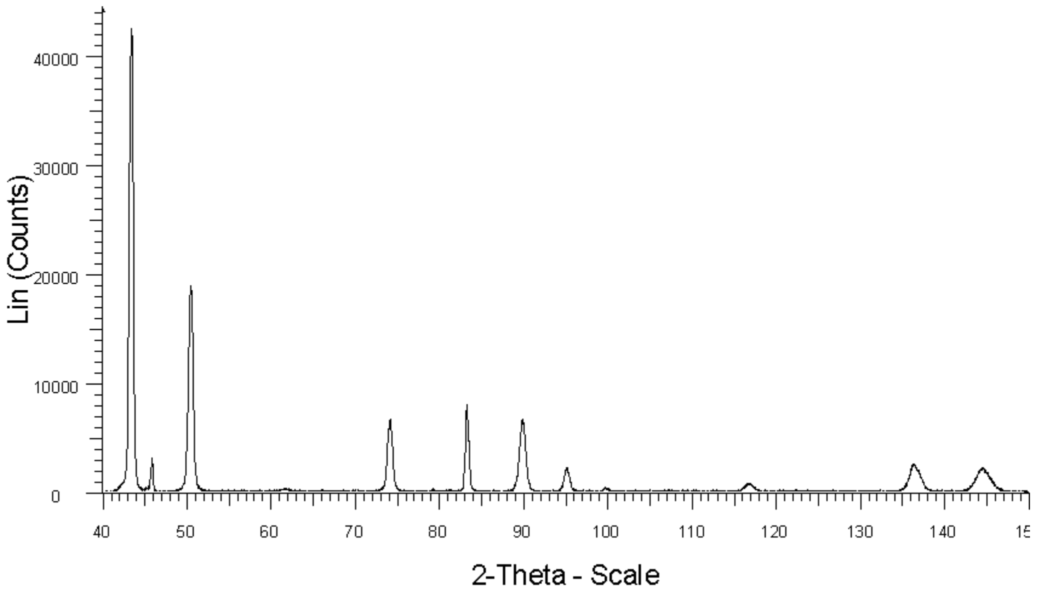

Figure 4.8.: Example of data of diffraction pattern from copper powder.

greater than 1 indicate that the crystals with the corresponding orientation occur more often; values smaller than 1, that the corresponding orientation occur more seldom. If the texture index of a grain orientation is 0, crystals with this orientation are not present in the diffracting volume.

For this study, all measurements were performed with the same copper tube ($\lambda = 0.154$ nm) and a constant accelerating potential of 40 kV. The penetration depth τ of the incident beam is depending on the diffraction angle θ, the X–Ray tube target material and the acceleration potential of the electrons hitting the target [114]. Its dependence on the diffraction angle is shown in Fig. 4.9. For the θ–2θ configuration, the higher the incident beam angle θ (i.e. the closer to 90°) is, the deeper the beam penetrates into the material. The values are calculated for the Kα_1 of a copper tube. The experimentally measured intensities from samples with 9 μm and 20 μm films are therefore contributed by diffracted signals coming from the film and from the substrate. In order to evaluate the fraction delivered by the film, the fraction of signal arising from the first 9 μm and 20 μm respectively was calculated for each Bragg angle. Fig. 4.10 shows the result of the calculations. It can be seen that even the reflection at the lowest Bragg angle [1 1 1] is not diffracted entirely within the 9 μm thick film, whereas this is the case in the 20 μm thick film. Starting from the second Bragg angle,

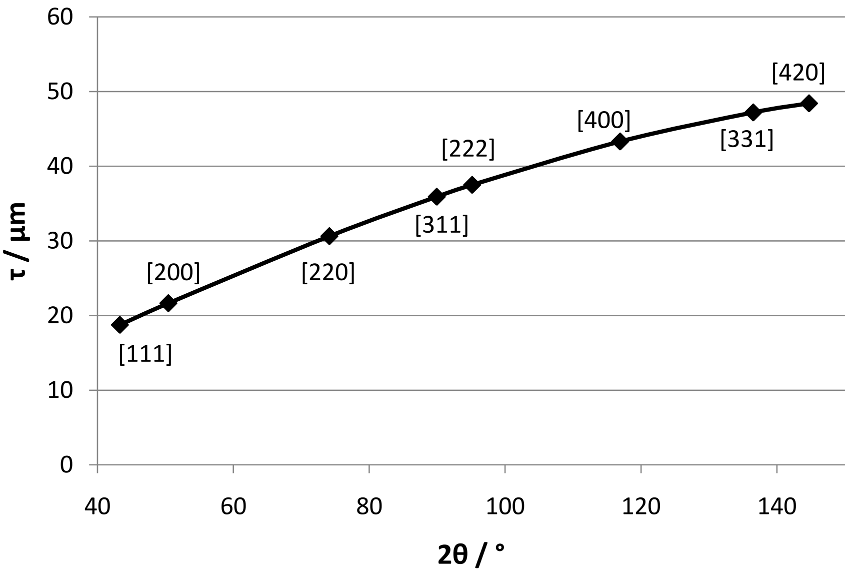

Figure 4.9.: Calculated penetration depth τ of CuKα radiation in copper as a function of diffraction angle. τ is defined as the thickness of the material that contributes to 99% of the diffracted intensity.

the substrate in both cases partially contributes to the measured intensities. On this basis it can be concluded that:

1) for the copper substrate samples, the substrate will contribute with its own texture to the measured intensities, affecting the estimation of the distribution of the integrated intensities of the films.

2) for increasing Bragg angles, hence higher penetration depths, the contributions of the substrates increase hence the contributions of the films decrease. The measured intensities of the powder do not need to be cleaned from the substrate contributions. The cleaning of the measured intensities of the coating decrease the integrated intensities of the film contributions which affects the comparison to the powder data and the calculation of T$_{hkl}$.

The contribution of the substrate texture of the copper substrate samples needs to be quantified. For this purpose a simple subtraction of intensities is conducted. For each Bragg angle (and hence penetration depth), the *corrected integrated intensity* $I_{hkl_{FCcorr}}$ contributed by the film is calculated as

$$I_{hkl_{FCcorr}} = I_{hkl} - I_{hkl_{bulk}}(1 - f_{hkl_{film}}) \tag{4.4}$$

where $I_{hkl_{bulk}}$ is the *integrated intensity measured in the bulk* and $f_{hkl_{film}}$ is the

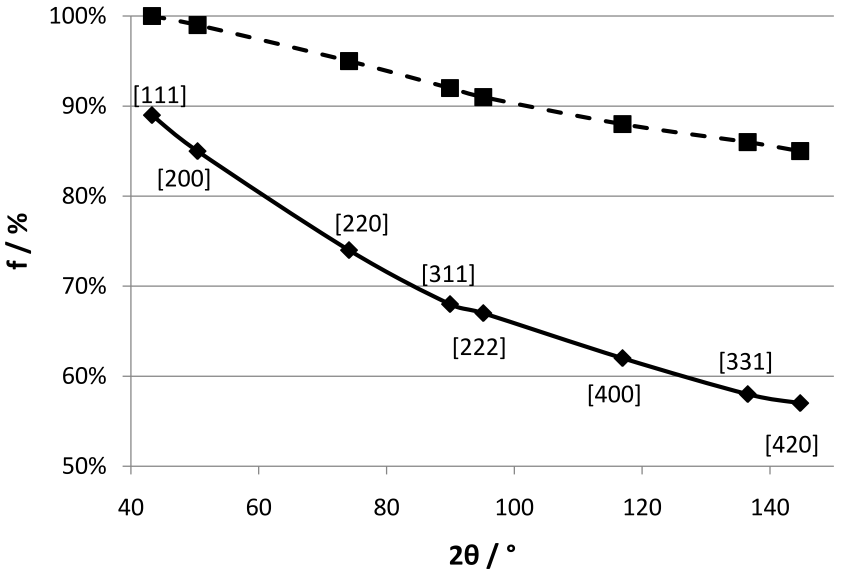

Figure 4.10.: Fraction f of diffracted signal coming from film of 9 μm thickness (solid line) and of 20 μm thickness (dashed line)

fraction diffracted by the film (see Fig. 4.10). Therefore, only intensities contributed by the film are taken into account for the texture index.

For the compensation of the second effect, another intensity correction is used here. Similarly to the substrate texture correction, for each Bragg angle (and hence penetration depth), the *corrected integrated intensity* $I_{hkl_{MIcorr}}$ is calculated by dividing I_{hkl} by the corresponding $f_{hkl_{film}}$

$$I_{hkl_{MIcorr}} = \frac{I_{hkl}}{f_{hkl_{film}}} \tag{4.5}$$

$I_{hkl_{MIcorr}}$ is therefore corrected for by the “missing” amount of insufficient film thickness.

In addition to the $K\alpha_1$ peaks, $K\alpha_2$ peaks are also present in the spectrum, separated by

$$\Delta 2\theta = 2 \tan\theta \left(\frac{\Delta\lambda}{\lambda}\right) \tag{4.6}$$

with respect to $K\alpha_1$ peaks, where $\Delta\lambda$ is 3.83 x 10^{-13} m [115]. A simple correction of the intensities was performed using Rachinger’s 1948 method [115]. The method is based on the assumption that the $K\alpha_1$ and $K\alpha_2$ profiles are identical in shape, but the intensity of $K\alpha_2$ is half of that of $K\alpha_1$.

4.4. Fatigue Test Benches

For the CLIC study, four fatigue test benches are currently available: the Conventional Fatigue test bench (CVF), the Ultrasonic Swinger test bench (USS), the Laser Fatigue test bench (LAF) and the Radio Frequency Fatigue test bench (RFF). The first three test benches are situated at CERN in Geneva. The fourth test bench was developed by the Stanford Linear Accelerator Center (SLAC), and is operated at Stanford, USA. A significant contribution of sample material for the test benches is provided by the High Energy Research Organization Japan (KEK).

4.4.1. Conventional Fatigue (CVF)

With the help of a UTS 200 mechanical universal testing machine from UTS Testsysteme GmbH, already used for the tensile and compression tests, fatigue tests were performed in accordance with standard ISO 1099 [116]. Tests were stress controlled, with a load ratio of R = -1. The sample geometry is shown in Fig. 4.11. Since the machine stroke is driven mechanically by ball bearing spindles, speed and accelerations are quite limited, allowing a maximum cycling repetition rate of 0.5 Hz. Achievable cycle numbers were limited by the long testing time and machine availability. Tests with maximum cycle numbers of about 1 x 10^6 were performed and were automatically stopped at rupture.

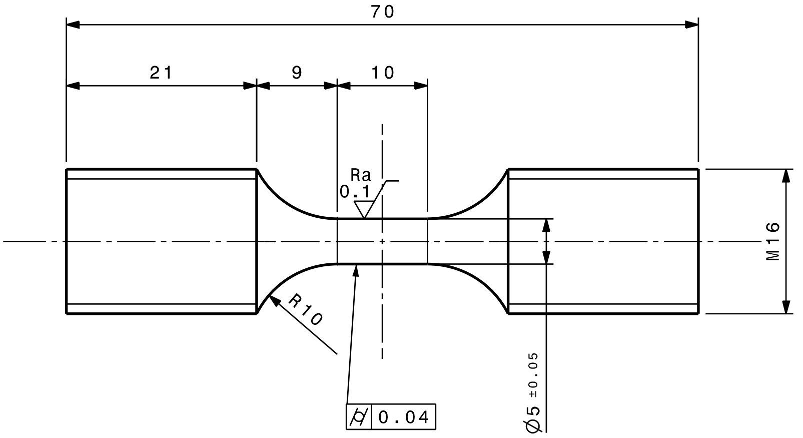

Figure 4.11.: Geometry of sample for conventional fatigue testing

Conventional fatigue testing is well understood and has the advantage of standardised, well controlled testing parameters [116].

4.4.2. Ultrasonic Swinger (USS)

In the USS test bench, an hour glass shaped sample was mounted on one end to a piezo–electric resonator. The experimental setup is described in detail elsewhere [117]. Fig. 4.12 represents a USS sample developed to feature first axial resonant frequency at 24 kHz which is the working frequency of the resonator. The sample design and optimisation to the correct resonant frequency were performed with the help of numerical simulations based on ANSYS Workbench©. During testing, the sample underwent cyclic uniaxial tension and compression loads with a load ratio of R = -1. The test bench is displacement controlled with an infrared sensor. The resonator can be operated at various amplitudes.

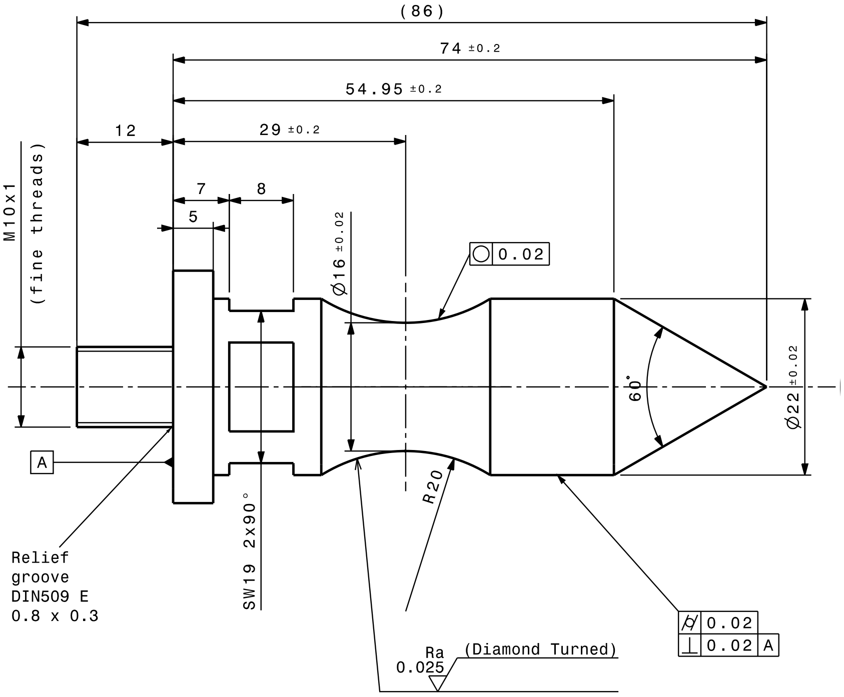
(86)
74 ±0.2
54.95 ±0.2
12
29 ±0.2
7
8
5
M10x1
(fine threads)
Ø16 ±0.02
○ 0.02
60°
Ø22 ±0.02
A
Relief groove DIN509 E 0.8 x 0.3
SW19 2x90°
R20
Ra 0.025
(Diamond Turned)
0.02
⊥ 0.02 A

Figure 4.12.: Hourglass–shaped USS test sample bolted to the resonator. Sample is designed to feature first resonant frequency at 24 kHz. Sample head in cone shape reduces cavitation pitting from cooling water

A LabView program was developed in order to record amplitude data over time and to maintain the amplitude at a pre-defined level. With the sample design shown, stress amplitudes in the range of 50 MPa - 90 MPa, corresponding to hence strain amplitudes between 4 x 10^{-4} and 8.5 x 10^{-4}, were obtained.

Fig. 4.13 shows a Finite Element Method (FEM) modal analysis simulation of the equivalent strain and stress distribution in a USS sample vibrating at the first resonant frequency. The time step was chosen to be in the maximum compressive amplitude. Stresses were relatively superficial whereas the region of highest strain extends deep in material [118].

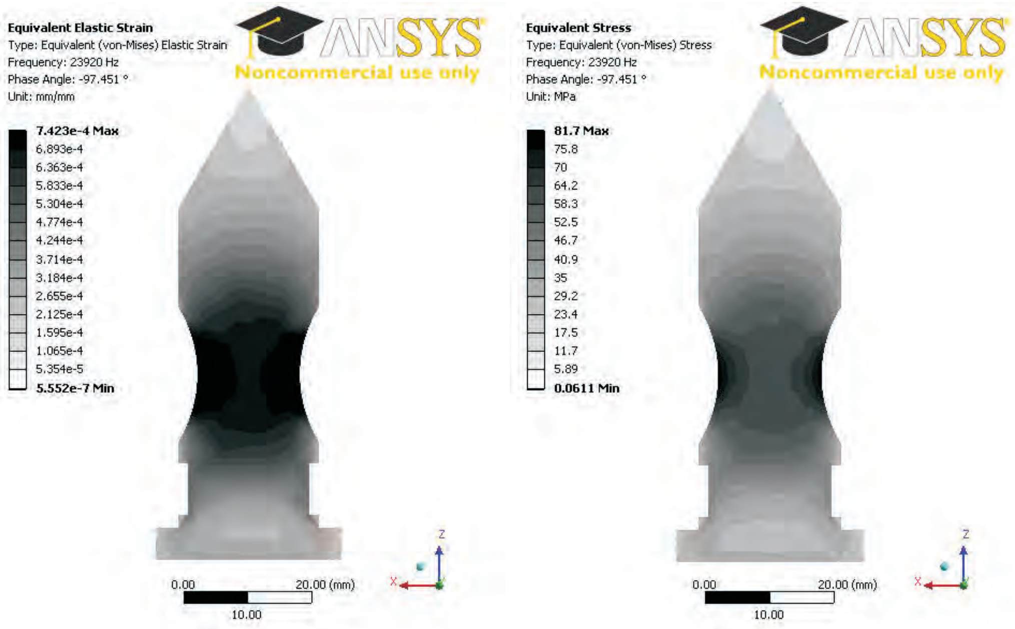

a) b)

Figure 4.13.: Equivalent (von-Mises) a) strain and b) stress distribution in a cross section of an USS sample. Stresses are very concentrated in the surface regions whereas the high strain region covers almost all the cross section.

Fig. 4.14 shows the stress component analysis for the USS sample for the same conditions as in Fig. 4.13. The longitudinal component (here z-axis) was significantly larger (by a factor of 10) than the circumference component (here y-axis). For the experiments performed in this study, the surface stress state was therefore assumed to be uniaxial.

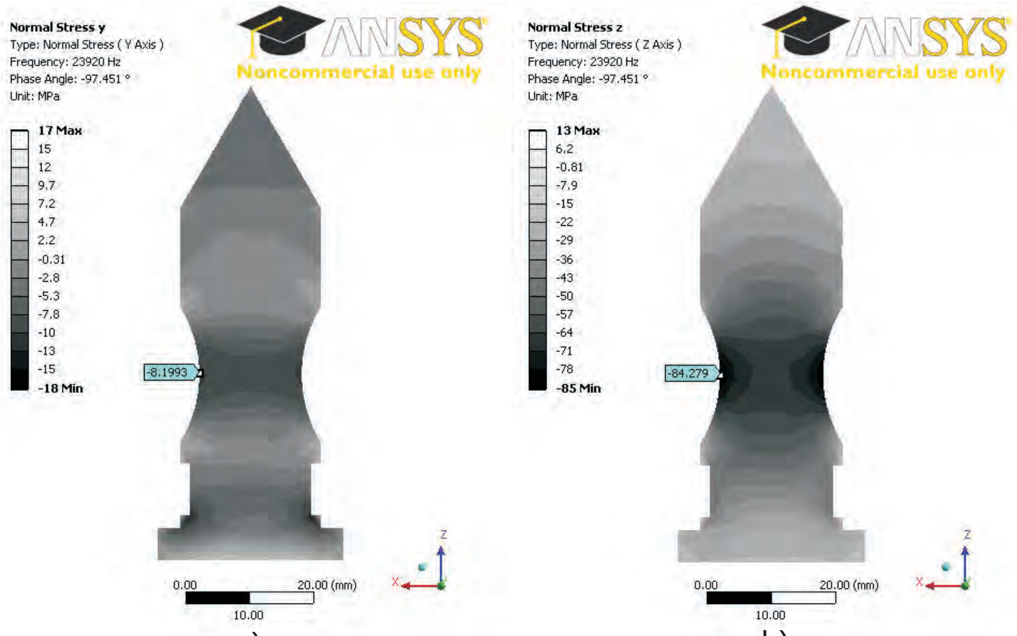
Normal Stress y
Type: Normal Stress (Y Axis)
Frequency: 23920 Hz
Phase Angle: -97.451 °
Unit: MPa
17 Max
15
12
9.7
7.2
4.7
2.2
-0.31
-2.8
-5.3
-7.8
-10
-13
-15
-18 Min
-8.1993
0.00
20.00 (mm)
10.00
Normal Stress z
Type: Normal Stress (Z Axis)
Frequency: 23920 Hz
Phase Angle: -97.451 °
Unit: MPa
13 Max
6.2
-0.81
-7.9
-15
-22
-29
-36
-43
-50
-57
-64
-71
-78
-85 Min
-84.279
0.00
20.00 (mm)
10.00
Z
X

a) b)

Figure 4.14.: Distribution of normal stresses in a) circumference and b) longitudinal direction. Longitudinal component in gage length very large (84 MPa compressive) compared to circumference component (8 MPa compressive)

In order to ensure the absence of flaws of the surface in the highest stressed regions, a final electropolishing of the gauge length was applied. To dissipate the heat induced in the sample during high frequency cycling, the sample head was immersed in a circulating water bath. On the resonator site, the mechanism was cooled through forced air convection, provided by a high power fan. The resulting steady state sample temperature as verified by infrared camera observations was below 50 °C. To minimise cavitation pitting, the sample head was cone shaped with an angle of 60°. The test end was characterised by the initiation of a crack inducing a change of the resonance frequency to a value out of the range of the resonator controlling system (23.5 kHz - 24.5 kHz).

Thanks to the high repetition rate of the test bench, the total cycle number of 2.3 x 10^{10}, corresponding to the estimated 20 years of CLIC lifetime, was achieved within 11 days of non-stop testing time.

4.4.3. Laser Fatigue (LAF)

The laser fatigue test bench used a pulsed ultraviolet excimer–laser ($\lambda = 248$ nm) to repeatedly irradiate a disc–shaped specimen under vacuum. The experimental setup is described in detail in [91]. The irradiated sample spot was a rectangle of 1 mm x 0.6 mm. Fig. 4.15 shows a fatigued laser sample where the dark spots correspond to the irradiated areas. Within each spot, uniform energy distribution was obtained through an energy homogenizer. Energy was therefore homogeneously distributed over the whole irradiated area within +/- 8 %. The absorption of ultraviolet light is known to be a thermal process in metals (excitation of electrons and phonons) and therefore independent of the crystallographic orientation of the grains [119]. Constant pulse energy was guaranteed through regular offline measurements provided by an energy monitor. A repetition frequency of 200 Hz, a pulse length of 40 ns and an energy density of 0.3 J/cm^2 (calculated to induce a temperature rise of ΔT = 180 K [91]) ensured that in between cycles, the irradiated area cooled down to room temperature. The estimated heated layer thickness was approximately 10 μm. In this way, there was no steady temperature rise in the specimen. Lateral thermal expansion due to heating from irradiation was constrained by the surrounding material. The thermally–induced cyclic equivalent compressive strain load ϵ_{equiv} is estimated at between 0 (no irradiation) and 5.1 x 10^{-3} (maximum of ΔT). Fig. 4.16 shows a simple ABAQUS© simulation example for a laser pulse irradiating a copper

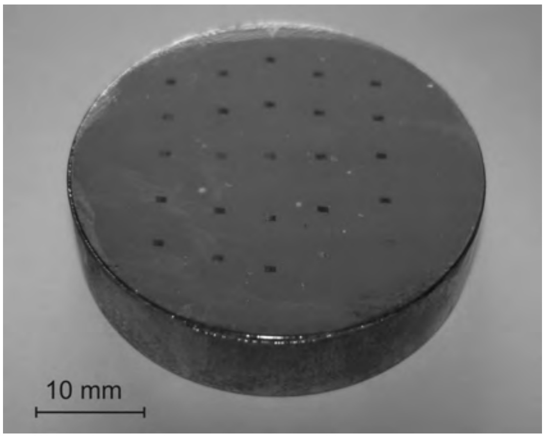

Figure 4.15.: Sample after laser irradiation. 25 dark spots each with 5 x 10^4 shots with an energy density of 0.3 J/cm^2

surface (neglecting mechanical anisotropy) [120].

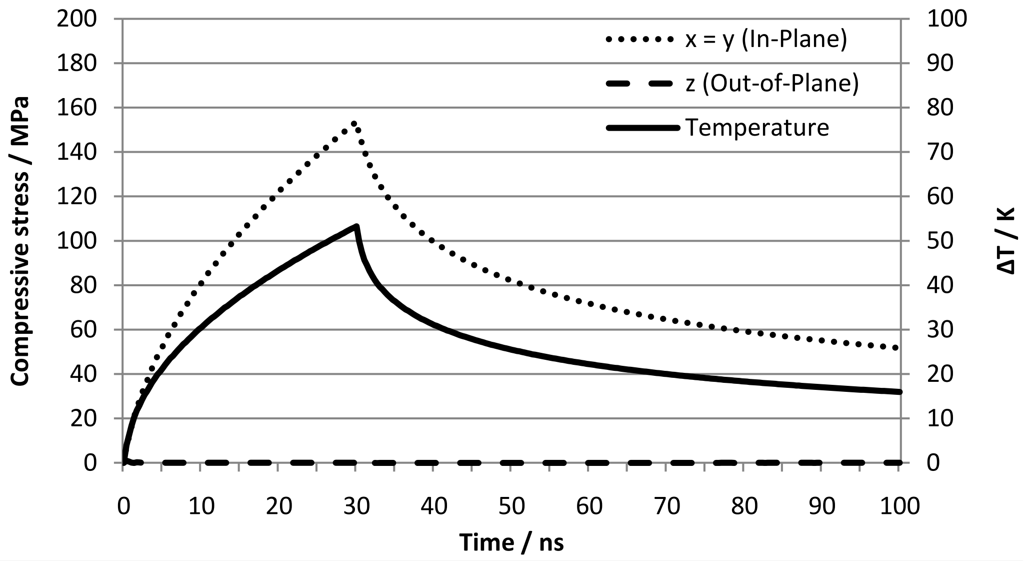

Figure 4.16.: Simulated temperature and stress component evolution in time during laser irradiation, assuming fully elastic isotropic material behaviour. Laser pulse length is 30 ns and energy density is 0.3 J/cm^2. In–Plane components (x = y) are similar compressive stresses whereas the out–of–plane component (z) remains zero

A surface point in the middle of the laser spot was considered, in order to exclude transient effects at the edges of the irradiated area. The laser pulse caused a temperature rise of about 53 K (pulse length only 30 ns). The in–plane components exhibited compressive stresses up to 157 MPa, whereas the out–of–plane component remained zero. Fig. 4.17 shows the stress component evolution as a function of distance to the surface. It can be seen that at the surface the in–plane components show high compressive stresses, with values similar to those at the temperature maximum in Fig. 4.16. The stresses decay to zero within a layer of 8 μm. In contrast, the out–of–plane component remained at zero through the entire layer.

This simulation shows that a perfect biaxial loading state can be assumed for all thermal fatigue experiments, as well as for the final application in the CLIC AS.

Due to the limited lifetime of the laser tube and despite the relatively high

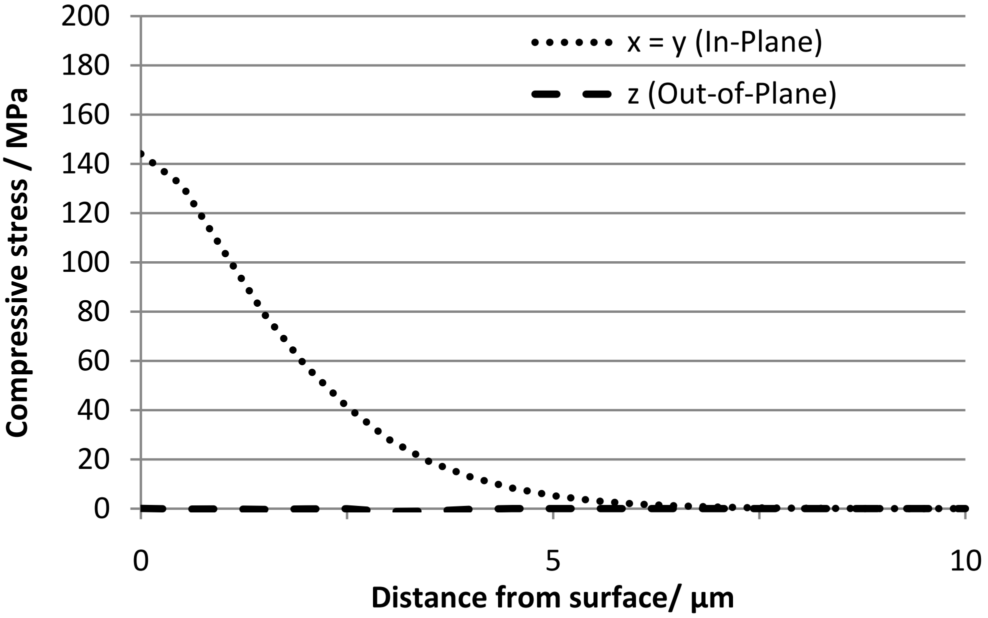

Figure 4.17.: Simulated temperature and stress component evolution in depth, same conditions as in Fig. 4.16. In–Plane components (x = y) decay in similar manners and become zero at a depth of 7 μm. Out–of–Plane component (z) stays zero.

repetition rate, this technique only allowed testing up to 10^7 cycles within a practical period of time, so the study was limited to the damage that might occur in the early stages of the CLIC AS. For the grain orientation dependence observation, each sample spot on the specimen was irradiated repetitively 5 x 10^4 times with 0.3 J/cm^2. The influence of individual grain orientations was determined on a statistical basis by observing 100 laser spots on 5 sample discs by SEM and EBSD.

In the past, laser fatigue tests have usually been performed on electro–polished half–hard (= fine grain) samples. As described in Chap. 4.1.1, the need for local roughness measurements in order to quantify the effect of grain orientation on the surface damage caused by fatigue made it necessary to use large grained samples. For this reason, complementary tests on annealed samples (= coarse grain) were performed. Indeed, due to their large grains, it was possible to inscribe a laser spot entirely within one grain.

We used the damage criterion proposed in [91] for quantitative LAF tests aimed at obtaining fatigue data in a form of a Woehler plot. Essentially, different areas were irradiated with different numbers of laser shots. Roughness measurements were performed ex–situ after the laser treatment. When the surface roughness exceeded a predefined threshold, the damage criterion was considered to have been fulfilled. Former CLIC related LAF studies [91] proposed a Ra value of 20 nm as the damage threshold, in view of the surface roughness requirements of CLIC AS discussed in Chap. 2.1, relating breakdown probability and Q-factor degradation. This threshold was used in this study.

4.4.4. Radio Frequency Fatigue (RFF)

To study RF fatigue, a mushroom–shaped RF cavity was used to produce a well–defined pattern of RF magnetic fields near the surface of an associated flat disc sample. A detailed description of the test bench can be found elsewhere [121, 122]. Fig. 4.18 shows a sample disc after fatigue testing. Pulsed RF magnetic fields (11,4 GHz; X–Band) were used to cyclically induce eddy currents with a repetition rate of 60 Hz. During one pulse (1.5 μs), such eddy currents cause Joule heating up to a calculated temperature rise of $\Delta T_{max} = 110$ K for the current test setup, which corresponds to a maximum thermal strain of $\epsilon_{th} = 1.8 \text{ x } 10^{-3}$. The heat load is equal for every grain oriented in a different crystallographic direction due to the isotropy of the electrical resistance in cubic materials [119, 38, 34]. The estimated thickness of the heated layer is approx. 30 μm [117]. This setup allows simulation of cyclic superficial heating, occurring in the real CLIC-AS due to RF at the nominal frequency of 12 GHz currently specified for CLIC [5]. This cyclic heating generates cyclic compressive biaxial stress, which results in fatigue damage. The magnetic field intensity and the cooling system were selected so as to ensure sufficient cooling between pulses in order to reach a steady state minimum temperature of approx. 60 °C. The effect of the inhomogeneous magnetic field distribution can be observed as a bright ring on the sample surface (Fig. 4.18), which corresponds to different fatigue damage, resulting from the variation of ΔT along the radius. The temperature variation, indicative of the strain/stress variation, can be calculated as a function of distance from the center through the field distribution function [121, 122].

The samples used for RF testing are in half–hard temper and are finished by

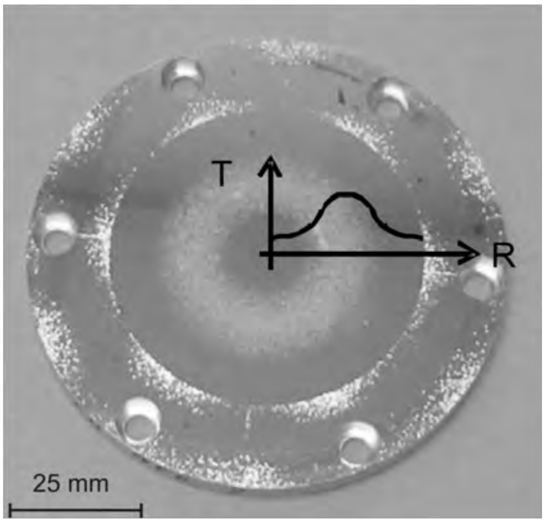

Figure 4.18.: RF fatigue test sample. The graph depicts the magnetic field intensity distribution along the radius: low intensity at $R = 0$, maximum intensity at $R = R_{Imax.} > 0$ and again low intensity at $R > R_{Imax.}$. The lighter shading in the inner ring marks the damaged area, where the maximum temperature rise of $\Delta T_{max} = 110$ K took place. The damage caused to the outer region, the result of sample clamping, is of no interest for the current purpose.

diamond fly–cut. Due to their fine grain size, a large number of grains with various orientations are situated in the area of maximum cyclic stress amplitude, making it possible to observe different grain orientations with different temperature loads using a single tested specimen.

In the absence of a damage criterion for this type of fatigue test, a new method for quantification of the fatigue–induced damage is proposed here. In the setup used, the cycle number was fixed at 10^7. The only free parameter on the sample was the radial position, hence the temperature amplitude. A threshold temperature amplitude can be defined as the temperature above which fatigue–induced damage can be microscopically observed on the sample surface. SEM inspections are performed along predefined radial lines of the sample, revealing the ring–shaped damaged area as in Fig. 4.18. The radial positions of the Starting and Ending Point (SP and EP) of the damaged area can be measured. The criterion for the SP/EP is considered to have been fulfilled if three areas covered with fatigue–related features (e.g. extrusions, SB, etc.) larger then 10 μm can be observed within on screen at 600 x magnification. The two radial positions for which SP and EP are in the center of the screen are then recorded. The procedure is repeated for three different radii. The SP and EP measurements can then be translated to local ΔT's via the known field distribution function defined by the RF cavity design [121, 122]. The damage criterion at 10^7 cycles is taken as the average of the temperatures corresponding to starting/ending of the damaged region.

Table 4.4 shows a summary of the applied testing parameters and compares the four test benches.

Features	CVF	USS	LAF	RFF
test bench	UTS 200 mech. testing	Ultrasonic swinger	Excimer Laser $\lambda = 248$ nm	Stnd. wave RF-cavity 11.4 GHz
Rep. rate	0.5 Hz	24 kHz	200 Hz	60 Hz
Cycles	0 - 10^6	10^6 - 10^{10}	0 - 10^7	10^7
Load	0 - 350 MPa	50 - 90 MPa	ΔT = 280 °C	$\Delta T_{max} = 110$ °C
Load Ratio	R = -1	R = -1	R = 0	R = 0
Sample type	Hour glass	Hour glass	Disc ⌀40 mm	Disc ⌀100 mm
Steady temp	25 °C	60 °C	25 °C	60 °C
Load distrib.	homog. on cross section	stress peak on surface	superficial in limited area	superficial radial distrib
Damage crit.	rupture	crack $\approx$ 1 mm	Ra $\leq$ 20 nm	ΔT of SP&EP

Table 4.4.: Comparison of the four fatigue test benches and commonly used test parameters

5. Results

This chapter presents the results obtained in the experiments described above, which form the basis for the discussion in Chap. 6. The first part of the chapter describes the general morphology of surface features and roughness developing during cycling with the different techniques, as described in Chap. 4.4. Special attention is paid to the different development of grains with particular orientations and GB surrounding areas. The second part presents the results for the evolution of hardness during cycling. The combination of roughening and hardening during cycling will be presented in the third part. The thin film characterisation and selected fatigue data will be presented at the end of the chapter.

5.1. Morphology of Fatigue Modified Surfaces

5.1.1. Morphology after Laser Fatigue

Fig. 5.1 shows the surface of an electropolished and laser fatigued H02 copper sample at different magnifications. The sample was subjected to 5 x 10^4 cycles at an equivalent Von Mises strain of ϵ_{eq} = 5.1 x 10^{-3}. In Fig. 5.1a the contrast between different areas is clearly visible. It will be shown in Chap. 5.1.4 that the contrast arises from different surface topographies, the result of different grain orientations. In Fig. 5.1b severe roughening is visible in several areas, in the form of regular and parallel–oriented lamellae, arranged in networks or cells. Spacing between lamellae is approx. 3 μm – 5 μm, and their height is approx. 1 μm. Higher magnification reveals an additional topography, the result of roughening, in Fig. 5.1c: densely packed regular, parallel–oriented lamellae, whose size and spacing are an order of magnitude smaller than those visible in Fig. 5.1b. These features correspond to the light areas in Fig. 5.1a. The

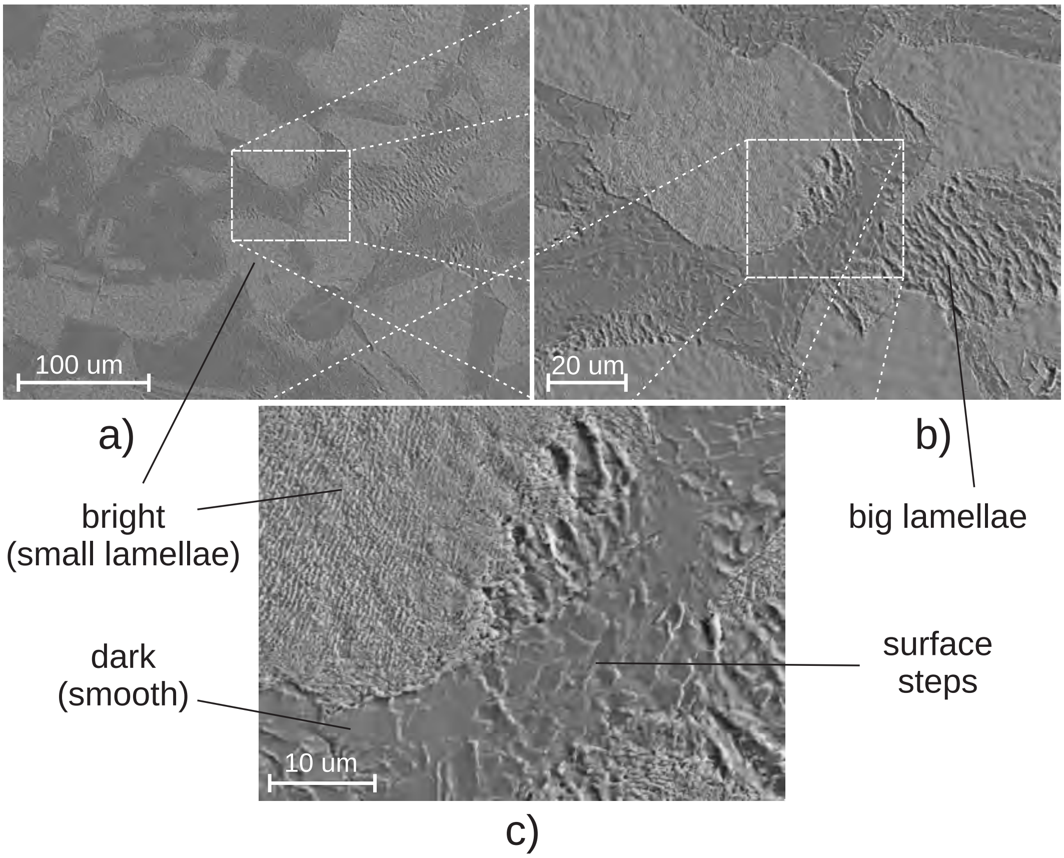

Figure 5.1.: SEM pictures of surface fatigued by laser with 0.3 J/cm^2 ($\Rightarrow \Delta$T = 180 K and ϵ_{eq} = 5.1 x 10^{-3}) after 5 x 10^4 cycles.

dark regions from Fig. 5.1a are shown at higher magnification (Fig. 5.1b and Fig. 5.1c) to have relatively smooth surfaces. Nevertheless they exhibit several surface scales oriented coherently.

Roughness Evolution versus Cycle Numbers in Laser Fatigue

As an example of the changes in surface topography during fatigue life, Fig. 5.2 shows a sequence of lower and higher magnification SEM pictures taken from an electro–polished H02 copper sample fatigued by laser at ϵ_{eq} = 3.4 x 10^{-3} for various numbers of cycles. In Fig. 5.2a (1.2 x 10^4 cycles), nucleation sites with surface features of 2 μm – 3 μm size appear sporadically while the surrounding areas appear smooth. In Fig. 5.2b (6 x 10^4 cycles), the density of the nucleation sites increases, and islands of the features develop around these sites and start

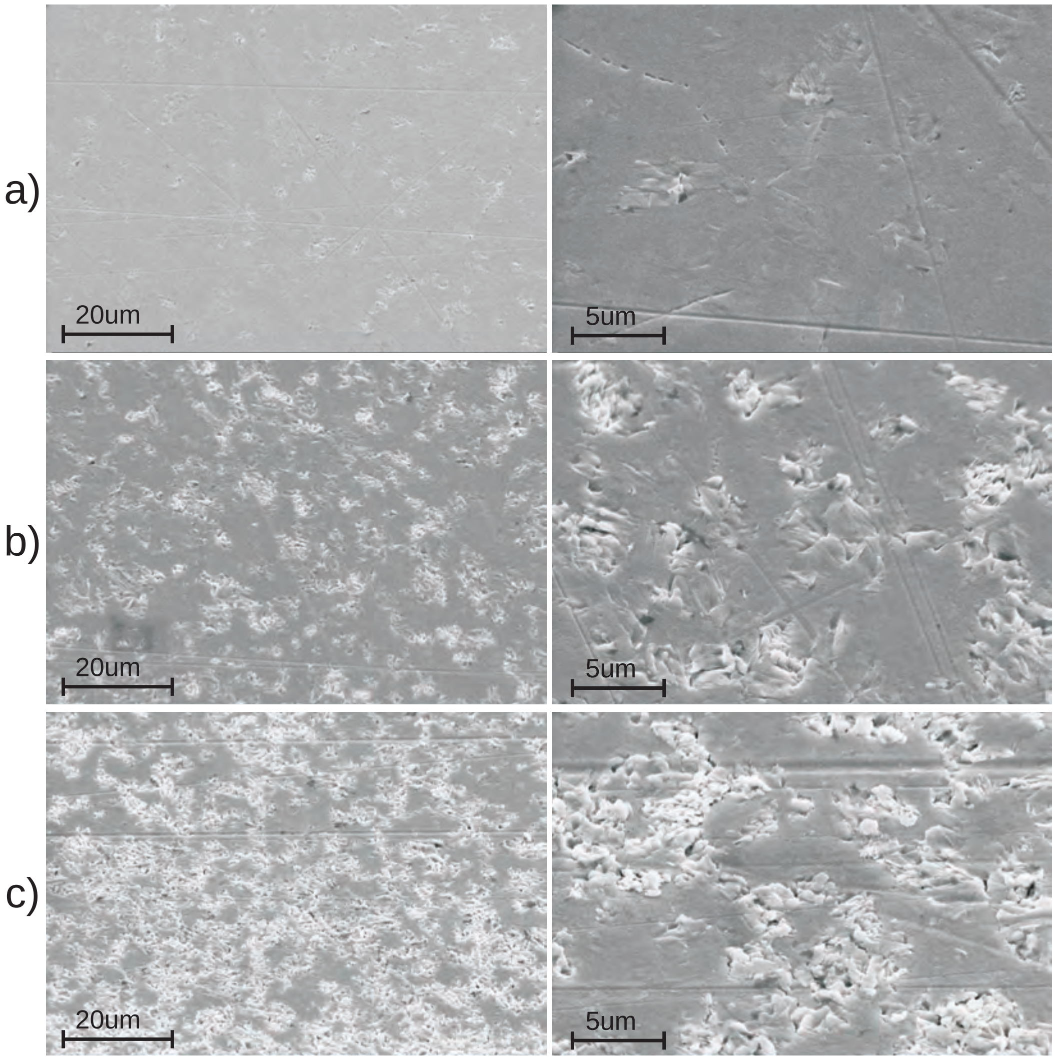

Figure 5.2.: SEM pictures of Cu H02 sample fatigued by laser with 0.2 J/cm^2 ($\Rightarrow \Delta$T = 120 K and ϵ_{eq} = 3.4 x 10^{-3}) after a) 1.2 x 10^4 b) 6 x 10^4 and c) 2.4 x 10^5 cycles.

to coalesce. In Fig. 5.2c (2.4 x 10^5 cycles), the islands have grown and formed continuous networks. The observed feature morphology is randomly oriented flakes.

Fig. 5.3 shows the roughness Ra as a function of cycle numbers for the sample observed in Fig. 5.2. The initial nucleation sites do not contribute much to the overall measured roughness. At 6 x 10^4 cycles, features start developing around the nucleation sites to form islands and roughening a significant portion of the

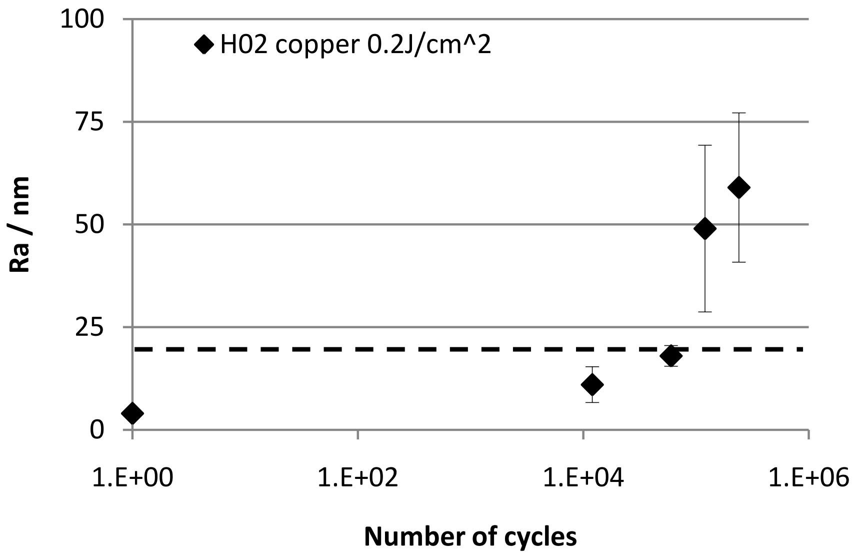

Figure 5.3.: Roughness evolution over cycle numbers from Fig. 5.2

surface, and the average roughness increases. Although *Ra* is a heavily averaged parameter, its value clearly increases when general roughening occurs at the higher cycle numbers. The measurements due to local roughness variations become more dispersed. The damage criterion threshold of $Ra = 0.02$ μm is exceeded just above 6 x 10^4 cycles.

Evolution of Roughness as a Function of Strain in Laser Fatigue

Fig. 5.4 shows the surface of an electro–polished H02 copper sample fatigued by laser to the same number of cycles (1.2 x 10^4), but with two different strain levels. The difference in surface morphology is clearly visible. The surface in Fig. 5.4a ($\epsilon_{eq} = 3.4$ x 10^{-3}) appears mainly smooth apart from sporadic roughness nucleation sites several μm in size, indicated by arrows. In Fig. 5.4b ($\epsilon_{eq} = 8.5$ x 10^{-3}), the surface shows clearly developed roughening in the form of networks of islands covering more than 50 % of the surface area. The morphology of early features close to the nucleation sites and those already well developed do not differ significantly.

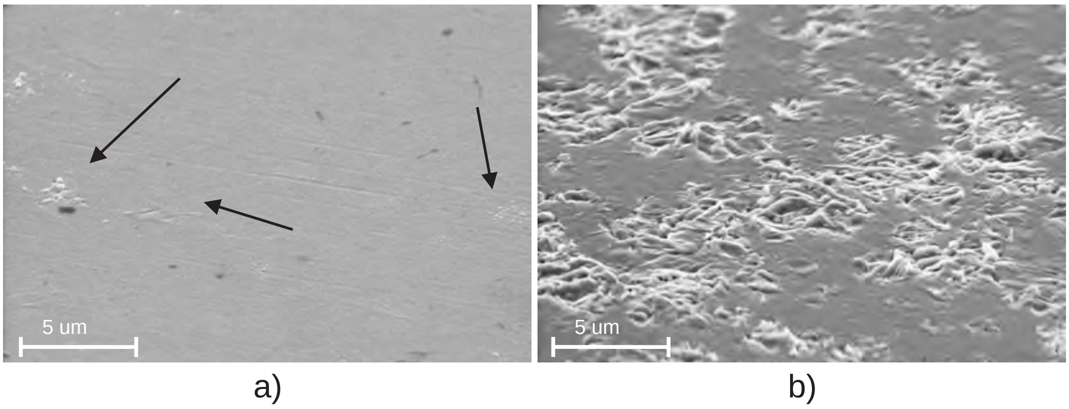

Figure 5.4.: SEM pictures of surface fatigued by laser after 1.2 x 10^4 cycles for a) 0.2 J/cm^2 ($\Rightarrow \Delta$T = 120 K and ϵ_{eq} = 3.4 x 10^{-3}) and b) 0.5 J/cm^2 ($\Rightarrow \Delta$T = 300 K and ϵ_{eq} = 8.5 x 10^{-3}).

5.1.2. Morphology after Radio Frequency Fatigue

Fig. 5.5 shows the surface of a RF fatigued H02 copper sample in the highest ΔT region. The sample was diamond fly–cut and then thermally cycled 10^7

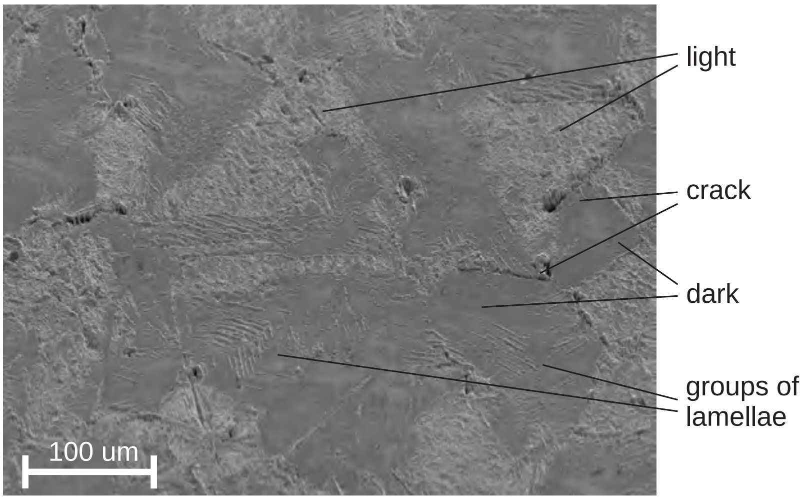

Figure 5.5.: SEM picture of Cu H02 sample fatigued by RF after 10^7 cycles in highest ΔT = 110 K ($\Rightarrow \epsilon_{eq}$ = 3.1 x 10^{-3}) region. Dark and light regions correspond to smooth and rough surfaces. Surface cracks can be observed in areas of extreme contrast.

times with ϵ_{eq} = 3.1 x 10^{-3} in the considered area. As with the laser fatigued sample in Fig. 5.1, lighter and darker areas, corresponding to different degrees of roughening, are present. Light regions have developed regular roughening, while elsewhere, randomly shaped features are observed. Dark regions appear to be mainly smooth, apart from rare groups of lamellae, very regularly oriented. The spacing between these lamellae is several μm and their height approx. 1 μm. At the boundary between light and dark regions, early stages of surface cracking is visible in some cases.

Evolution of Roughness as a Function of Strain in Radio Frequency Fatigue

Fig. 5.6 shows the surface of a diamond fly cut H02 copper sample fatigued by RF. Pictures are taken on the same sample in regions of different ΔT. The area in Fig. 5.6a was cycled with $\epsilon_{eq} \approx 2.3 \text{ x } 10^{-3}$. Most of the surface is smooth with limited roughening of the size of the average grain size (110 μm). In Fig. 5.6b the contrast between the roughened areas and the smooth appearing areas is more pronounced. The area was cycled with $\epsilon_{eq} \approx 3.1 \text{ x } 10^{-3}$. The density of the developed features is much higher. Smooth regions show development of isolated features. As will be shown in Chap. 5.1.4, the shape and size of

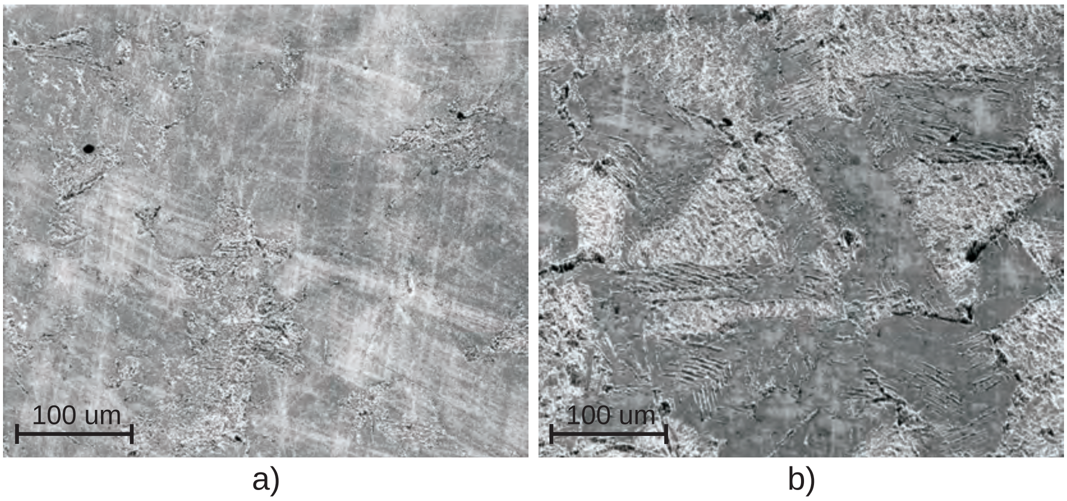

Figure 5.6.: SEM pictures of Cu H02 sample fatigued by RF after 10^7 cycles for a) ΔT $\approx$ 80 K ($\Rightarrow \epsilon_{eq} \approx 2.3 \text{ x } 10^{-3}$) and b) ΔT = 110 K ($\Rightarrow \epsilon_{eq} = 3.1 \text{ x } 10^{-3}$).

the observed areas suggest that smooth and rough regions can be attributed to individual grains, and develop from different crystallographic orientations.

5.1.3. Morphology after Ultrasonic Cycling

Fig. 5.7 is showing the surface of a USS fatigued sample in the region of highest local strain. The sample was electropolished and uniaxially mechanically loaded for 6 x 10^9 cycles at a maximum equivalent strain of $\epsilon_{eq} = 8.0$ x 10^{-4}. The sample surface shows a small number of areas with developed surface features. Very sharp, regularly oriented lamellae, that develop in groups of common orientation, form intermittent areas of damage. Typically, the lamella consists of an extrusion accompanied by an intrusion. The intruded parts develop small local cracks. The spacing between individual lamellae is approx. 2 μm – 5 μm and their height approx. 1 μm.

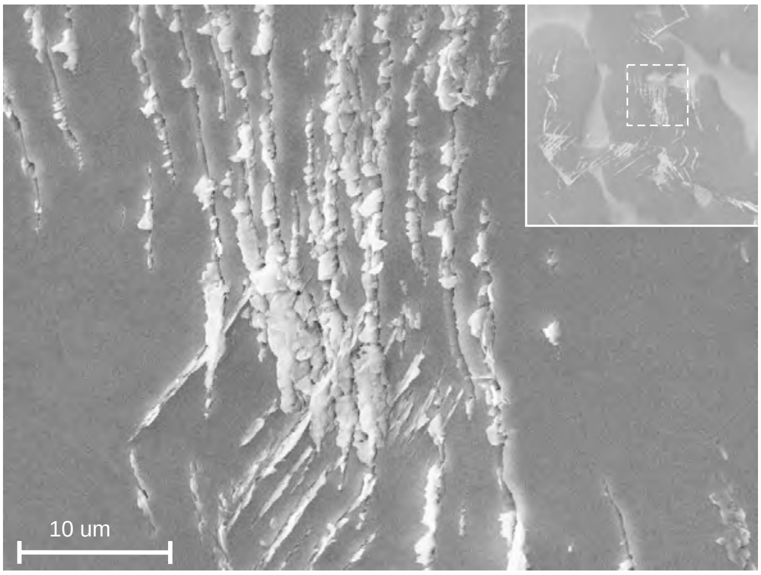

Figure 5.7.: SEM picture of USS fatigued copper H02 sample in highest load region ($\epsilon_{eq} = 8.0$ x 10^{-4}) showing individual lamellae.

Fig. 5.8 relates to an area lying on the same circumference as the area observed in Fig. 5.7. A significant crack, in length approx. 500 μm, is visible. Several secondary cracks branch off along the lamellae. Features on the right side of the crack show a very different morphology from the lamellae on the left, suggesting the crack follows a GB between grains of high misorientation. Features on the

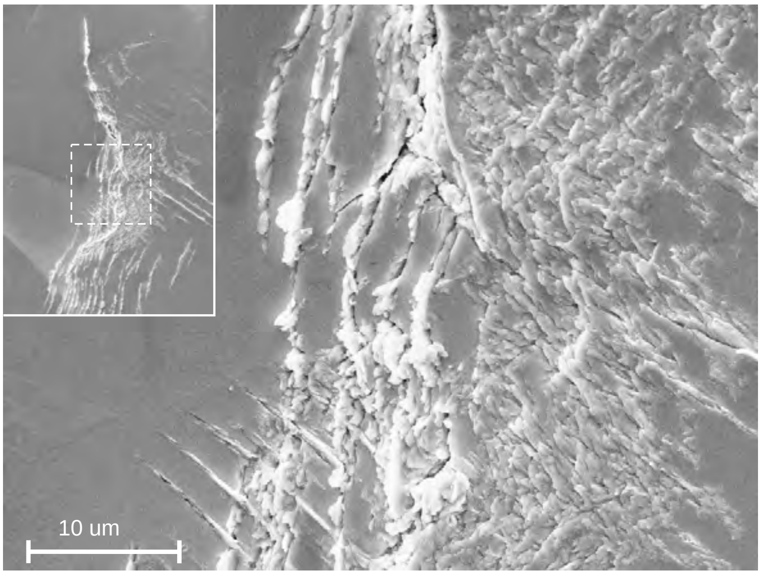

Figure 5.8.: SEM picture of USS fatigued sample in crack region. Higher magnification shows extrusions at main crack and secondary cracks.

right appear to be look like small irregular surface scales pointing in a common direction.

Evolution of Roughness as a Function of Strain in Ultrasonic Cycling

Fig. 5.9 shows the surface of an electropolished H02 copper sample fatigued by USS. The two pictures refer to areas where different levels of cyclic strain are applied due to the geometry of the sample. The region strained at a moderate level in Fig. 5.9a ($\epsilon_{eq} \approx 6.0$ x 10^{-4}) shows the nucleation of single lamellae developing in sporadic places, indicated by arrows. The length of these early lamellae is approx. 10 μm whereas the surrounding area appears smooth. Fig. 5.9b shows the surface of the region where the highest cyclic strain is applied ($\epsilon_{eq} = 8.0$ x 10^{-4}). Individual lamellae group in form of islands surrounding a visible crack. The lamellae are longer and more pronounced compared to the ones of Fig. 5.9a, suggesting a more advanced state. Large parts of the surrounding area appear smooth.

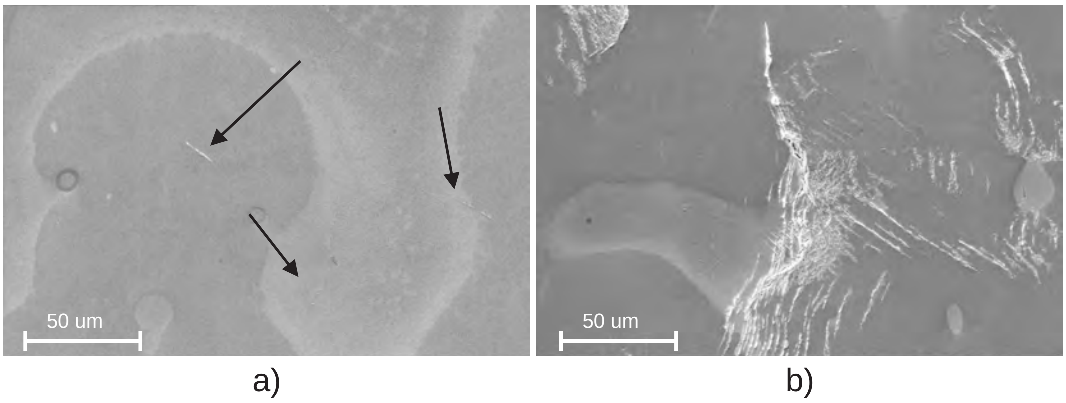

Figure 5.9.: SEM images of electropolished Cu H02 sample fatigued by USS with 6 x 10^9 cycles a) in a medium strain region ($\epsilon_{eq} \approx 6.0$ x 10^{-4}) and b) at the center of gage length ($\epsilon_{eq} = 8.0$ x 10^{-4})

5.1.4. Fatigue Induced Roughness versus Grain Orientation

Grain–Orientation Related Roughening after Laser Fatigue

Fig. 5.10 shows the surfaces of three different areas of an annealed and electropolished copper sample repeatedly irradiated in the LAF device, corresponding to grains oriented in the three main directions: [1 0 0], [1 1 1] and [1 1 0]. Fig. 5.11 shows the roughness values of those areas. Very different topographies and roughness values are observed at 5 x 10^4 cycles with the same applied cyclic strain of $\epsilon_{eq} = 5.1$ x 10^{-3}. The initial surface roughness, measured in a non irra-

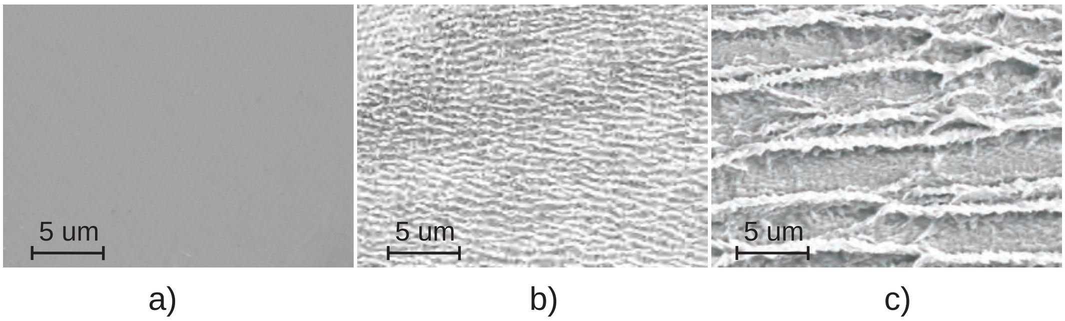

Figure 5.10.: SEM images of surfaces for grain orientation of a) [1 0 0], b)[1 1 1] and c)[1 1 0] following 5 x 10^4 laser cycles at 0.3 J/cm^2 ($\Rightarrow$ ΔT = 180 K and $\epsilon_{eq} = 5.1$ x 10^{-3})

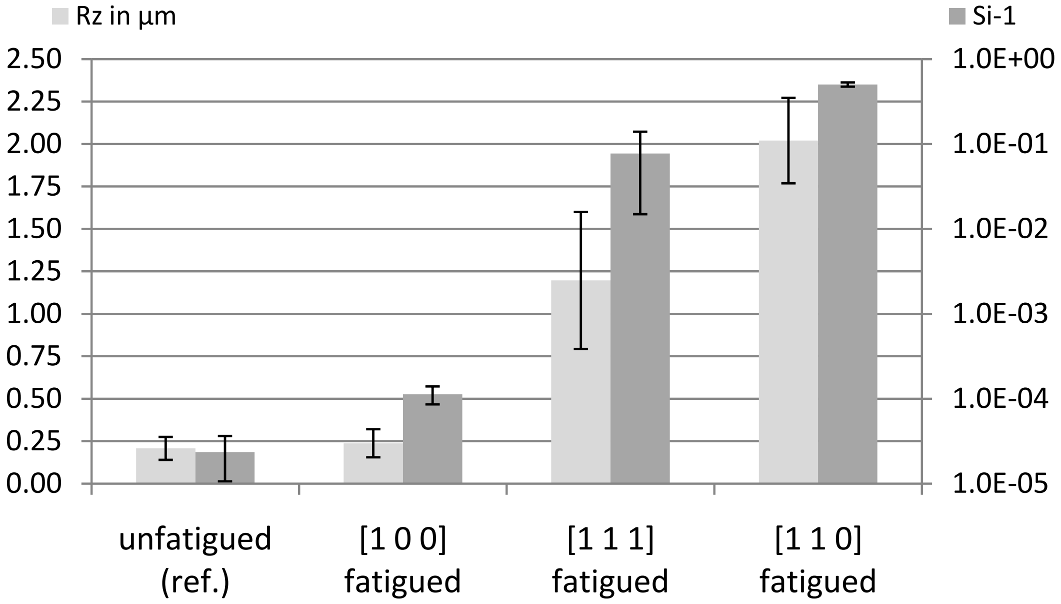

Figure 5.11.: Comparison of roughness measured in non–irradiated area (reference) and the grains in Fig. 5.10. For the definition of $SI - 1$ see Chap. 4.2.2. The [1 0 0] grain shows almost no difference with respect to the reference whereas the roughness in the [1 1 0] grain increased significantly during the cycling. The roughness values of the [1 1 1] grain are between [1 0 0] and [1 1 0].

diated area for reference, is very low ($Rz = 207 \pm 67$ nm; $SI - 1 = 2.35$ x 10^{-5} $\pm$ 1.29 x 10^{-5}). The [1 0 0] grain remains very smooth after cycling with Rz and $SI-1$ comparable to the reference value ($Rz = 238 \pm 83$ nm; $SI-1 = 1.13$ x 10^{-4} $\pm$ 0.3 x 10^{-4}). The [1 1 1] grain after cycling shows regular protrusions spaced less than 1 μm apart. Both roughness values, Rz and $SI - 1$, are significantly larger than the reference values ($Rz = 1.2 \pm 0.4$ μm; $SI - 1 = 7.7$ x 10^{-2} $\pm$ 6.2 x 10^{-2}). The [1 1 0] grain after cycling shows even larger regular protrusions, with wider spacing (4 – 5 μm), and roughness values that are the highest observed among the three main directions ($Rz = 2.0 \pm 0.25$ μm; $SI - 1 = 0.5$ $\pm$ 2.8 x 10^{-2}).

SF calculations for the thermal (biaxial) load case are performed for each of the three main orientations. The results are presented in the Appendix (Fig. A.1).

Grain–Orientation Related Roughening after Radio Frequency Fatigue

Fig. 5.12 shows the surface of a diamond fly cut H02 copper sample subjected to RF fatigue at $\epsilon_{eq} = 3.1 \text{ x } 10^{-3}$ for 10^7 cycles. EBSD was used to identify local grain orientations. GBs are highlighted by contrast, and are consistent with GBs identified by EBSD. Roughness can be associated with corresponding grain orientations: [1 0 0] grains appear dark, hence smooth, and show several individual groups of lamellae. Grains of [1 1 1] orientation show severe roughening. [1 1 0] oriented grains are not present within the observed area. Cracks did not initiate along GBs between [1 0 0] and [1 1 1] grains, whereas they initiated at GBs elsewhere.

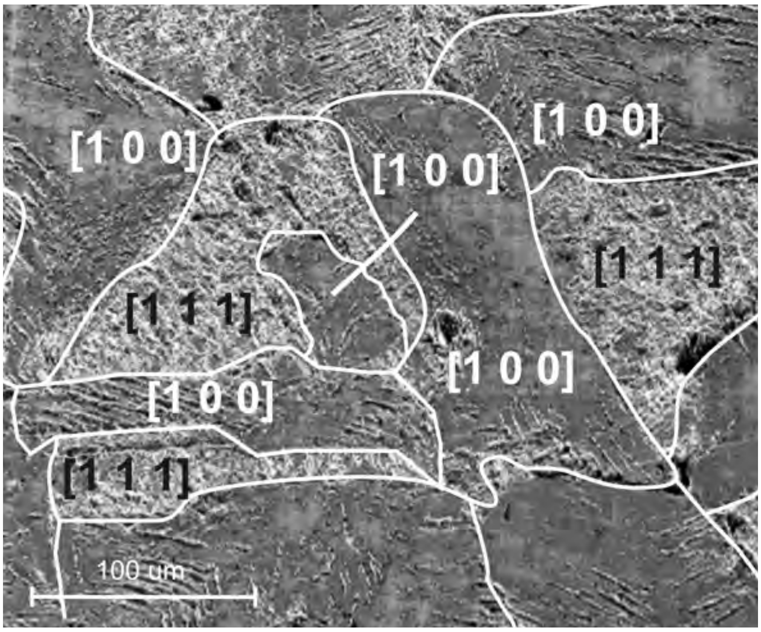

Figure 5.12.: SEM pictures of Cu H02 sample fatigued by RF after 10^7 cycles in ΔT = 110 K region ($\Rightarrow \epsilon_{eq} = 3.1 \text{ x } 10^{-3}$). Only main grain orientations are highlighted as identified by EBSD.

Grain–Orientation Related Roughening after Ultrasonic Cycling

Fig. 5.13 shows the surface of an electropolished and annealed copper sample fatigued in the USS device with $2.2 \text{ x } 10^{10}$ cycles and a strain amplitude of $\epsilon_{eq} = 8.0 \text{ x } 10^{-4}$. Several grains with an orientation close to [1 1 1], such

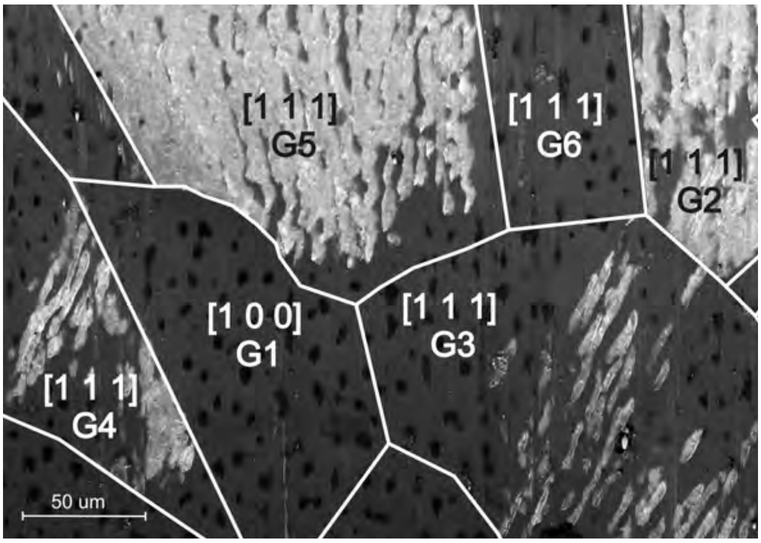

Figure 5.13.: SEM picture of USS sample in center of gage length ($\epsilon_{eq} = 8.0 \text{ x } 10^{-4}$). Grain orientations and boundaries high lighted as identified by EBSD. Grains are numbered G1 to G6. Central [1 0 0] grain shows no roughening; [1 1 1] grains show severe, moderate or no roughening. Dark spots are electro polishing artifacts.

as grains G2 to G6, are located around a central grain close to the [1 0 0] orientation (G1). Individual surface roughening can be qualitatively classified into three categories:

1) severe roughening
2) moderate roughening
3) no roughening.

Grains G2 and G5 show severe roughening, with a high density of overlapping lamellae covering nearly the entire grain area. Grains G3 and G4 show moderate roughening with apparently the same size of lamellae but at a lower density, hence larger spacing (2 – 5 μm). Groups of these lamellae are found on parts of the grains. Grains G1 ([1 0 0] orientation) and G6 ([1 1 1] orientation) appear dark and do not show roughening at all.

Tab. 5.1 lists the EBSD data collected for each grain. The deviation of the grains from the main orientations is as high as 10° in some cases (Euler angles for ideal orientation are listed in Tab. 4.2). For G1 the deviation is even larger (17.8°). The cube icon shows the orientation of the corresponding elementary

Grain No	Euler 1	Euler 2	Euler 3	Illustr.	SF 1	SF2	Roughen.
G1	143°	17.8°	68.0°	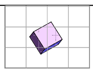	0.49	0.41	no
G2	350°	45.2°	34.7°	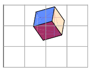	0.50	0.45	severe
G3	212°	46.4°	53.4°	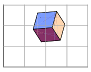	0.49	0.42	moderate
G4	222°	48.8°	49.8°	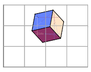	0.49	0.44	moderate
G5	350°	45.5°	34.2°	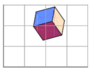	0.50	0.45	severe
G6	278°	43.3°	51.6°	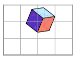	0.41	0.40	no

Table 5.1.: Euler angles of grains in Fig. 5.13 and illustration of orientation of elementary cell with respecto to the surface. SF on primary and secondary slip system SF1 and SF2. Qualitative roughening category.

cell with respect to the surface. Finally the SF values on the primary and on the secondary slip system are listed together with the severity of roughening. SF calculations are performed with precise Euler angles and presented in the Appendix (Fig. A.5).

Additionally, SF calculations were performed for each ideal out–of–plane main orientation with different in–plane rotations. The results are also presented in the Appendix (Fig. A.2 to A.4).

5.1.5. Morphology of Surface Features near Grain Boundary

Morphology of Surface Features Near Grain Boundary after Laser Fatigue

Fig. 5.14 shows the GB zone on an electro polished annealed copper sample fatigued by LAF at $\epsilon_{eq} = 5.1 \text{ x } 10^{-3}$ for 5 x 10^4 cycles. The orientations are highlighted as identified by EBSD, whereas the GB mark precisely the boundaries of the topography contrast. In the vicinity of the [1 0 0] – [1 1 1] GB, the surface shows peculiar aspects. The smooth [1 0 0] grain exhibits a band of approx. 10 μm in width, showing a low density of surface scales. On the opposite side of the GB, within the [1 1 1] grain, a different orientation of lamellae is observed with respect to the interior of the grain: within a band of approx.

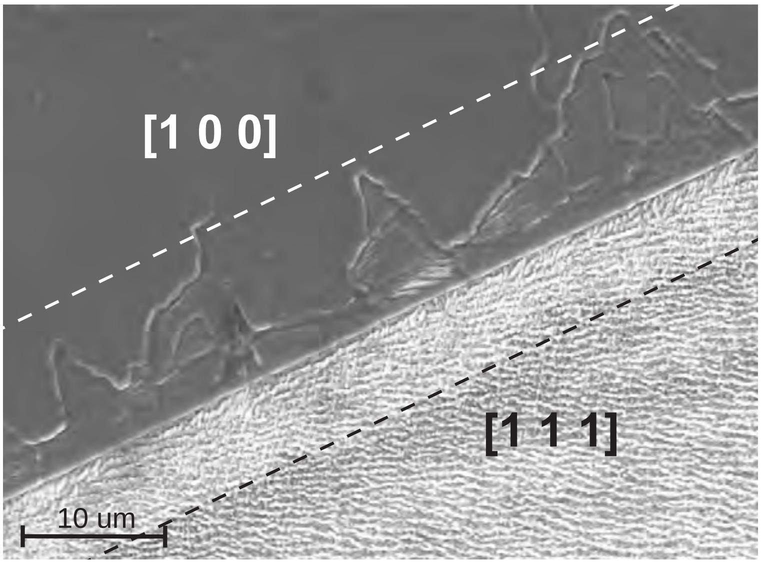

Figure 5.14.: SEM image of annealed copper surface fatigued by laser with 0.3 J/cm^2 ($\Rightarrow \Delta$T = 180 K and ϵ_{eq} = 5.1 x 10^{-3}) after 5 x 10^4 cycles. GB between [1 0 0] and [1 1 1] grain. Surface modification bands are visible in GB vicinity.

7 μm in width, the lamellae tend to be parallel to the GB. In the interior of the grain they are observed to be along a (2 1 1)–type axis as identified by EBSD. The width of both bands coincides approximately with the thickness of the heated layer in the LAF ($\approx$ 10μm). These bands near the GB are referred to here as “modification bands”.

Fig. 5.15 shows two different areas close to a GB on a sample treated with the same parameters as the sample in Fig. 5.14. the two GBs are of the same type, [1 0 0] – [1 1 0], but oriented differently with respect to the surface features in the [1 1 0] grain. In Fig. 5.15a the [1 0 0] grain clearly shows a 10 μm modification band along the GB where surface scales appear. The height of the lamellae in the [1 1 0] grain decreases towards the GB within a band of a width of approx. 5 μm. The lamellae network of the [1 1 0] grain is nearly perpendicular to the GB. On the other hand in Fig. 5.15b the lamellae network of the [1 1 0] grain is nearly parallel to the GB, and there is no sign of a modification band in either of the two grains.

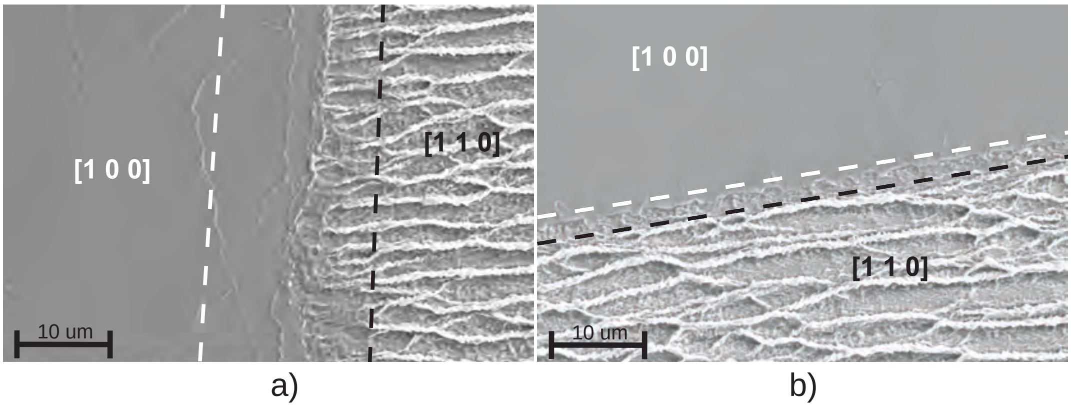

a) b)

Figure 5.15.: SEM image of annealed copper surface fatigued by laser with 0.3 J/cm^2 ($\Rightarrow \Delta$T = 180 K hence ϵ_{eq} = 5.1 x 10^{-3}) after 5 x 10^4 cycles. GB's of type: [1 0 0] – [1 1 0]. Plot a) large modification zone visible. Plot b) no modification zone visible.

Morphology of Surface Features Near Grain Boundary after Radio Frequency Fatigue

Fig. 5.16 shows a GB region on a diamond fly cut H02 copper sample fatigued by RF after 10^7 cycles with ϵ_{eq} = 3.1 x 10^{-3}. The otherwise smooth appearance of the [1 0 0] grain is disturbed in the GB vicinity. Irregular features extend approx. 30 μm into the interior of the grain. Since the grain size is 110 μm, the effect of the GB affects most of the grain interior. On the [1 1 1] grain the height of the parallel overlapping lamellae decreases towards the GB within a band approx. 15 μm in width. No severe intrusion or crack initiation is visible at the boundary between these two grains. The width of both modification bands coincides approximately with the heated layer thickness in the RFF ($\approx$ 30μm).

5.2. Fatigue–Induced Hardening

Most of the hardness measurements in this study were performed by using a Vickers diamond pyramid to indent the fatigued surface under very low weight, at the lower end of the load range of the microhardness technique. Indenting with a selected load of 10 g resulted in indent sizes between 18 μm and 23 μm and indentation depths between 3 μm and 4μm. As the maximum average roughness

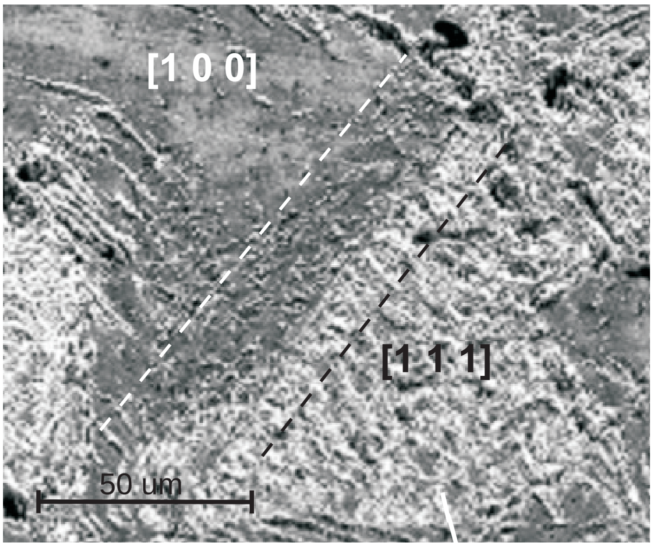

Figure 5.16.: SEM pictures of Cu H02 sample fatigued by RF after 10^7 cycles in highest ΔT = 110 K region ($\Rightarrow \epsilon_{eq}$ = 3.1 x 10^{-3}). GB between [1 0 0] and [1 1 1] grain. Large modification zone visible in GB vicinity.

(Ra = 250 nm) is approx. 6% – 9% of the indentation depth, the validity of the obtained hardness results could be challanged. ASTM standard 348-09 [98], covering the microhardness technique used here, specifies only the clear visibility (definition) of the perimeter of the indentation. Since this condition was met in the current measurement campaign, the hardness results are considered as valid.

5.2.1. Hardness as a Function of Cycle Number

Fig. 5.17 shows the hardness changing as a function of cycle numbers for an annealed copper sample fatigued by laser at ϵ_{eq} = 5.1 x 10^{-3}. Each data point averages the hardness resulting from 10 hardness imprints which were randomly distributed within the laser spots. The hardness increases continuously with increasing cycle number, from initially 47 HV to 69 HV.

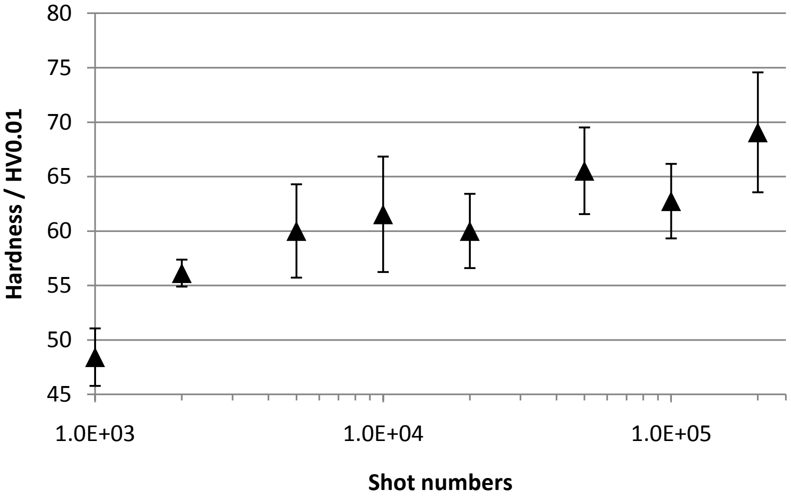

Figure 5.17.: Hardness (HV) as a function of cycle numbers on annealed copper sample, fatigued by laser at 0.3 J/cm^2 ($\Rightarrow \Delta$T = 180 K and ϵ_{eq} = 5.1 x 10^{-3}).

5.2.2. Hardness as a Function of Max. Equivalent Strain

Fig. 5.18 shows the microhardness of RFF fatigued samples after 10^7 cycles at maximum ϵ_{eq} = 3.1 x 10^{-3} as a function of radial position, hence ϵ_{eq}. It can

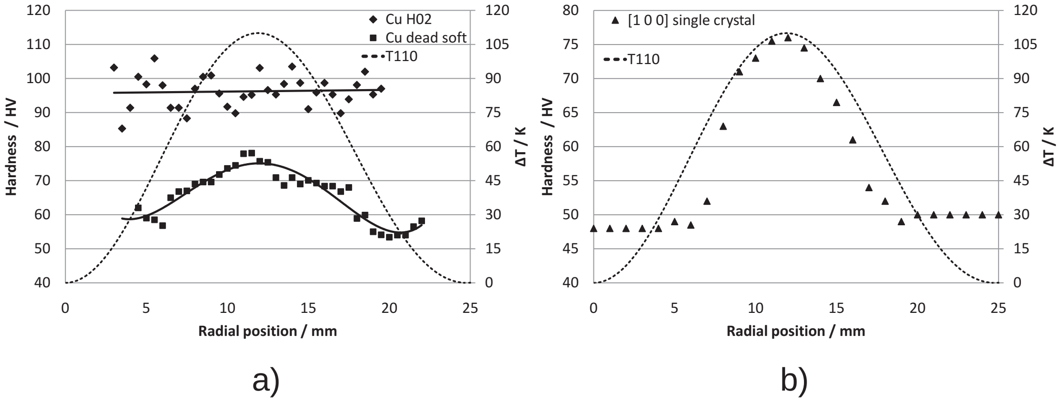

Figure 5.18.: Plot of microhardness as a function of radial position on RFF fatigued samples after 10^7 cycles at maximum ΔT = 110 K ($\Rightarrow$ ϵ_{eq} = 3.1 x 10^{-3}). Plot a) H02-Cu and dead–soft annealed Cu. Plot b) single crystal oriented in [1 0 0] direction (courtesy of KEK and SLAC). T110 represents the calculated radial distribution of ΔT.

be seen from Fig. 5.18a that a correlation exists between the ΔT curve and the hardness increase observed on the dead soft annealed sample. The highest hardness values occur in the region of highest cyclic temperature load, hence highest ϵ_{eq}. On the other hand, on the H02 temper sample the hardness does not increase with thermal cycling. Fig. 5.18b illustrates the aforementioned correlation on a single crystal sample, oriented in [1 0 0] direction: the hardness follows nicely the shape of the cyclic temperature profile with an offset. In Fig. 5.18a and Fig. 5.18b the hardness increase is only observed when ΔT is above 60 K ($\Rightarrow \epsilon_{eq} = 1.7 \text{ x } 10^{-3}$). Below this strain load no hardness increase is detectable. Fig. 5.19 shows the hardness versus cyclic strain plot for the data presented in Fig. 5.18b for the [1 0 0] single crystal. Below the threshold

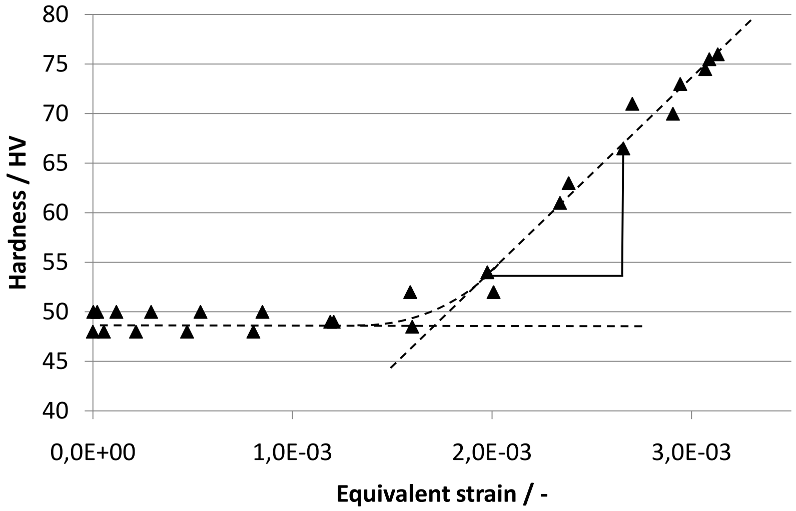

Figure 5.19.: Micro hardness as a function of equivalent strain on RFF fatigued [1 0 0] single crystal after 10^7 cycles at maximum ΔT = 110 K ($\Rightarrow \epsilon_{eq} = 3.1 \text{ x } 10^{-3}$).

strain of 1.7 x 10^{-3}, corresponding to 60 K, the hardness does not respond to cycling. Above this threshold, a linear increase of hardness with cyclic strain can be observed up to the highest strain applied, 3.1 x 10^{-3}, corresponding to the maximum temperature load of ΔT = 110 K. The slope of the hardness increase is 1.7 x 10^4 HVm/m.

5.2.3. Hardness as a Function of Grain Orientation

Fig. 5.20 shows a plot of hardness increase after LAF cycling applied to grains of different crystallographic orientations. Two dead–soft annealed and electropolished copper samples were fatigued with the LAF device during 5 x 10^4 cycles with ϵ_{eq} = 5.1 x 10^{-3}. Hardness values were measured for non–fatigued and fatigued areas within the same grain directions. Coherence of orientation was verified by EBSD. The minimum distance to the visible border of the laser spot for the non–fatigued measurements was 100 μm. Beyond this distance, it is assumed that irradiation, hence surface heating, is negligible (compare thickness of heated layer in LAF, approx. 10 μm). The hardness of the [1 0 0] orientation was measured twice independently in two similar laser spots to verify the reproducibility of fatigue cycling and hardness measurements. Since the difference between the two corresponding values is lower than 3 % despite the scatter of the hardness measurement, the hardness values are considered as consistent.

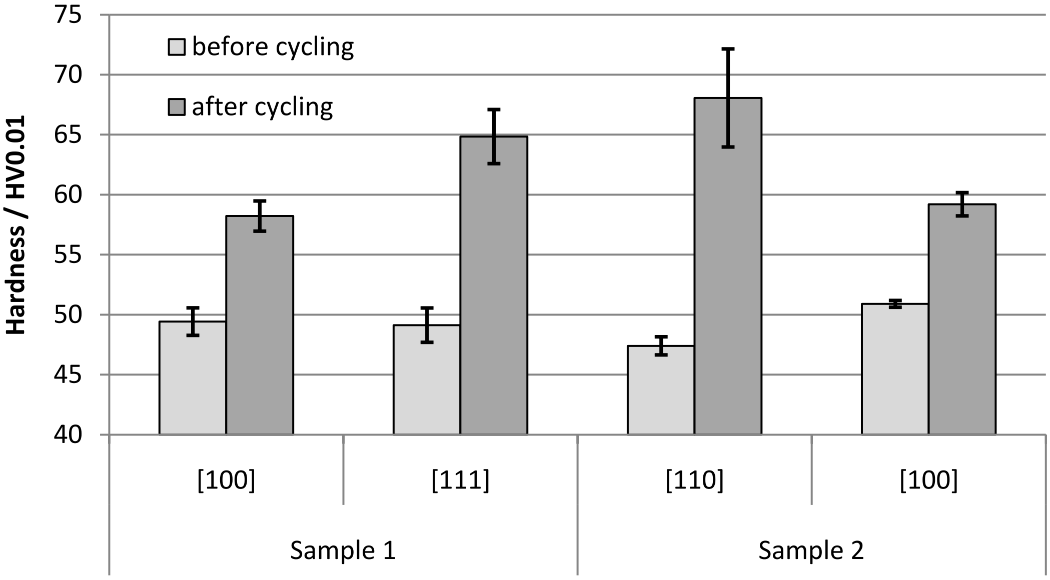

Figure 5.20.: Hardness increase of main orientations after 5 x 10^4 cycles with 0.3 J/cm^2 ($\Rightarrow \Delta$T = 180 K and ϵ_{eq} = 5.1 x 10^{-3})

All orientations show some degree of hardness increase after cycling. The hardness increase of the [1 0 0] grain (49 HV → 58 HV $\cong$ +17 %) is the smallest, followed by that of the [1 1 1] grain (49 HV → 65 HV $\cong$ +32 %). The highest was in the [1 1 0] orientation (47 HV → 68 HV $\cong$ +44 %).

5.3. Combined Roughening and Hardening

The results presented so far concerning the fatigue–induced roughening and the hardening suggest that the two mechanisms may be linked. This section will now combine the presented data in order to highlight this link in a direct way.

5.3.1. Roughening and Hardening as a Function of Cycle Number

Fig. 5.21 juxtaposes the increases in roughness and hardness with cycle number, measured on an annealed sample and fatigued by LAF with $\epsilon_{eq} = 5.1 \text{ x } 10^{-3}$. The measurement averages the hardness resulting from 10 hardness imprints, which were randomly distributed within the laser spots. The roughness value is an average of 3 independent measurements performed on three different laser spots cycled with the same parameters. The roughness measurement suffered from the inhomogeneously distributed fatigue–induced roughness and therefore exhibits considerable scatter. Hardness increases continuously with cycle number from initially 47 HV to 69 HV. Similarly, *Ra* shows a constant increase from initially 50 nm to approx. 200 nm. This trend is even more evident in Fig. 5.22, where

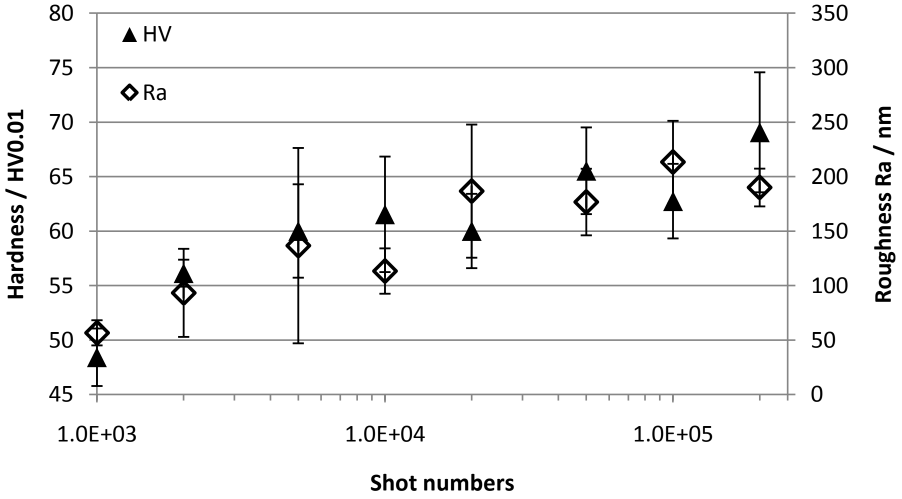

Figure 5.21.: Comparison of Hardness (HV) with surface roughness (*Ra*) over cycle numbers on annealed copper sample, fatigued by laser at 0.3 J/cm^2 ($\Rightarrow \Delta T = 180$ K and $\epsilon_{eq} = 5.1 \text{ x } 10^{-3}$).

roughness over hardness is plotted directly. It can be seen that during fatigue

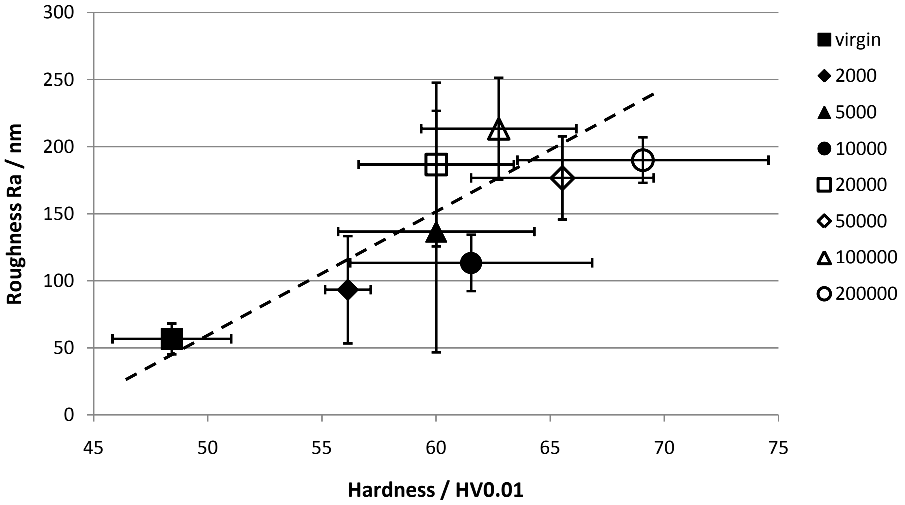

Figure 5.22.: Surface roughness (Ra) over Hardness (HV) for lower (filled symbols) and higher (hollow symbols) cycle numbers on annealed copper sample. Same data as in Fig. 5.21.

life, surfaces become harder and more rough, especially for high numbers of cycles (hollow symbols).

5.3.2. Roughening and Hardening as a Function of Grain Orientation

For the three main grain orientations of a dead soft annealed sample, Fig. 5.23 shows a graph plotting (Rz) versus HV (plot a) and another plotting the increases in (Rz) versus the increase in HV (plot b). Starting from initially equally smooth surface with slightly different hardness values, the [1 1 0] direction shows the highest roughening/hardening combination (87 nm/HV), followed by the [1 1 1] direction (63 nm/HV) and the [1 0 0] direction (4 nm/HV). Fig. 5.23b shows that the roughness increase versus hardness increase data points for all three main orientations lie on a common straight line with a slope of approx. 154 nm/HV.

Fig. 5.24 plots the measured hardness and strain data for the [1 0 0] single crystal fatigued by RFF (see Fig. 5.18b and Fig. 5.19) together with the data

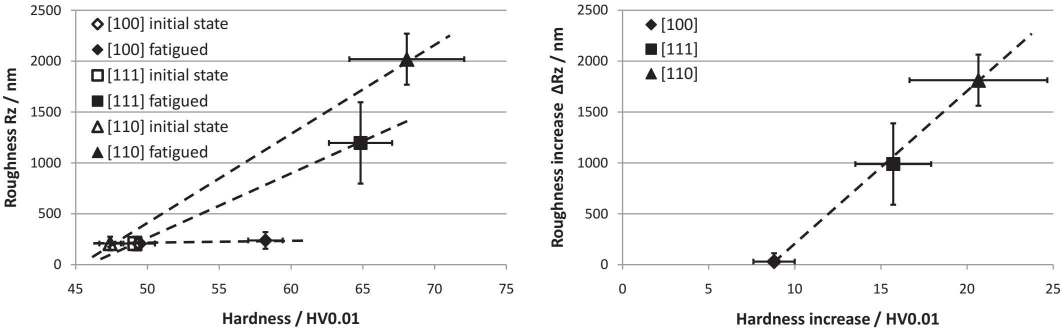

a) b)

Figure 5.23.: a) Roughness and hardness of the main orientations in the initial state and after 5 x 10^4 cycles with 0.3 J/cm^2 ($\Rightarrow \Delta$T = 180 K and ϵ_{eq} = 5.1 x 10^{-3}). b) Same data as in a) but with the roughness increase plotted directly versus the hardness increase.

obtained from the areas within a [1 0 0] grain fatigued by LAF. The initial hardness of the [1 0 0] single crystal fatigued by RFF and the area in a [1 0 0] grain fatigued by LAF are equal, wherefore here the same strain threshold point of the RFF sample is assumed also for the LAF sample (1.7 x 10^{-3}). The LAF sample shows a significantly lower slope in hardening due to cyclic straining compared to the RFF sample (2.8 x 10^3 HVm/m in LAF compared to 1.7 x 10^4 HVm/m in RFF). This may be due to two reasons:

1) The penetration depth of the microhardness measurements on this soft copper is between 3 μm and 5 μm. The heated layer in the RFF experiments is approx. 30 μm, whereas in LAF it is only approx. 10 μm. The influence of the soft underlying copper substrate is therefore more pronounced in LAF and decreases the hardness values measured.

2) The shown RFF sample underwent 10^7 thermal cycles whereas the LAF samples underwent only 5 x 10^4 cycles. Hence the RFF sample had more time to create, move and accumulate dislocations and therefore exhibits higher hardness.

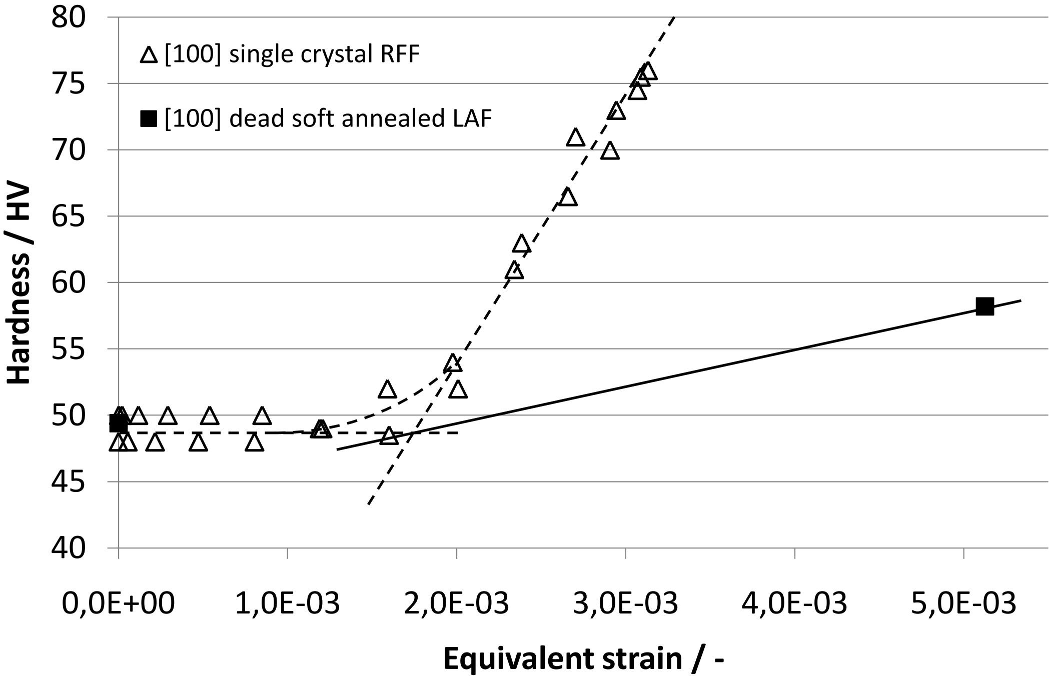

Figure 5.24.: Microhardness as a function of equivalent strain on RFF fatigued [1 0 0] copper single crystal after 10^7 cycles at maximum ΔT = 110 K ($\Rightarrow \epsilon_{eq}$ = 3.1 x 10^{-3}) compared to dead–soft annealed copper LAF fatigued after 5 x 10^4 cycles with 0.3 J/cm^2 ($\Rightarrow \Delta$T = 180 K and ϵ_{eq} = 5.1 x 10^{-3})

5.4. Thin Film Characterisation

5.4.1. Grain Size Measurements

Since grain size is an important parameter influencing the fatigue behaviour of a material, the grain size of each observed thin film was measured with EBSD. As the expected grain size of the thin films was inferior to 1 μm, the EBSD scans were performed with step sizes of 0.1 μm. After a parameter optimisation it was possible to perform scans of the dimension of 140 μm x 80 μm over night (12 h). In the EBSD data analysis, grains having an area inferior to 0.05 μm^2 were discarded because of the low number of acquisitions within a single grain.

Fig. 5.25 shows the results of the sample twin pair SS3 and Cu3, coated at the same time with the same coating parameters. The grain size and morphology are visible in Fig. 5.25a and Fig. 5.25b respectively. SS3 shows a large number of

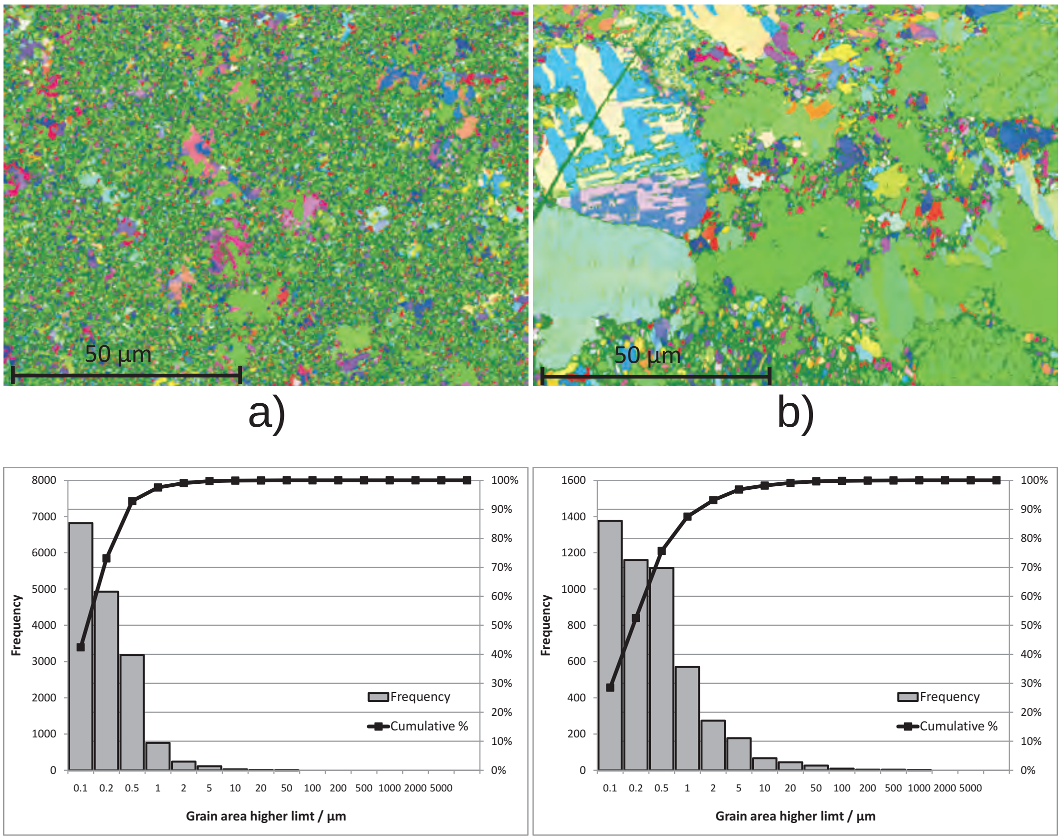

a) b)

c) d)

Figure 5.25.: a) and b) grain maps of SS3 and Cu3 as obtained by EBSD as basis for grain size calculations. c) and d) logarithmic grain area distribution of SS3 and Cu3.

grains in the submicrometer regime, and with randomly distributed grains in the order of 10 μm in diameter. Cu3 on the other hand features a high area fraction, with very large grains in the order of 100 μm in diameter embedded in numerous grains of 1 μm – 5 μm. Since the grain size distribution ranges over several orders of magnitude to in all thin films observed, a logarithmic classification of grain areas was chosen. Fig. 5.25c and Fig. 5.25d show the grain area distribution of the thin films of Fig. 5.25a and Fig. 5.25b respectively. The width of the distribution is a major criterion for the homogeneity of the micro structure in terms of grain size: 90 % of all grains in Fig. 5.25a and c (SS3) are smaller than 0.5 μm^2 whereas in Fig. 5.25b and d (Cu3) 90 % of all grains are smaller than 2 μm^2. Cu3 is thus less homogeneous in terms of grain area distribution, than SS3. The 90 % value and the 99 % value are used to characterise the grain size of the thin films. Tab. 5.2 summarizes the grain area distributions of all thin films observed. Basically all thin films feature grain sizes with highest occurrence at the lower end of the explored grain size range. The EBSD scans and the corresponding grain area distribution for the different thin films can be found in the Appendix (Fig. A.6 to Fig. A.15).

Grain area μm^2	SS2	Cu2	SS3	Cu3	SS4	Cu4	SS5	Cu5	SS6	Cu6
90% $\leq$ than	5	5	0.5	2	1	1	1	1	1	1
99% $\leq$ than	50	100	2	20	5	5	5	10	5	10

Table 5.2.: Average grain areas of the thin films measured with EBSD

5.4.2. Texture Analysis

Tab. 5.3 lists the measured diffraction data of copper powder together with the data obtained from the PDF file. The data measured with XRD shows good correspondence to the reference data from the PDF file in terms of relative intensity and angular position of the intensity maximum. This measurement is

Reflection	I (PDF) %	I (Meas.) %	Error %	2θ (PDF) °	2θ (Meas.) °	Error °
1 1 1	100	100	0.0	43.298	43.215	0.083
2 0 0	46	43	3.0	50.434	50.290	0.144
2 2 0	20	20	0.1	74.133	73.968	0.165
3 1 1	17	19	1.8	89.934	89.747	0.187
2 2 2	5	6	1.0	95.143	95.006	0.137
4 0 0	3	2	0.8	116.923	116.764	0.159
3 3 1	9	9	0.0	136.514	136.309	0.205
4 2 0	8	7	1.1	144.723	144.500	0.223

Table 5.3.: Diffraction data from PDF file and measured with XRD on pure copper powder. Relative intensities and angular position of intensity maxima.

therefore the reference measurement for a copper sample with randomly distributed grains. Texture index calculations, as described in Chap. 4.3.2, are performed on the basis of this data.

Fig. 5.26 shows an example of the results of the texture analysis of the Cu2 sample performed with the help of EBSD. The grain orientation map in Fig. 5.26a is the basis for the calculation of the MUD–factor (defined in Chap. 4.2.3), see Fig. 5.26c. Large grains clearly dominate the MUD–factor distribution thanks to their large area. Apart from the [1 1 1] direction no ideal or near–ideal main direction is present. The maxima are occupied by higher–order orientations whereas the maximum MUD–factor of 2.43 indicates the presence of a strong texture.

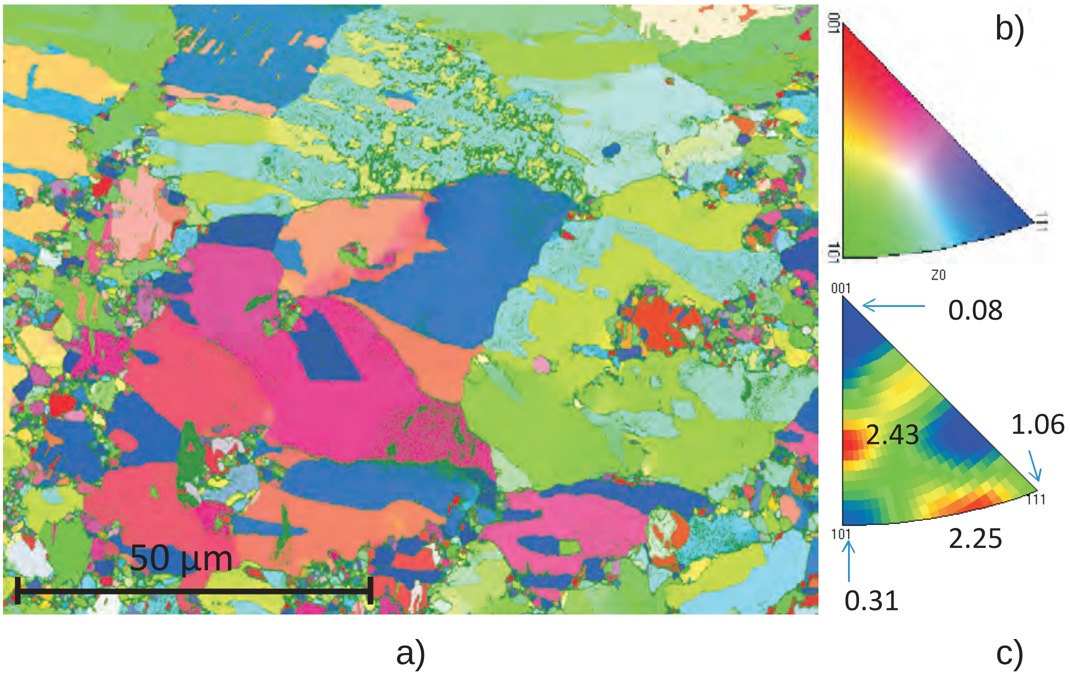

Figure 5.26.: EBSD results of Cu2 sample. a) grain orientation map b) inverse pole figure color–orientation code c) inverse pole figure density distribution (MUD factor)

Tab. 5.4 allows a direct comparison of the values obtained by the two techniques, XRD and EBSD, for each thin film sample showing the T_{hkl} value and the corresponding MUD–factor. As a measure of the degree of texture, the maximum value of both parameters is listed in the last two columns. As expected

Sample	T_{111}	MUD_{111}	T_{200}	MUD_{100}	T_{220}	MUD_{110}	T_{max}	MUD_{max}
SS2	0.62	0.07	5.31	2.23	0.01	0.66	5.31	3.02
Cu2	3.77	1.06	2.18	0.08	0.00	0.31	3.77	2.43
SS3	2.68	0.60	2.59	0.52	0.05	1.99	2.68	1.99
Cu3	4.66	0.18	1.14	2.15	0.01	0.17	4.66	2.48
SS4	1.84	0.48	3.00	1.02	0.14	1.23	3.00	1.32
Cu4	3.41	0.63	2.00	0.80	0.07	0.95	3.41	1.57
SS5	0.49	0.62	2.11	0.72	0.04	1.41	5.11	1.41
Cu5	1.49	0.54	4.15	0.84	0.02	1.69	4.15	1.85
SS6	2.92	0.54	2.18	0.64	0.05	1.66	2.92	1.66
Cu6	1.19	0.43	4.39	1.12	0.02	1.32	4.39	1.45

Table 5.4.: T_{hkl} values and corresponding MUD–factors for each thin film. Additionally maxima values of both as measure of degree of texture.

for a preferentially textured microstructure, a direct correlation between the parameters of the two techniques is not straightforward (see also [123, 124]):

1) The area considered in the XRD is in the order of 10 mm^2, whereas in the EBSD the area covered is about 0.01 mm^2. XRD averages therefore over a 1000 times larger area. EBSD on the other hand may be influenced by local inhomogeneities and insufficient statistics (even with large area scans).

2) As mentioned in Chap. 4.2.3, T_{hkl} only takes into account a limited number of reflections and hence orientations. The MUD-factor considers every orientation and results in a contour plot in the inverse pole figure. Due to the large number of neglected orientations, T_{hkl} is far less representative as compared to the MUD-factor.

A complete data set itemized for each thin film can be found in the Appendix (Fig. A.6 to Fig. A.15).

5.5. Fatigue Data

5.5.1. Thin Films

The fatigue data of the thin films fatigued by LAF are shown in Fig. 5.27, plotting *Ra* roughness as a function of cycle number. Only the best and worst performing thin film are shown for easier illustration. The same evolution was measured for annealed bulk copper in order to do a comparison with results obtained from the thin films. The roughness measurement of the bulk specimen suffered from very inhomogeneously distributed surface damage. Every data point is an average of five measurements. The best performing thin film crosses the threshold of 20 nm (as described in Chap. 4.4.3 and specified for the CLIC AS) at 2.0 x 10^4 cycles whereas the worst performing one crosses the threshold already at 2.0 x 10^3 cycles. The annealed bulk material crossed the threshold already within the first 1000 cycles.

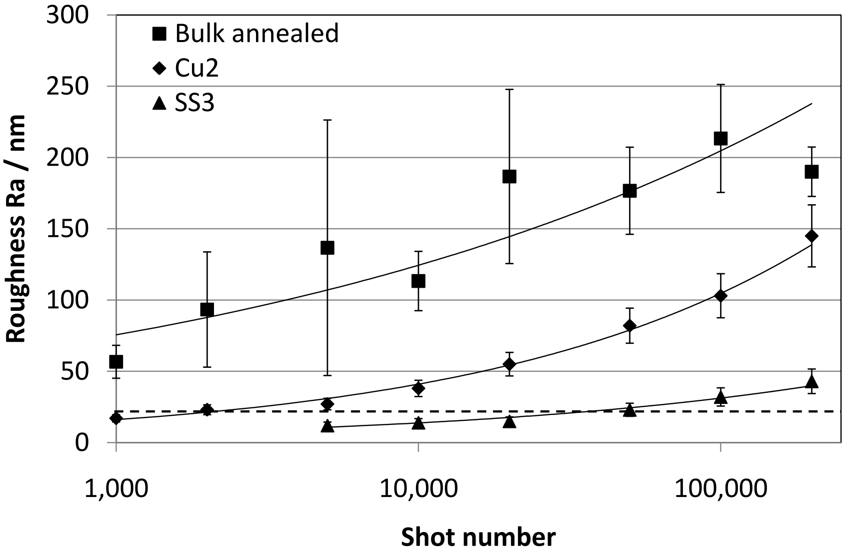

Figure 5.27.: Comparison of roughness evolution on annealed bulk copper with best (SS3) and worst (Cu2) performing copper thin film after LAF with 0.3 J/cm^2 ($\Rightarrow \Delta$T = 180 K and ϵ_{eq} = 5.1 x 10^{-3}).

5.5.2. Bulk Material

An excerpt of the fatigue data obtained with the help of the different fatigue techniques is presented as S–N plot in Fig. 5.28. Since the aim of this test campaign was to compare the different fatigue test benches and since most of the data in [117] and other literature are based on cold worked copper, the main part of the tests were performed on the H02 temper. The single data point of the LAF on H02 copper (solid black circle), where fatigue life is defined with the help of the roughness criterion threshold $Ra = 20$ nm, is well above the data obtained from CVF (at 6.0 x 10^4 cycles: 1.9 x 10^{-3} for LAF compared to 1.5 x 10^{-3} for CVF). As expected the brazing annealed temper is situated well below the H02 temper in CVF. The data points of the thin films fatigued by LAF show superior fatigue behaviour when compared to H02 temper fatigued by LAF and CVF. The H02 temper exhibits in USS an evolution well above the expected literature value of 5.0 x 10^{-4} (⇒ 90 MPa) at 1.0 x 10^8 cycles.

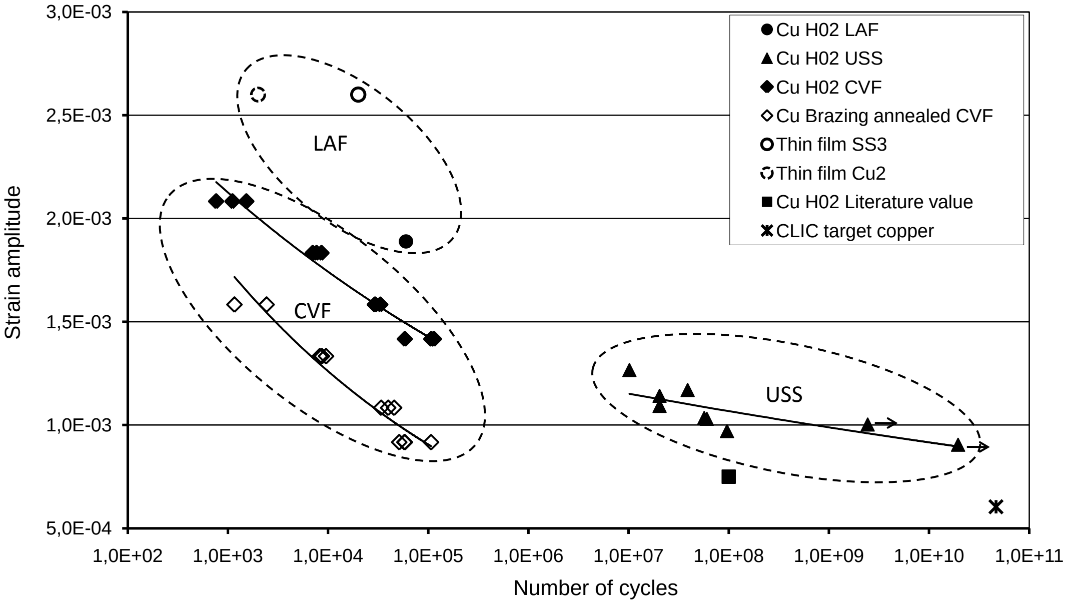

Figure 5.28.: S–N plot of fatigue data obtained with LAF, USS and CVF on H02 temper (solid symbols) and on brazing annealed copper (hollow symbols). For comparison, the literature value for H02 copper [34] and the CLIC target [117] is plotted. USS data partly from [117].

6. Discussion

The results of the four different fatigue experiments are compared and conclusions drawn about the commonality of phenomena. Fatigue–induced hardening, microstructure and orientation–induced effects are discussed on the basis of the results of the current study and compared with findings reported in the literature.

6.1. Comparison of Different Fatigue Test Procedures

The four fatigue devices used in this study (see Chap. 4.4) induced cyclic loading by four different methods. Their different effects on the materials is studied and commonality of phenomena are discussed as well as the consistency of results obtained by the fatigue test benches.

6.1.1. Load Ratio Dependency

Most of the results obtained through the mechanical devices, CVF and USS, involve a load ratio of $R = -1$, which means a fully reversed tension–compression load [41]. In the thermal cycling methods, LAF and RFF, the load ratio is assumed to be $R = 0$, representing a fully compressive loading with nil minimum stress was assumed (”zero–tension fatigue“ [41]).

In LCF the load ratio influences lifetime significantly. Assuming on the one hand cycling with a load ratio of $R = -1$, where the stress amplitude $\Delta\sigma = \sigma_{max}$ - σ_{min}, where σ_{max} is just under the elastic limit, the material will (ideally) exhibit fully elastic behaviour. On the other hand, when cycling with a load ratio of $R = 0$ and the same $\Delta\sigma$, the maximum stress σ_{max} may exceed the elastic limit, taking the material into its plastic regime, where fatigue mechanisms are known to be different [41]. This non–symmetric loading can become even more significant because the yield strengths in compression and tension are not necessarily the same or because of the known Bauschinger effect (see Chap. 2.3.3).

In UHCF the fatigue lifetime tends to become independent of the load ratio when the load amplitude is very low (e.g. $\epsilon = 5 \text{ x } 10^{-4}$. Results obtained by Heikkinen [117] from USS tests with pre–compressed copper and copper alloy samples ($R = 0 \Rightarrow$ fully compressive loading) showed no difference in lifetime compared to samples cycled in tension and compression (R = -1). However, from their ultrasonic–frequency tests on aluminum alloys Stanzel-Tschegg et al. [125, 61, 126] reported that fatigue crack growth rates decrease with increasing R. The observations of Heikkinen [117] and Stanzel-Tschegg et al. are not necessarily in contradiction, however. It is known that at very low cyclic loads in strain–controlled fatigue testing (UHCF) the material spends more than 90% of its fatigue life for the crack initating. The dependency of fatigue crack growth on R observed by Stanzel-Tschegg et al. could therefore play only a minor role under UHCF loading conditions, simply because of the short time spent for the crack propagation.

To sum up the discussion about the influence of the load ratio in the four different applied fatigue tests, the following two conclusions can be drawn:

1) Load ratio does play a role in LCF and HCF. The results obtained with the help of CVF should therefore be treated with caution when comparing with results obtained with LCF. Additional CVF testing with $R = 0$ must be performed in order to quantify the influence of R on fatigue life time for this specific test.

2) Since the fatigue devices operate in different fatigue regimes (LAF, CVF and RFF in LCF and HCF, but USS in UHCF) it should be mentioned which R has been applied in order to ensure the consistency of results. Notwithstanding the above, R has limited influence under UHCF loading conditions, which are representative for the intended use in the CLIC–AS.

6.1.2. Type of Loading

In the mechanical loading methods, CVF and USS, the material is loaded through an external force. The setup is ideally isothermal, which means throughout the whole testing time the sample is kept at a constant temperature [117]. This means that whether the material is under maximal load or unloaded the temperature is the same.

Cycling of the material in the LAF and in RFF is performed by applying cyclically pulsed heat to a fraction of the material surface. The heated part of the material tries to expand but is restricted by the surrounding material. The temperature of the material under maximum stress is therefore higher than in the unloaded state, where the temperature equals the ambient temperature. Although pulses in the thermal cycling methods, LAF and RFF, are very short (60 ns for LAF [91] and 1.5 μs for RFF [127, 128]), the microstructural impact of maximum stress combined with elevated temperatures have to be discussed. Four microstructural processes are considered:

1) self–diffusion as a measure of the migration length of vacancies to possible stress releasing sites.

2) dislocation climb (non–conservative dislocation motion) as a possibility for enhancing dislocation annihilation.

3) enhanced dislocation slip (conservative dislocation motion).

4) release of dislocations in the Frank-Read source and its temperature dependency.

The influence of self–diffusion can be assessed by a simple calculation of the *diffusion coefficient* D using Fick's law at RT and the highest achieved temperatures in the different tests

$$D = D_0 exp(-Q/R_g T) \tag{6.1}$$

where D_0 is a *temperature independent constant*, Q is the *activation energy*, R_g is the *ideal gas constant* and T is the *absolute temperature* of the material. For the parameters of copper (Q = 47100 cal/mol and D_0 = 0.2 cm^2/s [129, 130]; values extrapolated to lower temperatures), at the highest temperature achieved in the fatigue tests, 325°C (LAF at 0.5 J/cm^2), the diffusion coefficient is D_{325} = 1.4 x 10^{-4} nm^2/s. Assuming a laser pulse with a length of 60 ns the *effective diffusion area* A_{deff} at the maximum temperature $A_{deff-325}$ = 8.5 x 10^{-12} nm^2 (for RFF: for max ΔT = 110 K and a pulse length of 1.5 μs it is $A_{deff-135}$ = 2.4 x 10^{-17} nm^2). Since all values even at the highest achieved temperatures correspond to diffusion distances far below the inter–

atomic distance, self–diffusion during one pulse is not significant in either of the fatigue methods.

The mechanism of dislocation climb is directly linked to the self–diffusion mechanism: dislocation climb is driven by diffusion of atoms and vacancies [46]. It is therefore not relevant for the assessment of differences in kinds of cycling.

Enhanced dislocation slip, and hence movability, is related to the velocity of a dislocation in a crystal. By describing the dislocation motion analytically as in [46], it can be shown that the velocity is proportional to $(1/\mathrm{G})^{N_{gl}}$, where G is the *shear modulus* and N_{gl} is the *stress exponent for slip*. Since G is temperature dependent and falls with rising temperature [131], the velocity, and hence mobility of dislocations, rises with temperature.

The critical shear stress of a Frank-Read source, above which a dislocation is released, can be described analytically [46]. In the critical position, the force due to the applied stress is balanced by the line tension of the expanding loop of dislocation. The critical force is found to be proportional to G and therefore with increasing temperature the critical force decreases and Frank-Read sources tend to release more dislocations.

To sum up the possible differences of the mentioned cycling methods, it can be said that diffusion driven processes (diffusion of vacancies and dislocation climb) are not relevant, whereas the influence of the shear modulus dependent processes (dislocation velocity and critical shear stress of Frank-Read sources) cannot be assessed trivially.

6.1.3. Stress States

The mechanical testing methods CVF and USS submit the samples to a well defined uniaxial loading, as shown for the USS in Chap. 4.4.2. The loading axis is longitudinal to the sample axis and the stress is homogeneous on the cross section of the sample for the CVF case, whereas in the USS samples it is a function of the radius, as seen in Fig. 4.13.

The thermal loading methods result in a very different stress state. As the heating pulses of the concerned surface areas are very short (60 ns for LAF [91] and 1.5 μs for RFF [127, 128]) the penetration depth of the heat is rather small. At the time step of the highest surface temperature load the material at 10 μm depth for the LAF and at 45 μm for the RFF is still at room temperature. Compared to the heated layer thickness the lateral extension of the heated region is rather big. It is shown in Chap. 4.4.3 by simulation that the resulting strain state is perfectly biaxial within the laser spot, apart from the border effect arising from the transient region.

It is reported that when a biaxial state is used for cyclic loading, the fatigue lifetime shortens for all equivalent criteria presented in [76, 77]. Several simulation models to predict fatigue life in multi–axial fatigue have been introduced [132, 133, 134], but a conclusive microstructural explanation remains elusive.

One reason for differences in fatigue life for uniaxially and biaxially loaded samples arises from the different Schmid factor configuration present in the crystal (see Chap. 2.3.2). Schmid factor calculations performed for the biaxial and uniaxial loading case (Appendix Fig. A.1 - A.2) show that not only the maximum Schmid factor but also the number of active slip systems differs in the two cases. For the [1 1 1] out–of–plane orientation and the similar in–plane–orientation, the biaxial case shows $\mathrm{SF}_{max-bi} = 0.27$, whereas in uniaxial loading $\mathrm{SF}_{max-uni} = 0.41$. The number of active slip systems in biaxial loading is 6 whereas in uniaxial there are only 4 slip systems active. A significant difference in strain and stress distribution on the slip systems is therefore calculated (see Appendix Fig. A.1 - A.2). Additionally, calculations with variable in–plane orientations (Appendix Fig. A.2 - A.4) showed that the SF distribution in the biaxial state is independent of in–plane orientation, whereas in the uniaxial loading case the SF distribution strongly depends on in–plane orientation. The evidence of this in–plane orientation dependence is observed in the samples fatigued by USS (see Fig. 5.13), where grains with similar out–of–plane orientation but different in–plane orientation show different surface roughening due to cycling. It must be pointed out that simulations performed with FEM, taking into account the elastic anisotropy of the copper lattice [135, 136], showed that the real SF distribution differs slightly from the distribution in the classical approach used here. SF's differ in the order of of 15% which results also in some modification of the slip activation order. Due to computational limitations this effect cannot be taken into account here and the phenomenon will be explained on the basis of anisotropy, neglecting SF–FEM simulations. The influence of SF distribution on the fatigue behaviour of surface grains will be discussed in more detail in Chap. 6.2.1.

In summary it can be said that from the microstructural point of view, the difference in load case is significant, although no conclusive model based on dislocation interaction or multiple slip has been proposed. Empirical models and experiments [76, 77] predict fatigue life under multi–axial loading to be significantly shorter. For the current study, a suitable criterion was therefore needed in order to compare results obtained with mechanical fatigue (CVF and USS) with those obtained with thermal cycling methods (LAF and RFF) in a quantitative way.

6.1.4. Cycling Frequencies: Low versus High

Cycling frequency is one of the major issues for fatigue testing with high cycle numbers. CVF and the thermal cycling methods LAF and RFF used in this study have a low cycling frequency. Of these three, LAF has the highest frequency at 200 Hz (as described in Chap. 4.4). In contrast, USS has an extremely high frequency of 24 kHz. The comparability of the results obtained by application of such a wide range of cycling frequencies must therefore be discussed here.

The devices used in the present study do have a common non–achievable cycle number region from roughly 10^6 to 10^7 cycles (compare Tab. 4.4 and Fig. 5.28) which makes it experimentally very difficult to cross check fatigue results in the HCF and the UHCF regime obtained with different devices. The overlap between HCF and UHCF is often studied with the help of rotation bending methods and devices similar to the USS device used in the present study. Thus Papakyriacou et al. [137] compare results of 100 Hz rotation bending tests with results obtained at 20 kHz with the help of an ultrasound resonator. For samples made of Nb they report that no influence of the loading frequency was observed, whereas samples made of Ta showed significantly longer lifetime when cycle frequency was high. During those tests the temperature of the sample was kept a few degrees above RT (see also [63]). Park et al. [138] observed the frequency effect in thermal fatigue of copper interconnects by cycling 300 nm thin sputtered copper lines with alternating currents at frequencies of 200 Hz and 20 kHz. They report significantly faster damage development when the frequency was increased to 20 kHz. Generally it is believed that increasing the loading frequency from 60 Hz to 20 kHz does not affect fatigue life in bulk FCC metals such as Cu, but that it does prolong the fatigue life of BCC metals [138, 137]. Very often the reason for the frequency dependence in BCC metals is believed to be the strong strain rate dependence of deformation, which originates from the high lattice friction and the necessity of thermally activated glide of screw dislocations [138].

For the present study, the discussion concerning the effect of the different load frequencies can used to draw an important conclusion: as long as the copper samples cycled at high frequencies with the USS device are suitably cooled to near RT, the influence of the loading frequency on the fatigue life can be neglected.

6.1.5. Surface Degradation as a Function of Grain Orientation and Effects of Grain Boundaries

It was shown in the previous discussions that the loading conditions in all fatigue test benches used in the present study and in the AS of CLIC are quite different. Therefore an approach based on observable phenomena in order to assess the comparability of results and the commonality of phenomena should be presented here. Two particularly observed phenomena will be used as comparison criterion for the different techniques:

1) the different degree of surface roughness developing on grains of different crystallographic orientation.

2) the correlation between the width of the modification zone of surface features in the vicinity of certain GB.

On samples fatigued by LAF a clear correlation between the developing degree of surface roughness and the crystallographic orientation was found: Surface roughness on [1 0 0] grains is less than on [1 1 1] grains, and both are less than on [1 1 0] grains, as shown in Fig. 5.10 and Fig. 5.11. The reasons for this difference in fatigue behaviour will be discussed in Chap. 6.2.1. To some extend the same correlation was found on samples fatigued by RFF, as shown in Fig. 5.12. Grains of [1 0 0] direction stayed mostly smooth, showing therefore much less surfaces roughening as compared to grains of the [1 1 1] orientation.

Grains of the direction [1 1 0] were not present within the observed areas. The situation for samples fatigued by USS is much more complex. On the one hand, as with the LAF and RFF fatigue samples, grains of [1 0 0] out–of–plane orientation were found to stay smooth. On the other hand, [1 1 1] grains were found to exhibit either severe roughening, moderate roughening or no roughening at all, depending on their in–plane orientation, as shown in Fig. 5.13 and Tab. 5.1. The consistency of phenomena between LAF and RFF was shown for two of the three main orientation candidates. The additional degree of freedom of crystallographic orientation in USS makes the correlation of the roughness to grain orientation more demanding when compared to LAF and RFF. The second phenomenon concerns the modification of developing surface features in the vicinity of GB, here called the GB vicinity effect. A correlation between the width of the modification zone and the thickness of the heated layer was found in samples fatigued with LAF. The width of the modification zone between a [1 0 0] and a [1 1 1] grain, shown in Fig. 5.14, was found to extend approx. 7 μm – 10 μm to either side of the GB, corresponding to the thickness of the heated layer for the experiment. For the LAF technique this ratio of width of modification zone to heated layer thickness = 1 was confirmed for a different type of GB ([1 0 0] – [1 1 0]), shown in Fig. 5.15b. Nevertheless, the orientation of the GB with respect to the developing surface features has an influence on the width of the modification zone, as shown in Fig. 5.15a where no modification zone is visible in either of both adjacent grains. For samples fatigued with RFF a similar GB vicinity effect has been observed, as shown in Fig. 5.16. The width of the modification zone was found to be between 17 μm and 30 μm, which corresponds to the heated layer thickness for the experiment. A GB vicinity effect in samples cycled by USS was not discovered. The origin of the GB vicinity effect and the differences for the USS technique will be discussed in Chap. 6.2.2

The results of the phenomenological comparison approach can be summarised as follows:

1) The same correlation between the developing degree of surface roughness and the grain orientation was found for both thermal cycling methods for two of the orientation candidates([1 0 0] and [1 1 1]). More statistics would be needed in order to establish the correlation for the third orientation candidate. On the

other hand, the same correlation cannot be observed conclusively on the samples cycled with the USS device.

2) The ratio between the width of the surface feature modification zone and the heated layer thickness was found in both thermal cycling methods to be approx. equal to 1, underlining the similarity of phenomenon observed in the two fatigue techniques. The GB vicinity effect was not observed on samples cycled with the USS technique.

6.2. Fatigue Effects

Here the mechanisms ongoing in polycrystalline copper of different temper states during cycling will be discussed in more detail on the basis of results obtained within the current study. Explanations will be given concerning different effects on fatigue behaviour such as grain orientation and GB vicinity, followed by considerations about the relation between hardness and fatigue.

6.2.1. Fatigue Induced Roughness and Crystallographic Orientation

Observations of the surface topography and roughness measurements following different fatigue tests, show that the increase of surface roughness in fatigued high purity copper depends strongly on individual grain orientation, as shown in Fig. 5.11. The observed tendencies are similar, independent of the temper state or the fatigue testing method applied. Grains oriented in the [1 1 1] direction show much greater increases as those oriented in [1 0 0] whereas [1 1 0] grains show the biggest increases of all. These observations are consistent with the findings of researchers [43, 75, 139, 140] who have studied mainly thin films and single crystals. This difference in surface roughening due to fatigue has several causes:

(1) Elastic anisotropy approach: the [1 1 0] grains experience the highest shear stress, followed by those in [1 1 1] and then those in [1 0 0] direction. In both thermal cycling methods the biaxial load is thermal strain due to thermal expansion, which produces thermal stress. The isotropy of the thermal expansion coefficient [38] causes uniform strain in all grains, while the Young's modulus

and shear modulus is anisotropic. Due to this anisotropy, different levels of stress arise during the load cycle in grains with different orientation [139]. The order of this inhomogeneity was calculated by Wikstroem et al. [140] and Baker et al. [139], which were focusing on [1 1 1] and [1 0 0] grains in thin copper films. They found that the ratio between the evolving in–plane stresses in [1 1 1] and [1 0 0] oriented grains can become as high as $\sigma_{111}/\sigma_{100} = 2.3$, equal to the ratio of the corresponding moduli. Moenig [141] confirmed this for copper thin films by calculating the in–plane stress arising from an equi–biaxial in–plane strain as a function of the orientation of the crystal. Like Wikstroem et al. he calculated a ratio $\sigma_{111}/\sigma_{100} = 2.26$. These two orientations are associated with the maximum and the minimum stress values, found in the orientation triangle. Moenig [141] calculated the resolved shear stress under the same in–plane strain and found a ratio of $\tau_{111}/\tau_{100} = 1.51$. A calculation for the whole triangle allowed orientations to be identified where shear stresses even higher than τ_{111} develop. As an example, [1 1 0] grains undergo a higher shear stress due to a ratio $\tau_{110}/\tau_{100} = 1.60$. Therefore, the [1 1 0] grains are submitted during cycling to the highest maximum shear stresses followed by the [1 1 1] grains and the [1 0 0] grains. This means that the order of effective shear stress of the three main crystallographic orientations ($\tau_{100} \leq \tau_{111} \leq \tau_{110}$) is the same as the trend in the amount of surface roughening observed here experimentally, as seen in Fig. 5.10 and Fig. 5.11.

(2) Schmid factor distribution approach: in [1 0 0] grains there are 8 equally active slip systems. Global strain is distributed equally on the 8 systems. In [1 1 1] grains only 6 systems are active and in the [1 1 0] grains only 4 (see Appendix Fig. A.1). The fraction of the global strain applied on a single slip system is therefore the lowest in the [1 0 0] grains. A lower fraction of strain implies lower local deformation hence dislocation motion. Additionally, the Schmid factor values of the orientations are different. Fig. 6.1 illustrates schematically the influence of different Schmid factors on local strain. By imposing an elongation of ΔL on a sample in Fig. 6.1a, different shear strains are induced due to different Schmid factors. In the case in Fig. 6.1b a low Schmid factor forces the slip system to compensate for the imposed sample elongation with more local shear strain. Therefore high dislocation motion, and hence micro plasticity, is required. A high Schmid factor in the case shown in Fig. 6.1c allows the sample

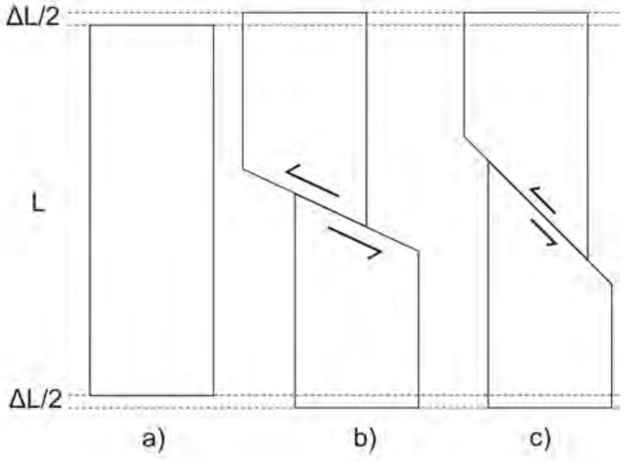

Figure 6.1.: Schematic of influence of Schmid factor on local shear strain in uniaxial single crystal under tensile strain oriented for single slip: (a) An elongation ΔL is imposed on a sample of the length L. When slip system has low Schmid factor (b) local high shear strain is needed to accommodate ΔL, whereas in (c) a higher Schmid factor results in lower local strain.

elongation to be compensated with comparatively smaller local shear strain. For this reason, grains with Schmid factors as low as 0.27, as found in the slip systems in the [1 1 1] grains, show high microplasticity. On the other hand, grains with Schmid factors as high as 0.41, found in the orientations [1 0 0] and [1 1 0], show lower microplasticity. Together with the higher fraction of total amount of strain on each individual slip system, due to the lower number of active systems in the [1 1 1] grains, and the higher micro–plasticity, due to lower Schmid factor, in the those grains result in a higher surface roughness for those, compared to the [1 0 0] grains. Although the [1 1 0] grains feature Schmid factors as high as those found in the [1 0 0] grains, the small number of active slip systems (only half those in [1 0 0])results in the highest local strain, and therefore the highest surface roughness, of the observed crystallographic orientations.

(3) Dislocation substructure approach: depending on the crystallographic orientation, hence the orientation of the slip system with respect to the loading plane, different dislocation substructures can be formed. Zhang et al. [43] and Wang et al. [50] have given indications on the dislocation substructure that

will develop in the copper grains/crystals during cycling, depending on their position in the standard orientation triangle. Grains of the [1 1 1] direction will develop dislocation walls and ladder–like cell structures, those oriented in [1 0 0] mainly show labyrinth structures occur, while those in [1 1 0] direction show PSB ladders. The orientations, which create a three–dimensional arrangement of dislocations (e.g. cellular or labyrinth structure found in [1 0 0] grains), inhibit surface upsets and therefore preserve smooth surfaces [45].

It is possible to explain the observed phenomenon of orientation dependent surface roughening during cycling on the basis of the three approaches presented here. Further microstructural observations (e.g. TEM) need to be performed in order to assess which one of these three complementary approaches is predominant.

6.2.2. Grain Size and the Effect of Grain Boundaries

Grain boundaries represent special regions, where two lattices of different orientation meet. The crystal is locally heavily disturbed. The grains are submitted to different stress levels during cycling, as discussed above. Therefore adaptation has to take place at the GB. Fig. 5.14 shows a transition region straddling the GB. On both sides the surface near the GB is changed. Since these observed large–angle boundaries are obstacles for dislocation motion, SB and PSB [43, 50], dislocations pile up in the vicinity of the grain boundary [43, 50]. Features observed in the modification zone of the [1 0 0] grain, which elsewhere appears smooth, are evidence for this accumulation. A model for accommodation bands in the GB vicinity due to stress accommodation in copper thin films was developed by Baker et al. [139]. A schematic of this model is presented in Fig. 6.2. The authors claime that in a GB between a [1 1 1] and a [1 0 0] grain, stress continuity requires $\sigma_{111}=\sigma_{100}$. Furthermore, the authors distinguish two extreme cases: in one case a) large grains (>> film thickness) cause constant strain (*isostrain*) while in the other b) small grains (<< film thickness) cause constant stress (*isostress*) around the grain boundary. They assume that stress accommodation takes place within a region of having a width corresponding to the thickness of the considered film, on each side of the boundary. Therefore when grains are small (case b), this accommodation zone covers most of the

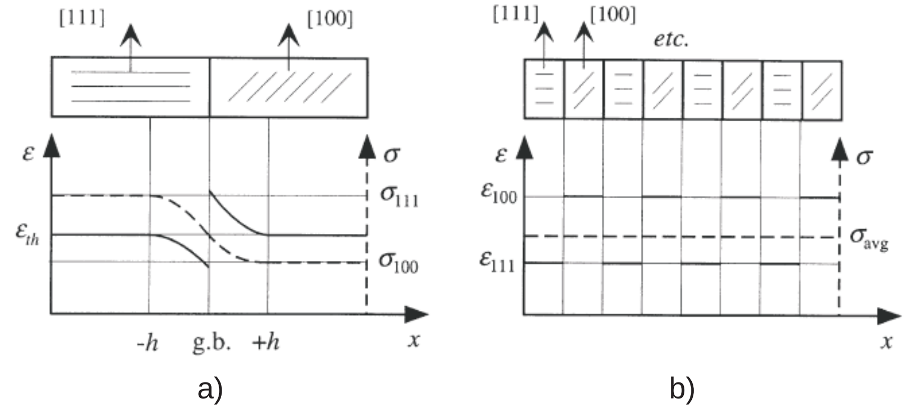

Figure 6.2.: Schematic showing the form of strain and stress distributions during elastic deformation in thin film after Baker et al. [139]. Grains oriented [1 1 1] and [1 0 0] out of surface accommodate stress within one film thickness to either side of the GB: case a) large grain size results in same average strain in both grains (isostrain case); case b) small grain size results in same stress in adjacent grains (isostress case)

space, and the stress distribution is uniform. However, three points in connection with the mentioned study should be born in mind:

(1) The time–temperature profile provided by the two thermal cycling methods used in this study and described in Chap. 4.4 results in a very high temperature gradient normal to the surface [91, 121]. The high–intensity energy deposition heats the surface layer to the maximum temperature in a very short period of time (LAF 60 ns, RFF 1.5 μs). Although the thermal conductivity of copper at room temperature is very high (401 W/m·K [34]), the heated volume is very small (for LAF 10 μm in depth and for RFF 30 μm; see Chap. 4.4) due to the very short heating time. The current test situation may thus be conceived in terms of a film several μm thick, with constrained lateral expansion due to a rigid substrate, subjected to thermal cycles. Assuming this similarity, it is important to point out that in LAF, as in RFF, the thickness of the heated layer is similar to the width of the accommodation band observed in Fig. 5.14 and Fig. 5.16 respectively. This result is in good agreement with the model developed by Baker et al. [139] where this correlation is predicted for thin films.

(2) The sample in half–hard temper cycled with RFF (shown in Fig. 5.16) has grains of equivalent diameter of a few tens of microns. Surface features are visible not only in the [1 1 1] grains but also in the [1 0 0] grains. Here accommodation appears again at the grain boundaries, but also extends within the grain. Completely smooth areas within [1 0 0] grains are rarely observed. They are mainly found in the center of large grains at sufficiently large distances from the grain boundaries. The same trend is observed on half–hard samples cycled with LAF. Conversely this means that, in sufficiently small grains, the accommodation area covers the entire grain. With decreasing grain size, all grains suffer from accommodation throughout, regardless of their crystallographic orientation, at the same stress level. This case would correspond to the predictions by the model of Baker et al. [139] about the so–called *isostress* state (case (b) where the common stress level lies in between the stress of the [1 0 0] grains and that of the [1 1 1] grains).

3) The GB between a [1 0 0] and a [1 1 0] grain in Fig. 5.15 shows ambivalent behaviour. When surface features in the [1 1 0] grain, which are aligned to a (1 1 0)–type axis as identified by EBSD, are parallel to the GB (a), no accommodation zone is observed, whereas in (b), where the features are nearly perpendicular to the GB, an accommodation zone with the width of one heated layer thickness on each side is visible. The results predicted by the Baker model [139] can be observed only partly in this GB configuration. Since in Fig. 5.15 exactly the same grains are involved and a different behaviour is observed, the orientation of the GB with respect to the lattice orientations of the adjacent grains plays a role. This gives rise to the question of the dependency of the GB vicinity effect not only on the GB–type but also on the GB-misorientation.

However, accommodation zones in the GB vicinity were not observed on samples cycled using USS. This may have several reasons:

1) In the uniaxial stress state not only the type and the orientation of the GB with respect to the lattice of the adjacent grains are important but also the orientation of the GB with respect to the loading axis, the USS therefore offers an additional degree of freedom for GB description. Additionally, since some [1 1 1] grains show partly damage (see Fig. 5.13), accommodation does not necessarily have to occur at all GB surrounding a [1 1 1] grain. Therefore many more grains and GBs have to be observed in order to ensure a quantitative

statement on a solid statistical basis.

2) As simulated and shown in Fig. 4.13, the strain region in the USS sample reaches deep into the interior. Since the thickness of the corresponding “heated” layer in the USS method, here called “stressed” layer, is in the order of several mm, it is questionable if the model of Baker et al. [139], developed for copper thin films of certain texture, is still applicable. The assumption of stress accommodation within one layer thickness in depth and to each side of the GB may not be valid anymore and hence a distinction between the earlier mentioned *isostress* and *isostrain* state is not possible.

6.2.3. Fatigue Induced Hardening

Two of the main micro structural processes occurring during cyclic mechanical loading are the creation and the rearrangement of dislocations, as described in Chap. 2.3. Since these processes are classically responsible for hardening of the material [41] and since it is believed that theses processes also occur during thermal cycling, a macroscopic hardness increase should be observable during cycling.

The microhardness results obtained at different cycle numbers of OFE copper samples cycled with the help of LAF (Fig. 5.21) show a continuous increase in hardness with increasing cycle numbers. Moreover, hardness observations on a copper single crystal submitted to RFF shows an increase in hardness proportional to the maximum thermal load, once a temperature threshold is exceeded (Fig. 5.18). It can therefore be said that the process of dislocation creation due to thermal cycling, within the experimental frame of this study, is indirectly confirmed. Since the H02 temper did not show hardening after RFF cycling (Fig. 5.18) it can be said that, for the given testing parameters, a previously work–hardened material responds differently to the cycling, compared to a soft state, and does not show additional hardening through cycling (for sample material description see Chap. 4.1.1). Regarding the arrangement of dislocations due to fatigue, no statements can be made without additional microstructural observations with the help of TEM or SEM with ECC.

Furthermore, there is experimental evidence that different crystallographic orientation harden differently during cycling. In Fig. 5.20 it is shown that hardness increase of differently oriented grains in LAF fatigued samples follows the same order as the roughness increase of corresponding orientations after cycling in Fig. 5.11. Grains in [1 1 1] direction show a higher amount of hardening as compared to [1 0 0] grains, whereas the [1 1 0] grains show the highest hardening. This result could also be explained by the first two of the three approaches to explain roughening discussed above:

1) Elastic anisotropy approach: highest shear stress due to elastic anisotropy in [1 1 0] grains produces the most dislocations, resulting in the highest hardening.

2) Schmid factor distribution approach: highest local strain on individual slip systems in [1 1 0] grains due to most disadvantageous Schmid factor configuration produces most dislocations, resulting therefore in the highest hardening.

The third explanation, the dislocation substructure approach, dealing with cyclically more and less stable dislocation substructures developing in the material, cannot be assigned directly since no statements can be made about the dimensions of any developing dislocation substructures or dislocation density distribution. Further microstructural analysis is needed here.

7. Summary and Conclusions

In the present study four fatigue test benches were use and compared in order to investigate the fatigue behaviour of oxygen–free electronic (OFE) copper as a candidate material for the accelerating structures (AS) of the compact linear collider (CLIC). In operation the material will undergo cyclic temperature change in the order of $\Delta T = 56$ K, from about 40° C to about 100° C. This temperature change results in a cyclic biaxial strain in the surface in the order of $\Delta\epsilon_{biax} = 9.2 \text{ x } 10^{-4}$ at a macro equivalent stress of 110 MPa. From the results obtained in the present study the following conclusions can be drawn:

(1) Structural fatigue failure is not a concern for an AS made of copper or a copper–based alloy.

(2) However, surface roughening due to thermal cycling will eventually occur in the AS. Roughness values have been measured after different cycle numbers. After a certain incubation time, there is a significant increase in roughness. This incubation period is shorter than the designed service life of CLIC. Therefore, the effect of surface roughening on the physical performance of the AS needs to be closely monitored.

(3) Characterisation and quantification of cyclic roughening and hardening phenomena on tested samples revealed a strong dependence on grain orientations. With the help of EBSD observations it was found that grains oriented in [1 0 0] direction show significantly lower roughness and hardness increase than grains oriented in [1 1 0]. The [1 1 1] orientations show intermediate values.

(4) A detailed analysis of the slip systems of the different orientations made it possible to understand the origin of the roughening phenomena and their dependence on crystallographic orientation. This dependence arises from the different number of active slip systems.

Analysis of the results obtained by different fatigue test techniques indicates the presence of the same elementary processes. The two mechanical loading methods, conventional fatigue (CVF) and ultrasonic swinger (USS), have experimental advantages in terms of standardisation and in terms of the capability of addressing high cycle numbers. Unfortunately, the results obtained cannot be directly related to thermal fatigue data.

It is not clear whether surface roughening arising from thermal cycling is the limiting factor for operating AS. The present study has shed light on the origin of fatigue–induced surface roughening and helped identify three micro–structural elements which are important in this respect:

– The [1 0 0] crystallographic orientation of surface grains shows the smallest amount of surface roughening and sub–surface hardening.

– Copper materials with high initial hardness show no further cyclic strengthening, while significant cyclic hardening accompanied cycling of soft material states.

– Grain boundaries need to be considered in fine structures (grain sizes as fine as 1 μm – 5 μm). High local stresses arising from the effect of anisotropy of moduli are therefore averaged out.

Since electrical conductivity is important for the CLIC AS application (see Chap. 2.1) the choice of material is restricted to copper–based materials. Following the three aforementioned favorable characteristics, two possible candidates for the application in CLIC–AS are:

1) A strongly textured and fine–grained OFE copper, e.g. equal–angular–channel–pressed (ECAP) OFE copper

2) A strongly [1 0 0] orientation textured pure copper thin film.

Either options could provide the fatigue performance needed to meet the high demands of the CLIC-AS, and deserve closer consideration in the context of the AS machining strategy.

Bibliography

[1] "ASTM B601 - 09 standard classification for temper designations for copper and copper alloys wrought and cast," 2009.

[2] "http://www.cern.ch."

[3] "http://clic-study.web.cern.ch/clic-study/."

[4] "http://lhc.web.cern.ch/lhc/."

[5] H. Braun, R. Corsini, J. P. Delahaye, A. de Roeck, S. Dbert, A. Ferrari, G. Geschonke, A. Grudiev, C. Hauviller, B. Jeanneret, E. Jensen, T. Lefvre, Y. Papaphilippou, G. Riddone, L. Rinolfi, W. D. Schlatter, H. Schmickler, D. Schulte, I. Syratchev, M. Taborelli, F. Tecker, R. Toms, S. Weisz, and W. Wuensch, "CLIC 2008 parameters," tech. rep., CERN CLIC-Note-764, Oct 2008.

[6] G. Guignard, "A 3 TeV e+e- linear collider based on CLIC technology," tech. rep., CERN, 2000.

[7] G. Arnau-Izquierdo, S. Calatroni, S. Heikkinen, T. Ramsvik, S. Sgobba, M. Taborelli, and W. Wuensch, "Material selection and characterization for high gradient RF applications," in *22th Particle Accelerator Conference, 25 - 29 June 2007, Albuquerque, NM, USA,*, pp. 2197–2199, 2007.

[8] A. Grudiev, H. Braun, D. Schulte, and W. Wuensch, "Optimum frequency and gradient for the CLIC main linac accelerating structure," CLIC-Note 771, CERN, 2009.

[9] K. J. Miller and W. J. O'Donnell, "The fatigue limit and its elimination," *Fatigue & fracture of engineering materials & structures*, vol. 22, pp. 545–557, July 1999.

[10] Mayer, Lipowsky, Papakyriacou, Rsch, Stich, and Stanzl-Tschegg, "Application of ultrasound for fatigue testing of lightweight alloys," *Fatigue & fracture of engineering materials & structures*, vol. 22, pp. 591–599, July 1999.

[11] H. Mughrabi, "On the life–controlling microstructural fatigue mechanisms in ductile metals and alloys in the giga cycle regime," *Fatigue & Fracture of Engineering Materials & Structures*, vol. 22, pp. 633–641, July 1999.

[12] G. Eggeler, E. Hornbogen, A. Yawny, A. Heckmann, and M. Wagner, "Structural and functional fatigue of NiTi shape memory alloys," *Materials Science and Engineering A*, vol. 378, pp. 24–33, 2004.

[13] J. D. Jackson, *Classical Electrodynamics*. Wiley, 1998.

[14] A. Sessler and E. Wilson, *Engines of Discovery: A Century of Particle Accelerators*. World Scientific Publishing Company, 2007.

[15] A. DeRoeck, J. Ellis, C. Grojean, S. Heinemeyer, K. Jakobs, G. Weiglein, and J. Wellsa, "From the LHC to future colliders," tech. rep., CERN, 2009.

[16] "http://atlas.ch/."

[17] "http://cms.web.cern.ch/cms/."

[18] R. Tomas, "CLIC overview," in *EuCARD-CON-2009-028*, European Coordination for Accelerator Research and Development, 2009.

[19] J. Osborne and A. Kosmicki, "CLIC-tunnel cross section." (unpublished note).

[20] "http://tesla-new.desy.de/."

[21] "http://www.linearcollider.org/."

[22] B. Crowell, *Vibrations and Waves*. www.lightandmatter.com, 2009. ISBN 0-9704670-3-6.

[23] A. Anders, *Cathodic Arcs: From Fractal Spots to Energetic Condensation.* Springer Series on Atomic, Optical, and Plasma Physics, 2008.

[24] J. Koverman, *The RF breakdown in high gradient cavities - comparative studies of RF and DC breakdowns.* PhD dissertation, RWTH Aachen, 2010.

[25] H. Timko, F. Djurabekova, K. Nordlund, L. Costelle, K. Matyash, R. Schnneider, A. Toerklep, G. Arnau-Izquierdi, and A. Descoeudres, "Mechanism of surface modification in the plasma-surface interaction in electrical arcs." (submitted for publication), 2010.

[26] H. Timko, K. Matyash, R. Schnneider, F. Djurabekova, K. Nordlund, A. Hansen, A. Descoeudres, J. Kovermann, A. Grudiev, W. Wuensch, S. Calatroni, and M. Taborelli, "A one-dimensional particle-in-cell model of plasma build-up in vacuum arcs." (submitted for publication), 2010.

[27] M. Stanczak, "A brief history of copper," *CSA Discovery Guides*, 2005.

[28] Deutschs Kupfer–Institut E.V., *Kupfer.* Deutschs Kupfer–Institut E.V., 1982.

[29] "http://public.web.cern.ch/public/en/research/lep-en.html."

[30] C. Benvenuti, N. Circelli, and M. Hauer, "Niobium films for superconducting accelerating cavities," *Appl. Phys. Lett.*, vol. 45, no. 5, pp. 583–584, 1984.

[31] S. Calatroni, "20 years of experience with the Nb/Cu technology for superconducting cavities and perspectives for future developments," *Physica C 441*, vol. 441, pp. 95–101, 2006.

[32] "http://linac4.web.cern.ch/linac4/."

[33] "http://www.tera.it."

[34] J. R. Davis, *ASM Specialty Handbook: Copper and Copper Alloys.* ASM International, 2001.

[35] "http://www.kupferinstitut.de."

[36] K. Dies, *Kupfer und Kupferlegierungen in der Technik.* Springer, 1967.

[37] L. Lu, Y. Shen, X. Chen, L. Qian, and K. Lu, “Ultrahigh strength and high electrical conductivity in copper,” *Science*, vol. 304, no. 5669, pp. 422–426, 2004.

[38] J. F. Nye, *Physical Properties of Crystals.* Walton Street, NY: Oxford University Press, first ed., 1995.

[39] P. K. Samal, “Brazing and diffusion bonding of GlidCop$^{©}$ dispersion strengthened copper,” tech. rep.

[40] “ASTM E1823 - 09b standard terminology relating to fatigue and fracture testing,” 2009.

[41] S. Suresh, *Fatigue of Materials.* Camebridge, UK: Camebridge University Press, second ed., 1998.

[42] D. C. Joy and G. R. Booker, “Recent developments in electron channelling techniques,” *Scanning Electron Microscopy*, pp. 137–144, 1973.

[43] Z. F. Zhang, Z. G. Wang, and Z. M. Sun:, “Evolution and mircrostructural characteristics of deformation bands in fatigued copper single crystals,” *Acta Materialia*, vol. 49, pp. 2875–2886, 2001.

[44] M. Hirao, H. Ogi, N. Suzuki, and T. Ohtani:, “Ultrasonic attenuation peak during fatigue of polycrystalline copper,” *Acta Materialia*, vol. 48, pp. 517–524, 2000.

[45] L. Cretegny and A. Saxena:, “AFM characterization of the evolution of surface deformation during fatigue in polycrystalline copper,” *Acta Materialia*, vol. 49, pp. 3755–3765, 2001.

[46] D. Kuhlman-Wilsdorf (Chap. Dislocations), *Physical Metallurgy.* North Holland, 2 ed., 1970.

[47] S. J. Basinski, Z. S. Basinski, and A. Howie, “Early stages of fatigue in copper single crystals,” *Philosophical Magazine*, vol. 19, pp. 899–924, 1969.

[48] H. Mughrabi, "Microscopic mechanisms of metal fatigue," in *The Strength of metals and Alloys* (V. G. P. Haasen and G. Kostorz, eds.), vol. 3, pp. 1615–1636, Oxford Pergamon Press, 1980.

[49] Z. S. Basinski, A. Korbel, and S. J. Basinski, "The temperature dependence of the saturation stress and dislaction structure in fatigued copper single crystals," *Acta Metallurgica*, vol. 28, pp. 191–207, 1980.

[50] Z. G. Wang, Z. F. Zhang, X. W. Li, W. P. Jia, and S. X. Li:, "Orientation dependence of the cyclic deformation behavior and the role of grain boundaries in fatigue damage in copper crystals," *Materials Science and Engineering A*, vol. 319-321, pp. 63–73, 2001.

[51] F. Ackerman, L. P. Kubin, J. Lepinoux, and H. Mughrabi, "The dependence of dislocation microstructure on plastic strain amplitude in cyclically strained copper single crystals," *Acta Metallurgica*, vol. 32, pp. 715–725, 1984.

[52] D. Hoeppner and G. Salviar, "The effect of crystallographic orientation on fatigue and fretting-initiated fatigue of copper single crystals," *Wear*, vol. 43, pp. 227–237, 1977.

[53] A. Cheng and C. Liard, "The high cycle fatigue life of copper single crystals tested under plastic-strain-controlled conditions," *Materials Science and Engineering*, vol. 51, pp. 55–60, 1981.

[54] A. Cheng and C. Liard, "Mechanisms of fatigue hardening in copper single crystals: The effects of strain amplitude and orientation," *Materials Science and Engineering*, vol. 51, pp. 111–121, 1981.

[55] J. Bauschinger, "Ueber die veraenderungen der elastizitaetsgrenze und der festigkeit des eisens und stahls durch strecken, quetschen, erwaermen, abkuehlen und durch oftmals wiederholte belastung," *Mitt: Mech-Tech Lab. XIII Muenchen*, vol. 13, pp. 1–115, 1886.

[56] S. Stanzl-Tschegg and H. Mayer, "Fatigue and fatigue crack growth of aluminium alloys at very high numbers of cycles," *International Journal of Fatigue*, vol. 23, pp. 231–237, 2001.

[57] H. Mughrabi, "Specific features and mechanisms of fatigue in the ultra–high–cycle regime," *International Journal of Fatigue*, vol. 28, pp. 1501–1508, 2006.

[58] B. Kaiser and C. Berger, "Fatigue behaviour of technical springs," *Materialwissenschaft und Werkstofftechnik*, vol. 36, no. 11, pp. 685–696, 2005.

[59] H. Mayer, "Ultrasonic torsion and tension-compression fatigue testing: Measuring principles and investigations on 2024-T351 aluminium alloy," *International Journal of Fatigue*, vol. 28, pp. 1446–1455, 2006.

[60] B. Holper, H. Mayer, A. Vasudevan, and S. Stanzl-Tschegg, "Near threshold fatigue crack growth at positive load ratio in aluminium alloys at low and ultrasonic frequency: influences of strain rate, slip behaviour and air humidity," *International Journal of Fatigue*, vol. 26, pp. 27–38, 2004.

[61] S. Stanzl-Tschegg, "Fatigue crack growth and thresholds at ultrasonic frequencies," *International Journal of Fatigue*, vol. 28, pp. 1456–1464, 2006.

[62] B. Zettl, H. Mayer, C. Ede, and S. Stanzl-Tschegg, "Very high cycle fatigue of normalized carbon steels," *International Journal of Fatigue*, vol. 28, pp. 1583–1589, 2006.

[63] S. E. Stanzl-Tschegg, H. Mughrabi, and B. Schoenbauer:, "Life time and cyclic slip of copper in the VHCF regime," *International Journal of Fatigue*, vol. 29, pp. 2050–2059, Sept. 2007.

[64] H. Mughrabi, "The cyclic hardening and saturation behavior of copper single crystals," *Materials Science and Engineering*, vol. 33, pp. 207–223, July 1978.

[65] C. Laird and G. Thomas, "On fatigue–induced reversion and overaging in dispersion strengthened alloy systems," *International Journal of Fracture Mechanics*, vol. 3, pp. 81–97, 1967.

[66] W. A. Wood, "Formation of fatigue cracks," *Philosophical Magazine*, vol. 3, pp. 692–699, 1958.

[67] U. Essman, U. Goesele, and H. Mughrabi, “A model of extrusions and intrusions in fatigued metals. I. point–defect production and the growth of extrusions,” *Philosophical Magazine A*, vol. 44, pp. 405–426, 1981.

[68] A. Hunsche and P. Neumann, “Quantitative measurement of persistent slip band profiles and crack initiation,” *Acta Metallurgica*, vol. 34, pp. 207–217, 1986.

[69] N. Thompson, N. J. Wadsworth, and N. Louat, “The origin of fatigue fracture in copper,” *Philosophical Magazine*, vol. 1, pp. 113–126, 1956.

[70] Z. S. Basinski, R. Pascual, and S. J. Basinski, “Low amplitude fatigue of copper single crystals – I. the role of the surface in fatigue failure,” *Acta Metallurgica*, vol. 31, pp. 591–602, 1983.

[71] S. Brinckmann, *On the Role of Dislocations in Fatigue Crack Initiation.* http://cms.web.cern.ch/cms/, Rijksuniversiteit Groningen, 2005.

[72] Y. V. Kostochkin, “Effect of thermal fatigue on the failure of turbine blades,” *Metal Science and Heat Treatment*, vol. 4, no. 7-8, pp. 305–307, 1962.

[73] G. S. Pisarenko and A. I. Petrenko, “One method of thermal fatigue testing of turbine blades,” *Metal Science and Heat Treatment*, vol. 8, no. 6, pp. 723–728, 1976.

[74] S. Bose and J. DeMasi-Marcin, “Thermal barrier coating experience in gas turbine engines at pratt & whitney,” *Journal of Thermal Spray Technology*, vol. 6, no. 1, pp. 99–104, 1997.

[75] R. Moenig, Y. B. Park, and C. A. Volkert, “Thermal fatigue in copper interconnects,” in *8th Int. Workshop on Stress-Induced Phenomena in Metallization* (E. Zschech, K. M. andP. S. Ho, H. Kawasaki, and T. Nakamura, eds.), pp. 147–156, American Institute of Physics, 2006.

[76] A. Fissolo, S. Amiable, O. Ancelet, F. Mermaz, J. Stelmaszyk, A. Constantinescu, C. Robertson, L. Vincent, V. Maillot, and F. Bouchet, “Crack initiation under thermal fatigue: An overview of CEA experience: Part I (of

II): Thermal fatigue appears to be more damaging than uniaxial isothermal fatigue," *International Journal of Fatigue*, vol. 31, no. 3, pp. 587 – 600, 2009.

[77] A. Fissolo, C. Gourdin, O. Ancelet, S. Amiable, A. Demassieux, S. Chapuliot, N. Haddar, F. Mermaz, J. Stelmaszyk, A. Constantinescu, L. Vincent, and V. Maillot, "Crack initiation under thermal fatigue: An overview of CEA experience: Part II (of II): Application of various criteria to biaxial thermal fatigue tests and a first proposal to improve the estimation of the thermal fatigue damage," *International Journal of Fatigue*, vol. 31, no. 7, pp. 1196 – 1210, 2009.

[78] "ISO 431:1981 - copper refinery shapes," 1981.

[79] "ASTM B224 -04 standard classification of coppers," 2004.

[80] "ASTM F68 - 05e1 standard specification for oxygen-free copper in wrought forms for electron devices," 2005.

[81] "ASTM B170 - 99(2004) standard specification for oxygen-free electrolytic copperrefinery shapes," 2004.

[82] CERN, "Technical specification: Bar copper OFE," Technical Specification 2001 - Ed. 7, CERN, 10 2006.

[83] "ASTM E8 / E8M - 09 standard test methods for tension testing of metallic materials," 2009.

[84] "ASTM E9 - 09 standard test methods of compression testing of metallic materials at room temperature," 2009.

[85] "ISO 409-1:1982 metallic materials – hardness test – tables of vickers hardness values for use in tests made on flat surfaces – part 1: HV5 to HV100," 1982.

[86] "ISO 409-2:1983 metallic materials – hardness test – tables of vickers hardness values for use in tests made on flat surfaces – part 2: HV0,2 to less than HV5," 1983.

[87] Foerster, *Operating Instructions Handbook SIGMATEST 2.069*, software version 4.06 ed.

[88] "ASTM E407 - 07 standard practice for microetching metals and alloys," 2007.

[89] "ASTM E112 - 96(2004)e2 standard test methods for determining average grain size," 2004.

[90] WYKO surface Profilers, *Technical Reference Manual.* VEECO Metrology group, version 2.2.1 ed., 1999.

[91] S. Calatroni, H. Neupert, and M. Taborelli, "Fatigue testing of materials by UV pulsed laser irradiation," CLIC Note 615, CERN, 2004.

[92] "ISO 4287:1997 geometrical product specifications (GPS) – surface texture: Profile method – terms, definitions and surface texture parameters," 1997.

[93] L. Reimer, *Scanning Electron Microscopy - Physics of Formation and Microanalysis.* Springer Verlag, Berlin, 1985.

[94] D. J. Dingley and V. Randle, "Microtexture determination by electron back-scatter diffraction," *Journal of Material Science*, vol. 27, pp. 4545–4566, 1992.

[95] V. Randle and O. Engler, *Texture Analysis - Macrotexture, Microtexture and Orientation Mapping.* CRC Press, Boca Raton, USA, 2000.

[96] L. D. Landau and E. M. Lifshitz, *Mechanics: Course of Theoretical Physics.* Butterworth Heinemann, 1982.

[97] O. I. HKL, *HKL Channel 5 Manual.* Oxford Instruments HKL, 2007.

[98] "ASTM E384 - 09 standard test method for microindentation hardness of materials," 2009.

[99] M. Goto, S. Han, T. Yakushiji, S. S. Kim, and C. Y. Lim, "Fatigue strength and formation behavior of surface damage in ultrafine

grained copper with different non-equilibrium microstructures," *International Journal of Fatigue*, vol. 30, pp. 1333–1344, 2008.

[100] T. Hanlon, Y.-N. Kwon, and S. Suresh, "Grain size effects on the fatigue response of nanocrystalline metals," *Scripta Materialia*, vol. 49, pp. 675–680, 2003.

[101] T. Hanlon, E. Tabachnikov, and S. Suresh, "Fatigue behavior of nanocrystalline metals and alloys," *International Journal of Fatigue*, vol. 4927, p. 11471158, 2005.

[102] A. Vinogradov, S. Hashimoto, and V. Kopylov, "Enhanced strength and fatigue life of ultra–fine grain Fe-36Ni invar alloy," *Materials Science and Engineering*, vol. A355, pp. 277–285, 2003.

[103] D. Smith, *Thin-film Deposition. Principles and Practice.* McGraw-Hill, Inc., New York, 1995.

[104] A. Prodromides, *Non-Evaporable Getter Thin Film Coatings for Vacuum Applications.* PhD thesis, EPFL Lausanne, 2002.

[105] "http://www.gencoa.com/."

[106] R. Stuart, *Vacuum Technology, Thin Films, and Sputtering. An Introduction.* Academic Press, Inc. Orlando, Florida, 32887, 1983.

[107] A. Richardt and A.-M. Durand, *Le Vide: Les Couches Minces, Les Couches Dures.* In Fine, 1994.

[108] J. Thornton, "High rate thick film growth," *Annual Review of Material Sciences*, vol. 7, pp. 239–260, 1977.

[109] J. A. Thornton, "Influence of apparatus geometry and deposition conditions on the structure and topography of thick sputtered coatings," *Journal of Vacuum Science and Technology*, vol. 11, no. 4, pp. 666–670, 1974.

[110] ICDD International Centre for Diffraction Data, "PDF-2 database release A6," 1991.

[111] G. B. Harris, "Quantitative measurement of preferred orientation in rolled uranium bars," *Philosophical Magazine*, vol. 43, pp. 113–123, 1952.

[112] V. Valvoda and M. Jaervinen, "On the harris texture index," *Powder Diffraction*, vol. 5, no. 4, pp. 200–203, 1992.

[113] M. A. Peck, *Structural and Superconducting properties of sputter–deposited niobium films for application in RF accelerating cavities.* PhD thesis, Technische Unversitaet, Wien, 2000.

[114] B. Cullity and S. Stock, *Elements of X-Ray Diffraction.* Prentice Hall, 3rd ed., 2001.

[115] W. A. Rachinger, "A correction for the $\alpha 1$:$\alpha 2$ doublet in the measurement of widths of X-ray diffraction lines," *Journal of Scientific Instruments*, vol. 25, pp. 254–259, 1948.

[116] "ISO 1099:2006 metallic materials – fatigue testing – axial force-controlled method," 2006.

[117] S. Heikkinen, *Study of High Power RF Induced Thermal Fatigue in the High Gradient Accelerating Structures.* PhD dissertation, Helsinki University, 2007.

[118] M. Aicheler, "Internal note." unpublished.

[119] D. E. Gray, *American Institute of Physics Handbook.* Mcgraw-Hill, 3rd ed., 1972. ISBN 9780070014855.

[120] J. Huopana, "Internal note." unpublished.

[121] V. Dolgashev, S. Tantawi, and Y. Higashi, "Status of high gradient tests of normal conducting single-cell structures." Presentation in Advanced Accelerator Concepts Workshop, July 2008.

[122] C. Nantista, S. Tantawi, J. Weisend, R. Siemann, and V. Dolgashev, "Test bed for superconducting materials," in *Proceedings of Particle Accelerator Conference. 16-20 May 2005, Knoxville(TN, USA)*, pp. 4227–4229, 2005.

[123] H.-J. Bunge, *Texture analysis in materials science: mathematical methods.* Butterworths, 1982.

[124] S. I. Wright, M. M. Nowell, and J. F. Bingert, “A comparison of textures measured using x-ray and electron backscatter diffraction,” *Metallurgical and Materials Transactions A*, vol. 38, pp. 1845–1855, 2007. 10.1007/s11661-007-9226-2.

[125] Stanzl-Tschegg, “Fracture mechanisms and fracture mechanics at ultrasonic frequencies,” *Fatigue & fracture of engineering materials & structures*, vol. 22, pp. 567–579, July 1999.

[126] Stanzl-Tschegg, “Influence of microstructure and load ratio on fatigue threshold behavior in 7075 aluminum alloy,” *International Journal of Fatigue*, vol. 21, pp. 255–262, July 1999.

[127] D. P. Pritzkau, *RF Pulsed Heating.* PhD thesis, Stanford Linear Accelerator Center, 2001.

[128] D. P. Pritzkau and R. H. Siemann, “Experimental study of rf pulsed heating on oxygen free electronic copper,” *Physical Review Special Topics - Accelerators and Beams*, vol. 5, pp. 1–22, 2002.

[129] J. Steigman, “The self-diffusion of copper,” *Physical Review*, vol. 56, pp. 13–21, 1939.

[130] A. Kuper, H. Letaw, L. Slifkin, E-Sonder, and C. T. Tomizuka, “Self-diffusion in copper,” *Physical Review*, vol. 96, no. 5, pp. 1224–1225, 1954.

[131] C. Upthegrove and H. Burghoff, “ASTM special technical publication no. 181.elevated temperature properties of copper and copper base alloys,” tech. rep., ASTM International, 1956.

[132] A. Chamat, M. Abbadi, J. Gilgert, F. Cocheteux, and Z. Azari, “A new non-local criterion in high-cycle multiaxial fatigue for non-proportional loadings,” *International Journal of Fatigue*, vol. 29, pp. 1465–1474, 2007.

[133] T. Delahaye, *Developpement d'une methode probabiliste de calcul en fatigue multiaxiale prenant en compte la repartition volumique des contraintes.* PhD thesis, L'Universite de Bordeaux, 2004.

[134] C. Doudard, S. Calloch, and F. Hild, "Fatigue multiaxiale : un point de vue probabiliste," in *Congres Francais de Mecanique*, no. 17, 2005.

[135] M. Sauzay and T. Jourdan, "Polycrystalline microstructure, cubic elasticity and nucleation of high-cycle fatigue cracks," *International Journal of Fracture*, vol. 141, pp. 431–446, 2006.

[136] M. Sauzay, "Cubic elasticity and stress distribution at the free surface of polycrystals," *Acta Materialia*, vol. 55, pp. 1193–1202, 2007.

[137] M. Papakyriacou, H. Mayer, C. Pypen, H. P. Jr., and S. Stanzl-Tschegg, "Influence of loading frequency on high cycle fatigue properties of b.c.c. and h.c.p. metals," *Materials Science and Engineering*, vol. A308, pp. 143–152, 2001.

[138] Y.-B. Park, R. Mnig, and C. A. Volkert, "Frequency effect on thermal fatigue damage in Cu interconnects," *Thin Solid Films*, vol. 515, pp. 3253–3258, 2007.

[139] S. Baker, A. Kretschmann, and E. Arzt, "Thermo mechanical behavior of different texture components in Cu thin films," *Acta Materialia*, vol. 49, pp. 2145–2160, 2001.

[140] A. Wikstroem and M. Nygards, "Anisotropy and texture in thin copper films - an elasto-plastic analysis," *Acta Materialia*, vol. 50, pp. 857–870, 2002.

[141] R. Moenig, *Thermal Fatigue of Cu Thin Films.* PhD dissertation, Universitaet Stuttgart, 2005.

List of Figures

2.1. Overall layout CLIC 3 TeV. Generation, acceleration and delivery of the main beams in the lower half. The drive-beam complex and the production of 12 GHz RF–power are situated in the upper half [3]. 4

2.2. Proposed CLIC tunnel cross section. The main beam linac and the drive beam are installed on individual girders on a common concrete base. Transfer lines carry the main- and drive-beams from the generation complexes to their respective injection points and connect cooling and ventilation facilities [19]. 5

2.3. Scheme of AS consisting of brazed discs. Bunches of particles are accelerated by the RF fields and pass in center of irises. The particle beam induces wake fields, which are transported away from the center by the damping wave guides and are damped in the silicon carbide loads [3]. 6

2.4. Softening resistance of GlidCop Al-15© (C15700) versus cold-worked OF copper and cold–worked Zirconium Copper. Properties measured at RT, after exposure to elevated temperatures for one hour. From [39] 10

2.5. Influence of alloying element and content on electrical conductivity of pure copper. From [34] 11

2.6. Determination of the different fatigue regimes in S-N Woehler plot according to [11]. Material with or without a plastic strain fatigue limit in the HCF regime (range II), terminated by a further decrease of fatigue life with decreasing strain amplitude below the PSB-threshold in the UHCF regime (range III). 15

4.1. Microstructure of cold drawn OFE copper in temper state H02 . 24

4.2. Microstructure of “brazing annealed” OFE copper obtained by standard (825 °C) vacuum brazing cycle. 25

4.3. Microstructure of “dead soft annealed” OFE copper obtained by annealing at 1000 °C for 2 h in vacuum. 26

4.4. a) from [45] fatigued polycrystalline copper for 6900 cycles at $\Delta\epsilon_{tot}/2 = 2.5$ x 10^{-3}. Individual feature size in the order of 1 μm in height and 10 μm width. b) from [63] fatigued polycrystalline copper for 1.3 x 10^{10} cycles at $\Delta\epsilon_{tot}/2 = 4.8$ x 10^{-4}. Individual feature size in the order of 0.2 μm in height and 0.5 μm width. . 27

4.5. Sample geometry and dimensions of standard tensile test sample complying [83, 84] 28

4.6. Plasma enhanced PVD setup applied. 34

4.7. X-Ray diffractometer in Bragg-Brentano configuration 36

4.8. Example of data of diffraction pattern from copper powder. . . . 37

4.9. Calculated penetration depth τ of CuKα radiation in copper as a function of diffraction angle. τ is defined as the thickness of the material that contributes to 99% of the diffracted intensity. . . . 38

4.10. Fraction f of diffracted signal coming from film of 9 μm thickness (solid line) and of 20 μm thickness (dashed line) 39

4.11. Geometry of sample for conventional fatigue testing 40

4.12. Hourglass–shaped USS test sample bolted to the resonator. Sample is designed to feature first resonant frequency at 24 kHz. Sample head in cone shape reduces cavitation pitting from cooling water 41

4.13. Equivalent (von-Mises) a) strain and b) stress distribution in a cross section of an USS sample. Stresses are very concentrated in the surface regions whereas the high strain region covers almost all the cross section. 42

4.14. Distribution of normal stresses in a) circumference and b) longitudinal direction. Longitudinal component in gage length very large (84 MPa compressive) compared to circumference component (8 MPa compressive) 43

4.15. Sample after laser irradiation. 25 dark spots each with 5 x 10^4 shots with an energy density of 0.3 J/cm^2 44

4.16. Simulated temperature and stress component evolution in time during laser irradiation, assuming fully elastic isotropic material behaviour. Laser pulse length is 30 ns and energy density is 0.3 J/cm^2. In–Plane components (x = y) are similar compressive stresses whereas the out–of–plane component (z) remains zero . 45

4.17. Simulated temperature and stress component evolution in depth, same conditions as in Fig. 4.16. In–Plane components (x = y) decay in similar manners and become zero at a depth of 7 μm. Out–of–Plane component (z) stays zero. 46

4.18. RF fatigue test sample. The graph depicts the magnetic field intensity distribution along the radius: low intensity at $R = 0$, maximum intensity at $R = R_{Imax.} > 0$ and again low intensity at $R > R_{Imax.}$. The lighter shading in the inner ring marks the damaged area, where the maximum temperature rise of $\Delta T_{max} = 110$ K took place. The damage caused to the outer region, the result of sample clamping, is of no interest for the current purpose. 48

5.1. SEM pictures of surface fatigued by laser with 0.3 J/cm^2 ($\Rightarrow \Delta T = 180$ K and $\epsilon_{eq} = 5.1 \text{ x } 10^{-3}$) after 5 x 10^4 cycles. 52

5.2. SEM pictures of Cu H02 sample fatigued by laser with 0.2 J/cm^2 ($\Rightarrow \Delta T = 120$ K and $\epsilon_{eq} = 3.4 \text{ x } 10^{-3}$) after a) 1.2 x 10^4 b) 6 x 10^4 and c) 2.4 x 10^5 cycles. 53

5.3. Roughness evolution over cycle numbers from Fig. 5.2 54

5.4. SEM pictures of surface fatigued by laser after 1.2 x 10^4 cycles for a) 0.2 J/cm^2 ($\Rightarrow \Delta T = 120$ K and $\epsilon_{eq} = 3.4 \text{ x } 10^{-3}$) and b) 0.5 J/cm^2 ($\Rightarrow \Delta T = 300$ K and $\epsilon_{eq} = 8.5 \text{ x } 10^{-3}$). 55

5.5. SEM picture of Cu H02 sample fatigued by RF after 10^7 cycles in highest $\Delta T = 110$ K ($\Rightarrow \epsilon_{eq} = 3.1 \text{ x } 10^{-3}$) region. Dark and light regions correspond to smooth and rough surfaces. Surface cracks can be observed in areas of extreme contrast. 55

5.6. SEM pictures of Cu H02 sample fatigued by RF after 10^7 cycles for a) $\Delta T \approx 80$ K ($\Rightarrow \epsilon_{eq} \approx 2.3 \text{ x } 10^{-3}$) and b) $\Delta T = 110$ K ($\Rightarrow \epsilon_{eq} = 3.1 \text{ x } 10^{-3}$). 56

5.7. SEM picture of USS fatigued copper H02 sample in highest load region (ϵ_{eq} = 8.0 x 10^{-4}) showing individual lamellae. 57

5.8. SEM picture of USS fatigued sample in crack region. Higher magnification shows extrusions at main crack and secondary cracks. 58

5.9. SEM images of electropolished Cu H02 sample fatigued by USS with 6 x 10^9 cycles a) in a medium strain region ($\epsilon_{eq} \approx$ 6.0 x 10^{-4}) and b) at the center of gage length (ϵ_{eq} = 8.0 x 10^{-4}) 59

5.10. SEM images of surfaces for grain orientation of a) [1 0 0], b)[1 1 1] and c)[1 1 0] following 5 x 10^4 laser cycles at 0.3 J/cm^2 ($\Rightarrow$ ΔT = 180 K and ϵ_{eq} = 5.1 x 10^{-3}) 59

5.11. Comparison of roughness measured in non–irradiated area (reference) and the grains in Fig. 5.10. For the definition of $SI-1$ see Chap. 4.2.2. The [1 0 0] grain shows almost no difference with respect to the reference whereas the roughness in the [1 1 0] grain increased significantly during the cycling. The roughness values of the [1 1 1] grain are between [1 0 0] and [1 1 0]. 60

5.12. SEM pictures of Cu H02 sample fatigued by RF after 10^7 cycles in ΔT = 110 K region ($\Rightarrow$ ϵ_{eq} = 3.1 x 10^{-3}). Only main grain orientations are highlighted as identified by EBSD. 61

5.13. SEM picture of USS sample in center of gage length (ϵ_{eq} = 8.0 x 10^{-4}). Grain orientations and boundaries high lighted as identified by EBSD. Grains are numbered G1 to G6. Central [1 0 0] grain shows no roughening; [1 1 1] grains show severe, moderate or no roughening. Dark spots are electro polishing artifacts. 62

5.14. SEM image of annealed copper surface fatigued by laser with 0.3 J/cm^2 ($\Rightarrow$ ΔT = 180 K and ϵ_{eq} = 5.1 x 10^{-3}) after 5 x 10^4 cycles. GB between [1 0 0] and [1 1 1] grain. Surface modification bands are visible in GB vicinity. 64

5.15. SEM image of annealed copper surface fatigued by laser with 0.3 J/cm^2 ($\Rightarrow$ ΔT = 180 K hence ϵ_{eq} = 5.1 x 10^{-3}) after 5 x 10^4 cycles. GB's of type: [1 0 0] – [1 1 0]. Plot a) large modification zone visible. Plot b) no modification zone visible. 65

5.16. SEM pictures of Cu H02 sample fatigued by RF after 10^7 cycles in highest ΔT = 110 K region ($\Rightarrow \epsilon_{eq} = 3.1 \text{ x } 10^{-3}$). GB between [1 0 0] and [1 1 1] grain. Large modification zone visible in GB vicinity. 66

5.17. Hardness (HV) as a function of cycle numbers on annealed copper sample, fatigued by laser at 0.3 J/cm^2 ($\Rightarrow \Delta$T = 180 K and $\epsilon_{eq} = 5.1 \text{ x } 10^{-3}$). 67

5.18. Plot of microhardness as a function of radial position on RFF fatigued samples after 10^7 cycles at maximum ΔT = 110 K ($\Rightarrow \epsilon_{eq} = 3.1 \text{ x } 10^{-3}$). Plot a) H02-Cu and dead–soft annealed Cu. Plot b) single crystal oriented in [1 0 0] direction (courtesy of KEK and SLAC). T110 represents the calculated radial distribution of ΔT. 67

5.19. Micro hardness as a function of equivalent strain on RFF fatigued [1 0 0] single crystal after 10^7 cycles at maximum ΔT = 110 K ($\Rightarrow \epsilon_{eq} = 3.1 \text{ x } 10^{-3}$). 68

5.20. Hardness increase of main orientations after 5 x 10^4 cycles with 0.3 J/cm^2 ($\Rightarrow \Delta$T = 180 K and $\epsilon_{eq} = 5.1 \text{ x } 10^{-3}$) 69

5.21. Comparison of Hardness (HV) with surface roughness (*Ra*) over cycle numbers on annealed copper sample, fatigued by laser at 0.3 J/cm^2 ($\Rightarrow \Delta$T = 180 K and $\epsilon_{eq} = 5.1 \text{ x } 10^{-3}$). 70

5.22. Surface roughness (*Ra*) over Hardness (HV) for lower (filled symbols) and higher (hollow symbols) cycle numbers on annealed copper sample. Same data as in Fig. 5.21. 71

5.23. a) Roughness and hardness of the main orientations in the initial state and after 5 x 10^4 cycles with 0.3 J/cm^2 ($\Rightarrow \Delta$T = 180 K and $\epsilon_{eq} = 5.1 \text{ x } 10^{-3}$). b) Same data as in a) but with the roughness increase plotted directly versus the hardness increase. 72

5.24. Microhardness as a function of equivalent strain on RFF fatigued [1 0 0] copper single crystal after 10^7 cycles at maximum ΔT = 110 K ($\Rightarrow \epsilon_{eq} = 3.1 \text{ x } 10^{-3}$) compared to dead–soft annealed copper LAF fatigued after 5 x 10^4 cycles with 0.3 J/cm^2 ($\Rightarrow \Delta$T = 180 K and $\epsilon_{eq} = 5.1 \text{ x } 10^{-3}$) 73

5.25. a) and b) grain maps of SS3 and Cu3 as obtained by EBSD as basis for grain size calculations. c) and d) logarithmic grain area distribution of SS3 and Cu3. 74
5.26. EBSD results of Cu2 sample. a) grain orientation map b) inverse pole figure color–orientation code c) inverse pole figure density distribution (MUD factor) 76
5.27. Comparison of roughness evolution on annealed bulk copper with best (SS3) and worst (Cu2) performing copper thin film after LAF with 0.3 J/cm^2 ($\Rightarrow \Delta$T = 180 K and ϵ_{eq} = 5.1 x 10^{-3}). 78
5.28. S–N plot of fatigue data obtained with LAF, USS and CVF on H02 temper (solid symbols) and on brazing annealed copper (hollow symbols). For comparison, the literature value for H02 copper [34] and the CLIC target [117] is plotted. USS data partly from [117]. 79

6.1. Schematic of influence of Schmid factor on local shear strain in uniaxial single crystal under tensile strain oriented for single slip: (a) An elongation ΔL is imposed on a sample of the length L. When slip system has low Schmid factor (b) local high shear strain is needed to accommodate ΔL, whereas in (c) a higher Schmid factor results in lower local strain. 91
6.2. Schematic showing the form of strain and stress distributions during elastic deformation in thin film after Baker et al. [139]. Grains oriented [1 1 1] and [1 0 0] out of surface accommodate stress within one film thickness to either side of the GB: case a) large grain size results in same average strain in both grains (isostrain case); case b) small grain size results in same stress in adjacent grains (isostress case) 93

A.1. Detailed Schmid factor analysis with orientation illustration for biaxial stress state 124
A.2. Detailed Schmid factor analysis with orientation illustration for uniaxial stress state: in–plane rotation 0° 125
A.3. Detailed Schmid factor analysis with orientation illustration for uniaxial stress state: in–plane rotation 30° 126

A.4. Detailed Schmid factor analysis with orientation illustration for uniaxial stress state: in–plane rotation 45° 127

A.5. Detailed Schmid factor analysis with orientation illustration for the sample shown in Fig. 5.13. The two maximum SF for each grain are highlighted in gray 128

A.6. Combination of results of thin film characterisation. Sample SS2: a) logarithmic grain area distribution. b) inverse pole figure (color–orientation code) and texture results: inverse pole figure density distribution (MUD factor) and XRD data. c) image–quality map. d) grain map. e) SEM picture 129

A.7. Combination of results of thin film characterisation. Sample Cu2: a) logarithmic grain area distribution. b) inverse pole figure (color–orientation code) and texture results: inverse pole figure density distribution (MUD factor) and XRD data. c) image–quality map. d) grain map. e) SEM picture 130

A.8. Combination of results of thin film characterisation. Sample SS3: a) logarithmic grain area distribution. b) inverse pole figure (color–orientation code) and texture results: inverse pole figure density distribution (MUD factor) and XRD data. c) image–quality map. d) grain map. e) SEM picture 131

A.9. Combination of results of thin film characterisation. Sample Cu3: a) logarithmic grain area distribution. b) inverse pole figure (color–orientation code) and texture results: inverse pole figure density distribution (MUD factor) and XRD data. c) image–quality map. d) grain map. e) SEM picture 132

A.10. Combination of results of thin film characterisation. Sample SS4: a) logarithmic grain area distribution. b) inverse pole figure (color–orientation code) and texture results: inverse pole figure density distribution (MUD factor) and XRD data. c) image–quality map. d) grain map. e) SEM picture 133

A.11. Combination of results of thin film characterisation. Sample Cu4: a) logarithmic grain area distribution. b) inverse pole figure (color–orientation code) and texture results: inverse pole figure density distribution (MUD factor) and XRD data. c) image–quality map. d) grain map. e) SEM picture 134
A.12. Combination of results of thin film characterisation. Sample SS5: a) logarithmic grain area distribution. b) inverse pole figure (color–orientation code) and texture results: inverse pole figure density distribution (MUD factor) and XRD data. c) image–quality map. d) grain map. e) SEM picture 135
A.13. Combination of results of thin film characterisation. Sample Cu5: a) logarithmic grain area distribution. b) inverse pole figure (color–orientation code) and texture results: inverse pole figure density distribution (MUD factor) and XRD data. c) image–quality map. d) grain map. e) SEM picture 136
A.14. Combination of results of thin film characterisation. Sample SS6: a) logarithmic grain area distribution. b) inverse pole figure (color–orientation code) and texture results: inverse pole figure density distribution (MUD factor) and XRD data. c) image–quality map. d) grain map. e) SEM picture 137
A.15. Combination of results of thin film characterisation. Sample Cu6: a) logarithmic grain area distribution. b) inverse pole figure (color–orientation code) and texture results: inverse pole figure density distribution (MUD factor) and XRD data. c) image–quality map. d) grain map. e) SEM picture 138

List of Tables

2.1. Electrical and thermal conductivity values for various metals and alloys (from [34]). 9

4.1. Comparison of measured mechanical properties of copper tempers used for the experiments. 23
4.2. Correspondence between hkl notation and Euler notation for main orientations. “x” means arbitrary value possible. 31
4.3. Process parameters for plasma sputtering of copper thin films on twin sample pairs (copper substrate “Cux” and stainless steel substrate “SSx”, coated at the same time). Film thicknesses are derived from process parameters. 35
4.4. Comparison of the four fatigue test benches and commonly used test parameters 49

5.1. Euler angles of grains in Fig. 5.13 and illustration of orientation of elementary cell with respecto to the surface. SF on primary and secondary slip system SF1 and SF2. Qualitative roughening category. 63
5.2. Average grain areas of the thin films measured with EBSD . . . 75
5.3. Diffraction data from PDF file and measured with XRD on pure copper powder. Relative intensities and angular position of intensity maxima. 75
5.4. T_{hkl} values and corresponding MUD–factors for each thin film. Additionally maxima values of both as measure of degree of texture. 77

A. Appendix

A.1. Schmid Factors

Bi-Axial load x-y

	Plane	Direction	(100)	(110)	(111)
1	{1 1 1}	(1 -1 0)	0	0	-0.27
2	{1 1 1}	(1 0 -1)	0.41	0	0
3	{1 1 1}	(0 1 -1)	0.41	0	0.27
4	{1 -1 1}	(1 1 0)	0	0.41	0
5	{1 -1 1}	(1 0 -1)	0.41	0.41	0
6	{1 -1 1}	(0 1 1)	-0.41	0	0
7	{1 1 -1}	(1 -1 0)	0	0.41	0.27
8	{1 1 -1}	(1 0 1)	0.41	0.41	0.27
9	{1 1 -1}	(0 1 1)	0.41	0	0
10	{-1 1 1}	(1 1 0)	0	0	0
11	{-1 1 1}	(1 0 1)	-0.41	0	0.27
12	{-1 1 1}	(0 1 -1)	0.41	0	-0.27
Max:			0.41	0.41	0.27
Sum:			1.63	1.63	0.54
Sum Absolute:			3.27	1.63	1.63

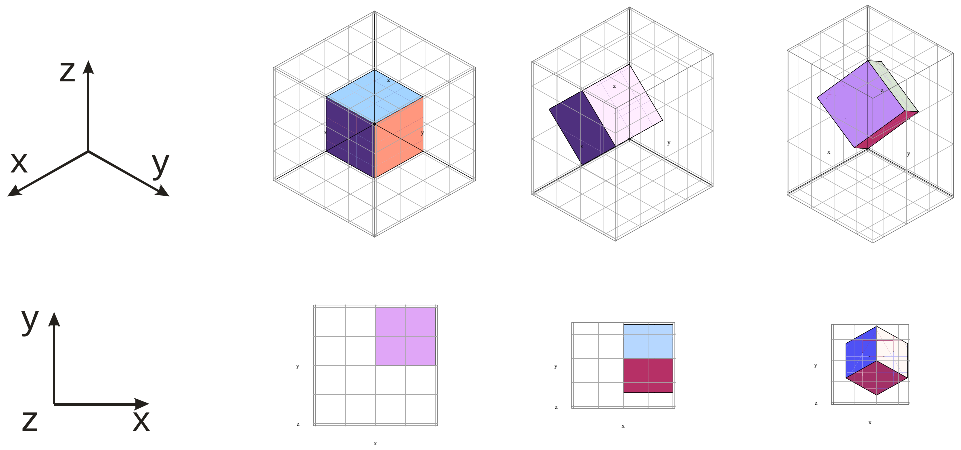

Figure A.1.: Detailed Schmid factor analysis with orientation illustration for biaxial stress state

Uni-Axial load in x-direction; In-Plane rotation 0°

	Plane	Direction	(100)	(110)	(111)
1	{1 1 1}	(1 -1 0)	0.41	0.41	0
2	{1 1 1}	(1 0 -1)	0.41	0.41	0.41
3	{1 1 1}	(0 1 -1)	0	0	0.41
4	{1 -1 1}	(1 1 0)	0.41	0.41	0
5	{1 -1 1}	(1 0 -1)	0.41	0.41	0
6	{1 -1 1}	(0 1 1)	0	0	0
7	{1 1 -1}	(1 -1 0)	0.41	0.41	0
8	{1 1 -1}	(1 0 1)	0.41	0.41	0.41
9	{1 1 -1}	(0 1 1)	0	0	0.41
10	{-1 1 1}	(1 1 0)	-0.41	-0.41	0
11	{-1 1 1}	(1 0 1)	-0.41	-0.41	0
12	{-1 1 1}	(0 1 -1)	0	0	0
Max:			0.41	0.41	0.41
Sum:			1.63	1.63	1.63
Sum Absolute:			3.27	3.27	1.63

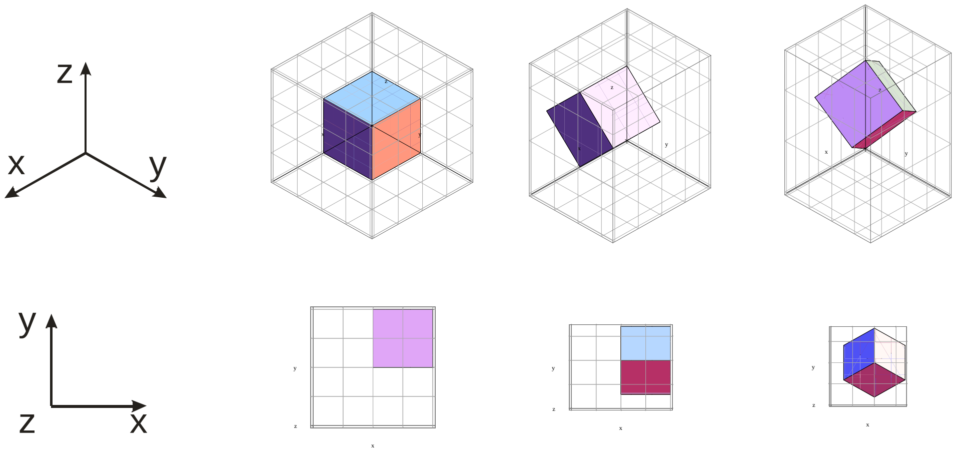

Figure A.2.: Detailed Schmid factor analysis with orientation illustration for uniaxial stress state: in–plane rotation 0°

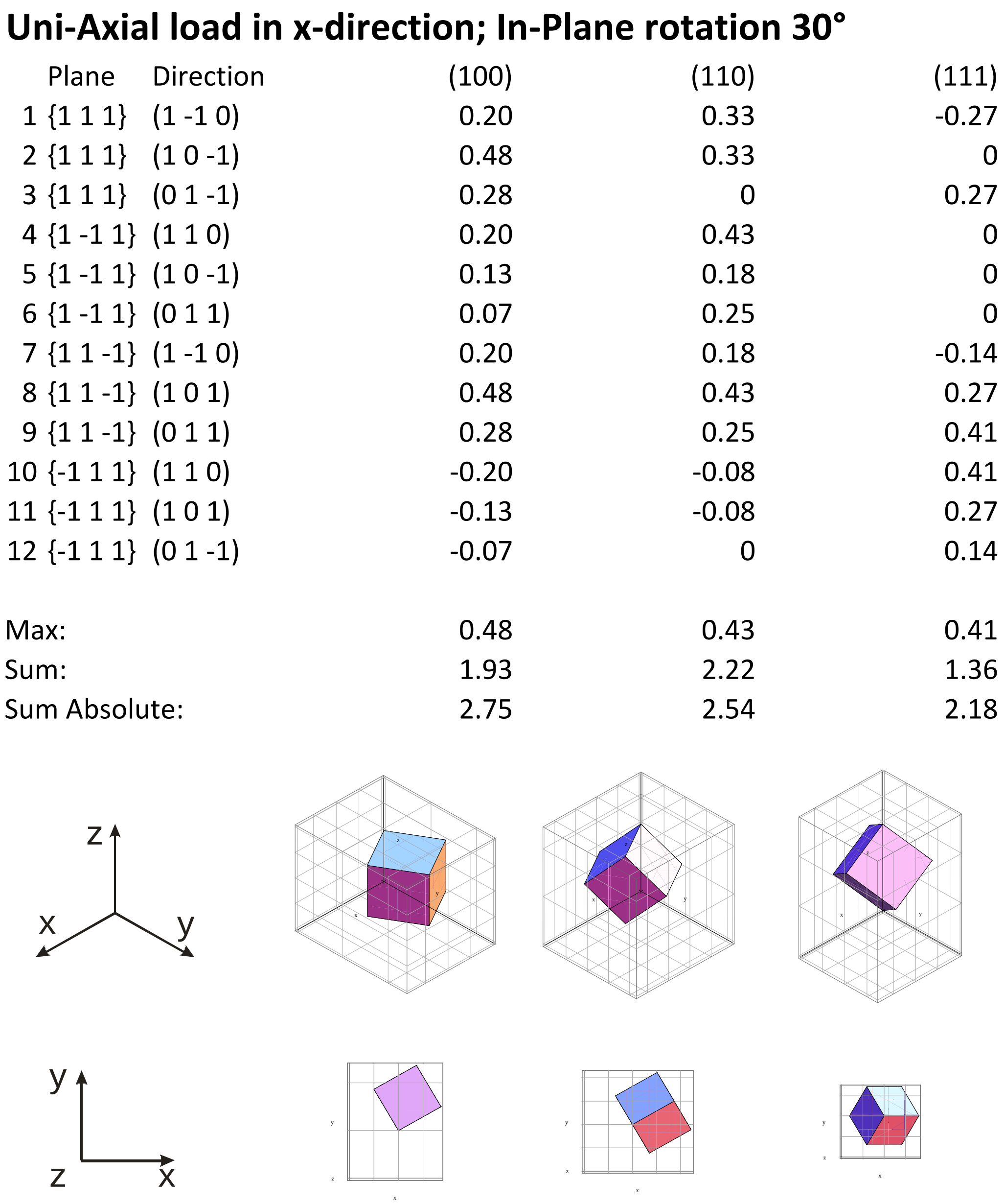

Uni-Axial load in x-direction; In-Plane rotation 30°

	Plane	Direction	(100)	(110)	(111)
1	{1 1 1}	(1 -1 0)	0.20	0.33	-0.27
2	{1 1 1}	(1 0 -1)	0.48	0.33	0
3	{1 1 1}	(0 1 -1)	0.28	0	0.27
4	{1 -1 1}	(1 1 0)	0.20	0.43	0
5	{1 -1 1}	(1 0 -1)	0.13	0.18	0
6	{1 -1 1}	(0 1 1)	0.07	0.25	0
7	{1 1 -1}	(1 -1 0)	0.20	0.18	-0.14
8	{1 1 -1}	(1 0 1)	0.48	0.43	0.27
9	{1 1 -1}	(0 1 1)	0.28	0.25	0.41
10	{-1 1 1}	(1 1 0)	-0.20	-0.08	0.41
11	{-1 1 1}	(1 0 1)	-0.13	-0.08	0.27
12	{-1 1 1}	(0 1 -1)	-0.07	0	0.14
Max:			0.48	0.43	0.41
Sum:			1.93	2.22	1.36
Sum Absolute:			2.75	2.54	2.18

Figure A.3.: Detailed Schmid factor analysis with orientation illustration for uniaxial stress state: in–plane rotation 30°

Uni-Axial load in x-direction; In-Plane rotation 45°

	Plane	Direction	(100)	(110)	(111)
1	{1 1 1}	(1 -1 0)	0	0.14	-0.37
2	{1 1 1}	(1 0 -1)	0.41	0.14	-0.24
3	{1 1 1}	(0 1 -1)	0.41	0	0.14
4	{1 -1 1}	(1 1 0)	0	0.35	0
5	{1 -1 1}	(1 0 -1)	0	0.06	0
6	{1 -1 1}	(0 1 1)	0	0.29	0
7	{1 1 -1}	(1 -1 0)	0	0.06	-0.10
8	{1 1 -1}	(1 0 1)	0.41	0.35	0.14
9	{1 1 -1}	(0 1 1)	0.41	0.29	0.24
10	{-1 1 1}	(1 1 0)	0	0.14	0.47
11	{-1 1 1}	(1 0 1)	0	0.14	0.37
12	{-1 1 1}	(0 1 -1)	0	0	0.10
Max:			0.41	0.35	0.47
Sum:			1.63	1.97	0.74
Sum Absolute:			1.63	1.97	2.16

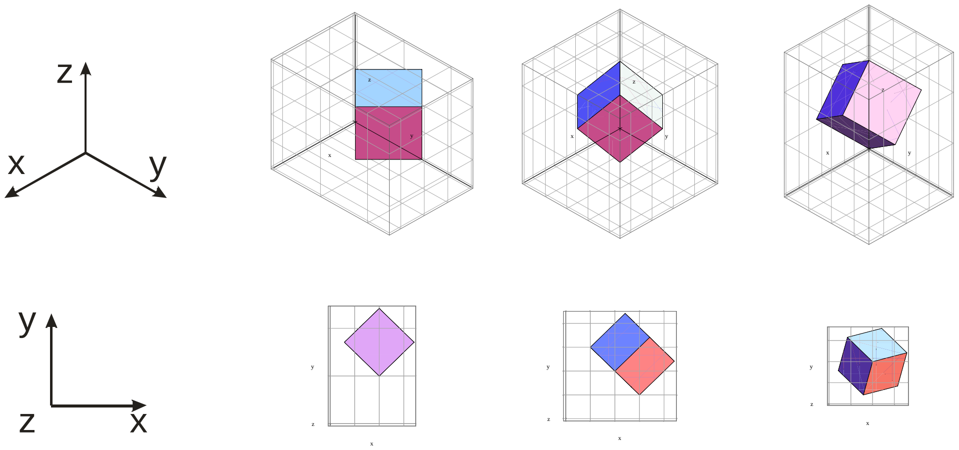

Figure A.4.: Detailed Schmid factor analysis with orientation illustration for uniaxial stress state: in–plane rotation 45°

UniAxial CASE in x-Direction! Brazed Sonotrode Grain Analyse!!!!

Plane	Direct	Grain1	Grain2	Grain3	Grain4	Grain5	Grain6
1 {1 1 1}	(1 -1 0)	0.15	0.21	-0.42	-0.44	0.21	-0.14
2 {1 1 1}	(1 0 -1)	0.49	0.50	-0.10	-0.22	0.50	-0.19
3 {1 1 1}	(0 1 -1)	0.34	0.29	0.31	0.22	0.29	-0.05
4 {1 -1 1}	(1 1 0)	0.07	0.16	-0.14	-0.09	0.17	0.04
5 {1 -1 1}	(1 0 -1)	0.05	0.12	0.02	0.03	0.13	0.17
6 {1 -1 1}	(0 1 1)	0.02	0.04	-0.16	-0.12	0.04	-0.13
7 {1 1 -1}	(1 -1 0)	0.19	0.25	-0.20	-0.14	0.26	0.40
8 {1 1 -1}	(1 0 1)	0.41	0.45	0.18	0.13	0.45	-0.01
9 {1 1 -1}	(0 1 1)	0.21	0.20	0.38	0.27	0.20	-0.41
10 {-1 1 1}	(1 1 0)	-0.27	-0.30	0.49	0.49	-0.30	-0.22
11 {-1 1 1}	(1 0 1)	-0.13	-0.17	0.26	0.32	-0.17	0.02
12 {-1 1 1}	(0 1 -1)	-0.14	-0.13	0.22	0.18	-0.13	-0.24
Max:		0.49	0.50	0.49	0.49	0.50	0.41
Sum:		1.38	1.63	0.84	0.63	1.63	-0.76
SumAbs:		2.47	2.82	2.89	2.64	2.84	2.02

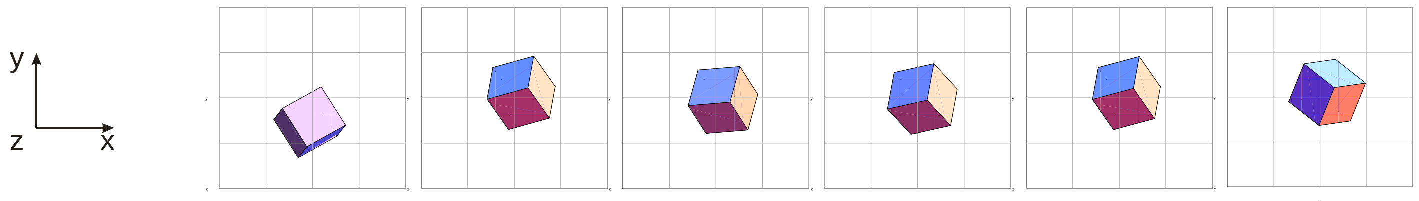

Euler angels:	Euler angels:	Euler angels:	Euler angels:	Euler angels:	Euler angels:
Eu1=142.8°	Eu1=350°	Eu1=212°	Eu1=222°	Eu1=350°	Eu1=278.5°
Eu2=17.8°	Eu2=45.2°	Eu2=46.4°	Eu2=48.8°	Eu2=45.5°	Eu2=43.3°
Eu3=68.0°	Eu3=34.7°	Eu3=53.4°	Eu3=49.8°	Eu3=34.2°	Eu3=51.6°

Figure A.5.: Detailed Schmid factor analysis with orientation illustration for the sample shown in Fig. 5.13. The two maximum SF for each grain are highlighted in gray

A.2. Thin Film Characterisation

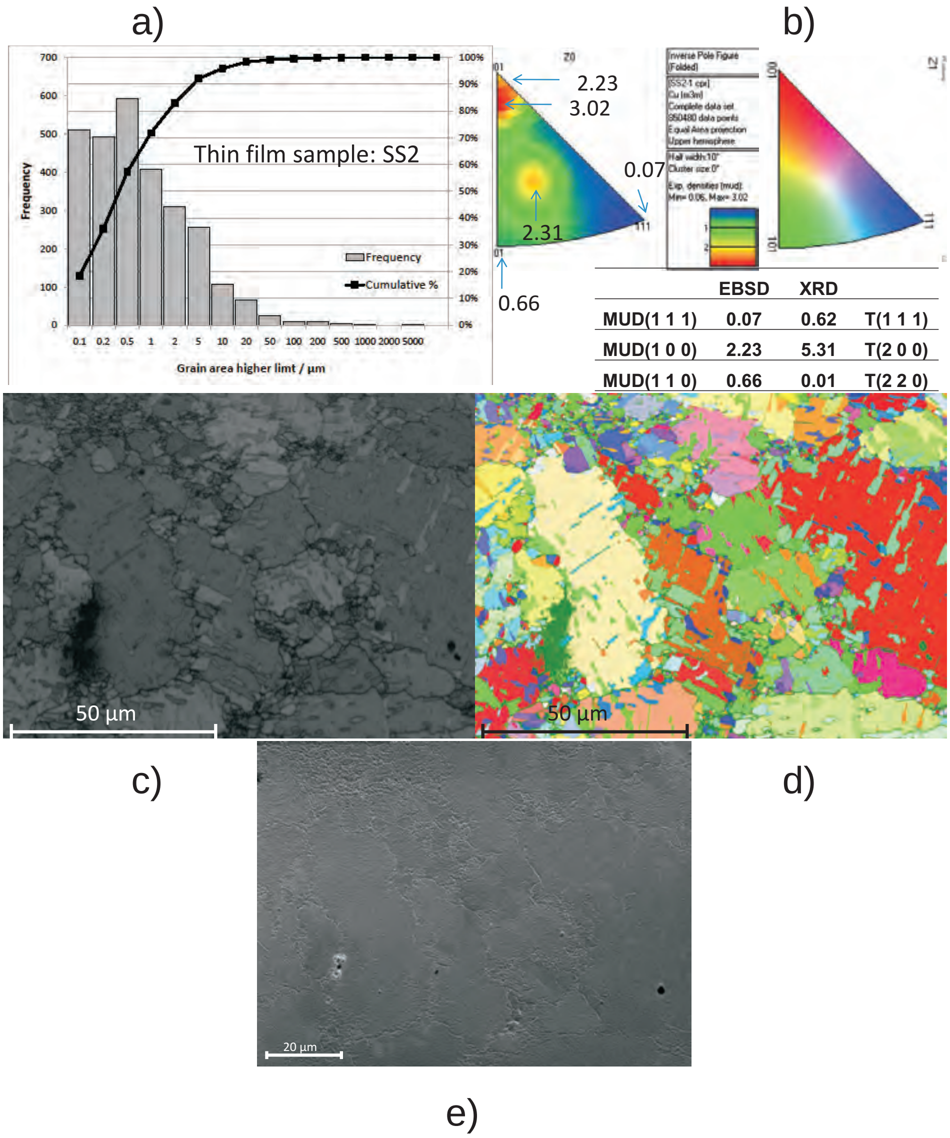

	EBSD	XRD	
MUD(1 1 1)	0.07	0.62	T(1 1 1)
MUD(1 0 0)	2.23	5.31	T(2 0 0)
MUD(1 1 0)	0.66	0.01	T(2 2 0)

Figure A.6.: Combination of results of thin film characterisation. Sample SS2: a) logarithmic grain area distribution. b) inverse pole figure (color–orientation code) and texture results: inverse pole figure density distribution (MUD factor) and XRD data. c) image–quality map. d) grain map. e) SEM picture

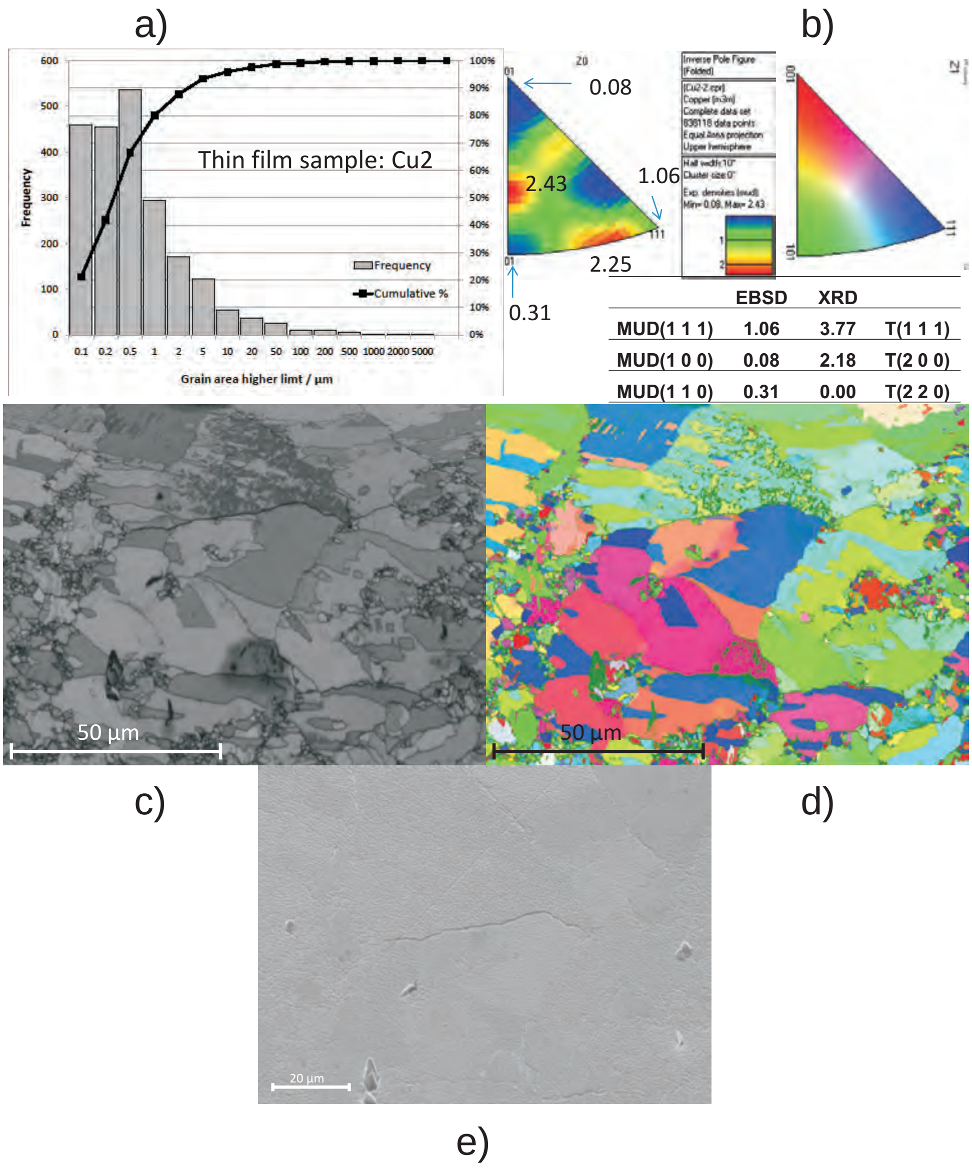

	EBSD	XRD	
MUD(1 1 1)	1.06	3.77	T(1 1 1)
MUD(1 0 0)	0.08	2.18	T(2 0 0)
MUD(1 1 0)	0.31	0.00	T(2 2 0)

Figure A.7.: Combination of results of thin film characterisation. Sample Cu2: a) logarithmic grain area distribution. b) inverse pole figure (color–orientation code) and texture results: inverse pole figure density distribution (MUD factor) and XRD data. c) image–quality map. d) grain map. e) SEM picture

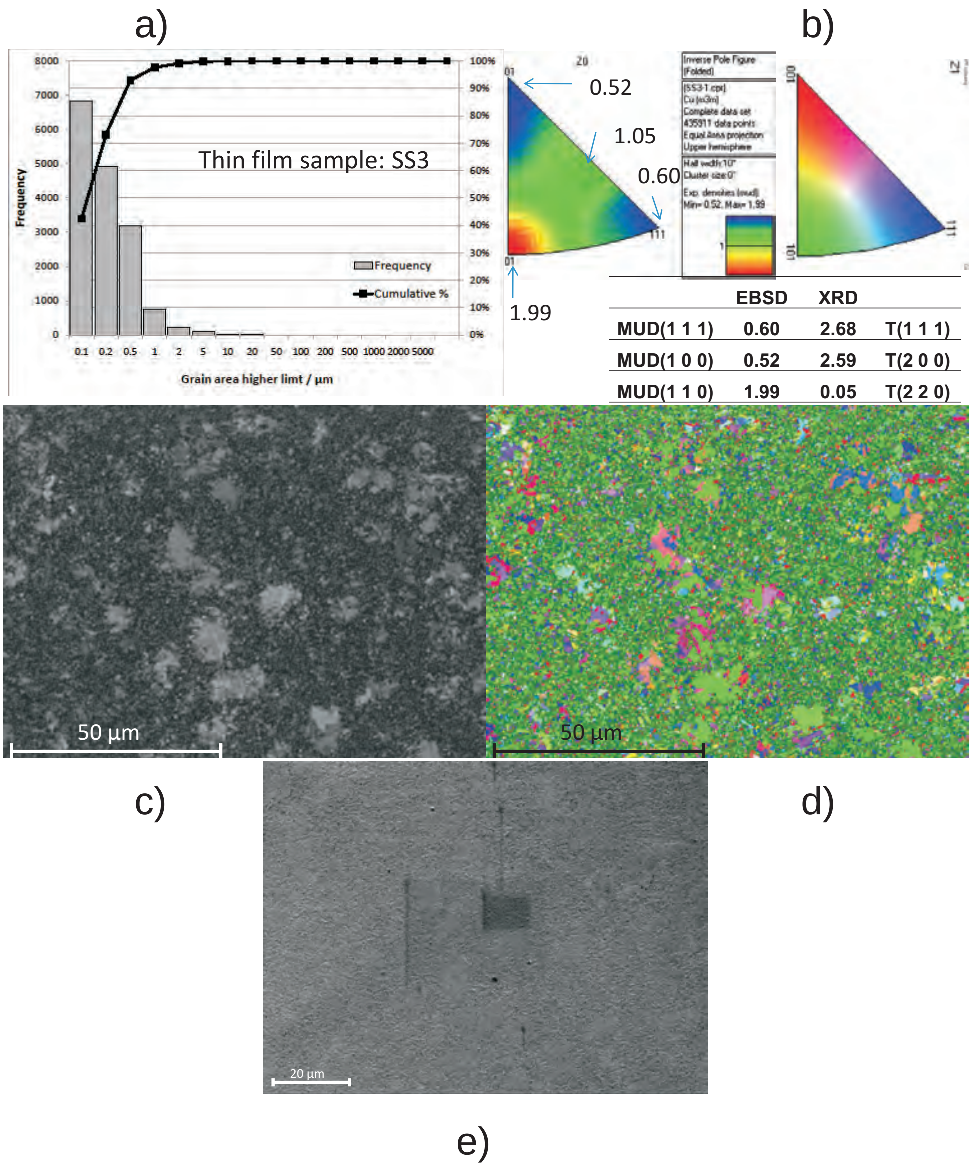

	EBSD	XRD	
MUD(1 1 1)	0.60	2.68	T(1 1 1)
MUD(1 0 0)	0.52	2.59	T(2 0 0)
MUD(1 1 0)	1.99	0.05	T(2 2 0)

Figure A.8.: Combination of results of thin film characterisation. Sample SS3: a) logarithmic grain area distribution. b) inverse pole figure (color–orientation code) and texture results: inverse pole figure density distribution (MUD factor) and XRD data. c) image–quality map. d) grain map. e) SEM picture

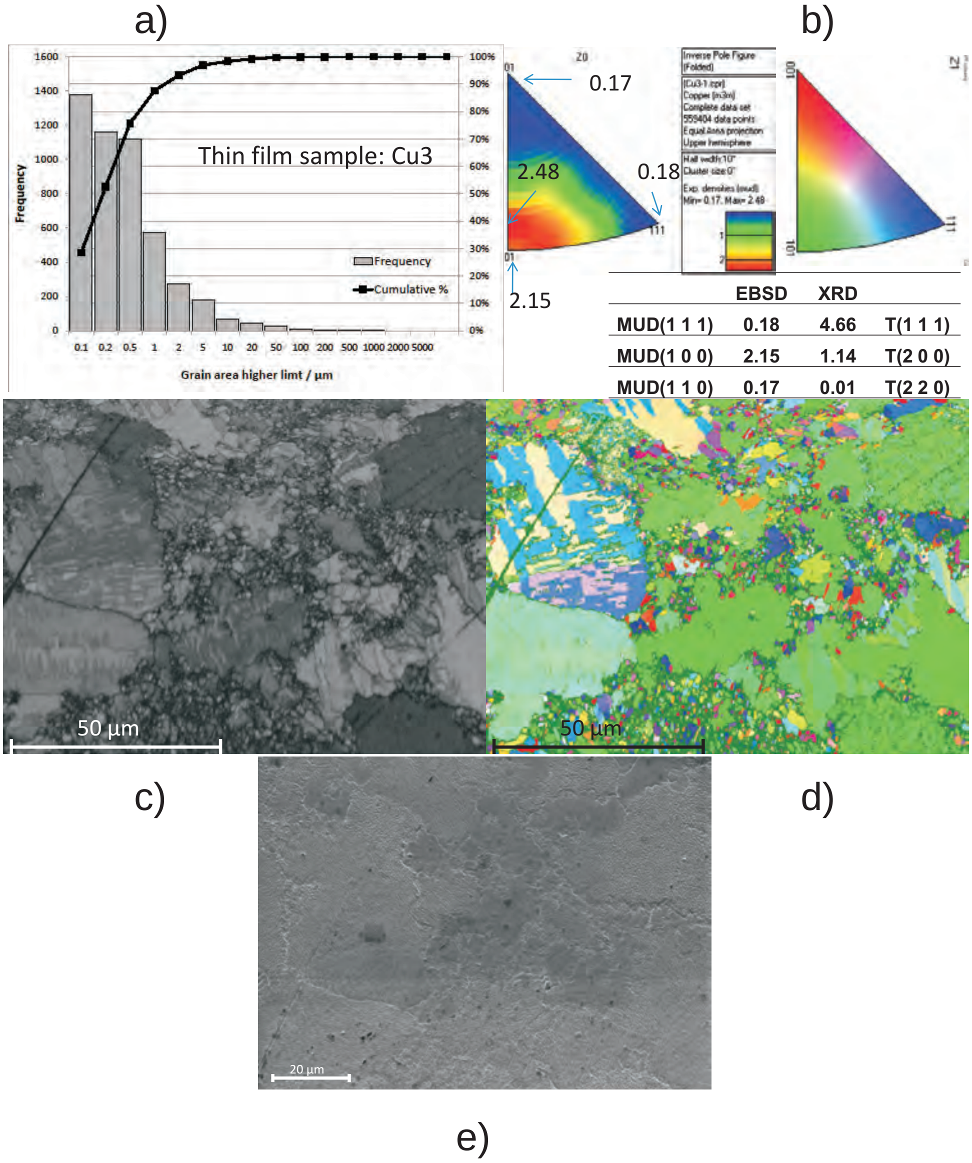

	EBSD	XRD	
MUD(1 1 1)	0.18	4.66	T(1 1 1)
MUD(1 0 0)	2.15	1.14	T(2 0 0)
MUD(1 1 0)	0.17	0.01	T(2 2 0)

Figure A.9.: Combination of results of thin film characterisation. Sample Cu3: a) logarithmic grain area distribution. b) inverse pole figure (color–orientation code) and texture results: inverse pole figure density distribution (MUD factor) and XRD data. c) image–quality map. d) grain map. e) SEM picture

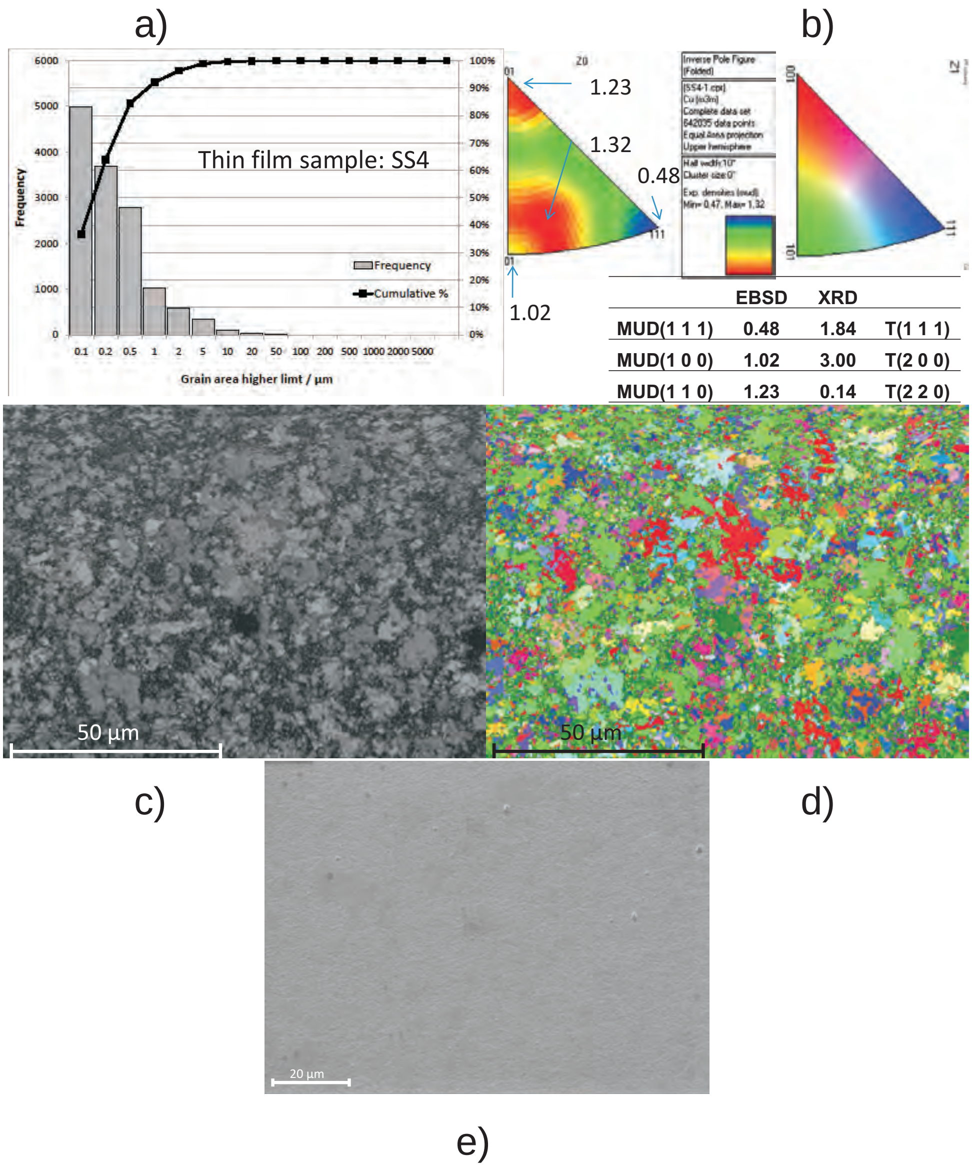

	EBSD	XRD	
MUD(1 1 1)	0.48	1.84	T(1 1 1)
MUD(1 0 0)	1.02	3.00	T(2 0 0)
MUD(1 1 0)	1.23	0.14	T(2 2 0)

Figure A.10.: Combination of results of thin film characterisation. Sample SS4: a) logarithmic grain area distribution. b) inverse pole figure (color–orientation code) and texture results: inverse pole figure density distribution (MUD factor) and XRD data. c) image–quality map. d) grain map. e) SEM picture

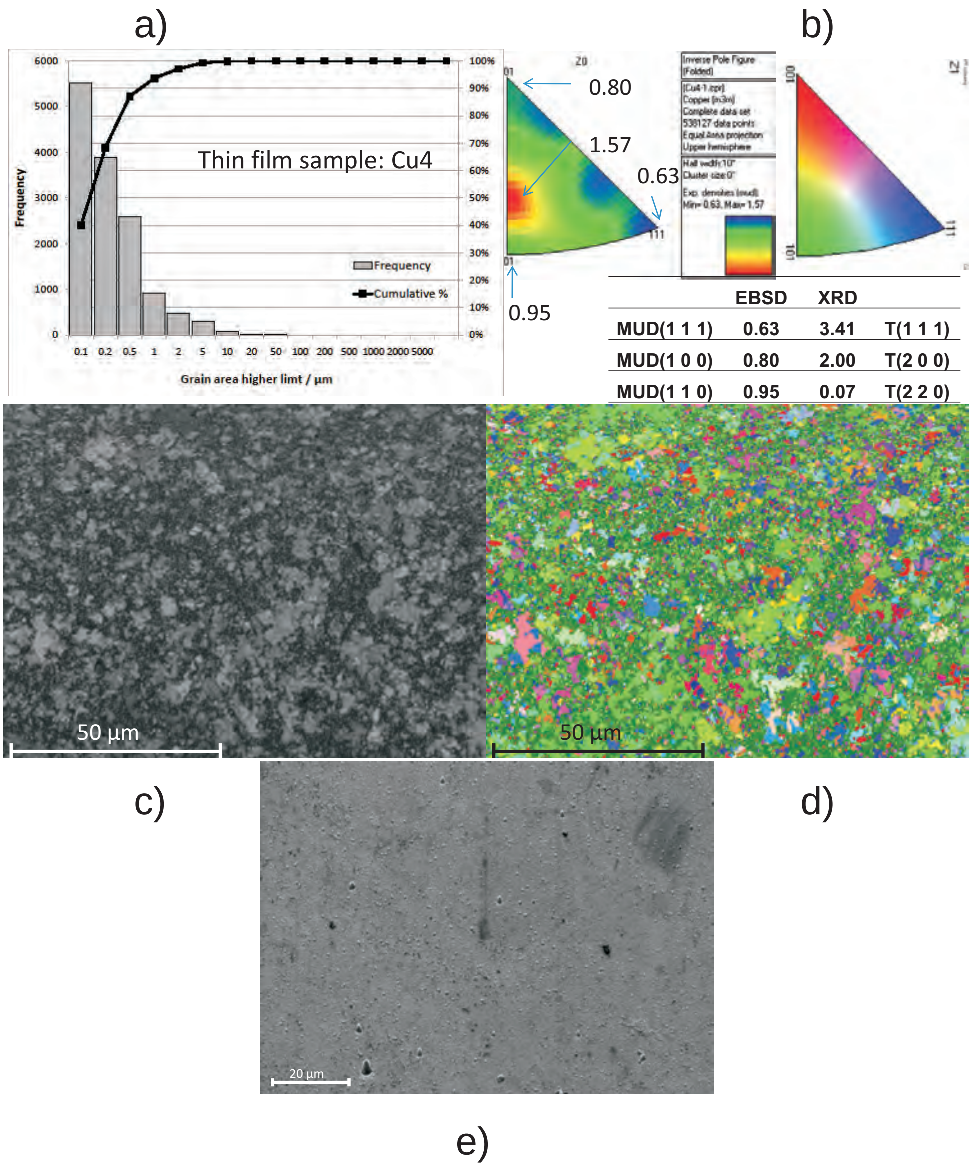

	EBSD	XRD	
MUD(1 1 1)	0.63	3.41	T(1 1 1)
MUD(1 0 0)	0.80	2.00	T(2 0 0)
MUD(1 1 0)	0.95	0.07	T(2 2 0)

Figure A.11.: Combination of results of thin film characterisation. Sample Cu4: a) logarithmic grain area distribution. b) inverse pole figure (color–orientation code) and texture results: inverse pole figure density distribution (MUD factor) and XRD data. c) image–quality map. d) grain map. e) SEM picture

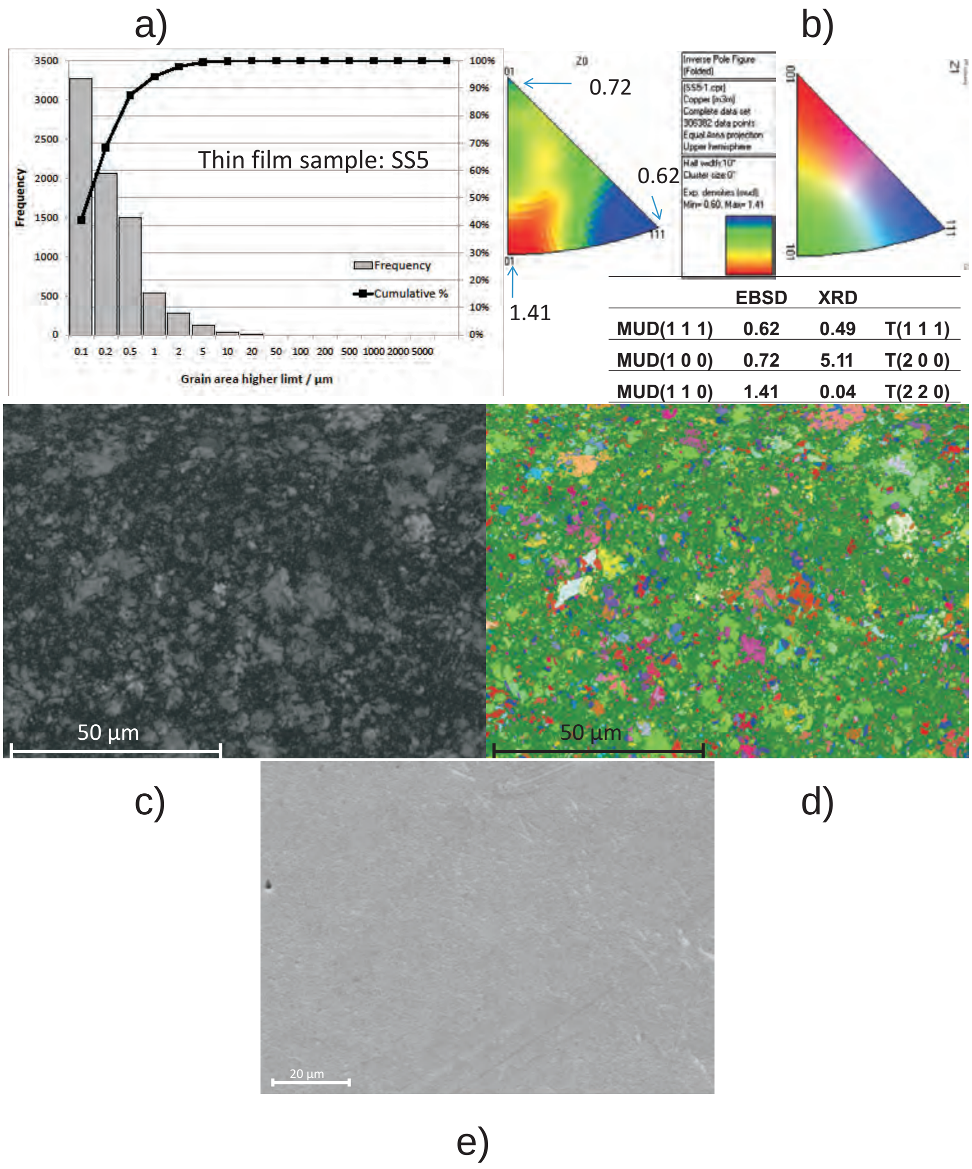

	EBSD	XRD	
MUD(1 1 1)	0.62	0.49	T(1 1 1)
MUD(1 0 0)	0.72	5.11	T(2 0 0)
MUD(1 1 0)	1.41	0.04	T(2 2 0)

Figure A.12.: Combination of results of thin film characterisation. Sample SS5: a) logarithmic grain area distribution. b) inverse pole figure (color–orientation code) and texture results: inverse pole figure density distribution (MUD factor) and XRD data. c) image–quality map. d) grain map. e) SEM picture

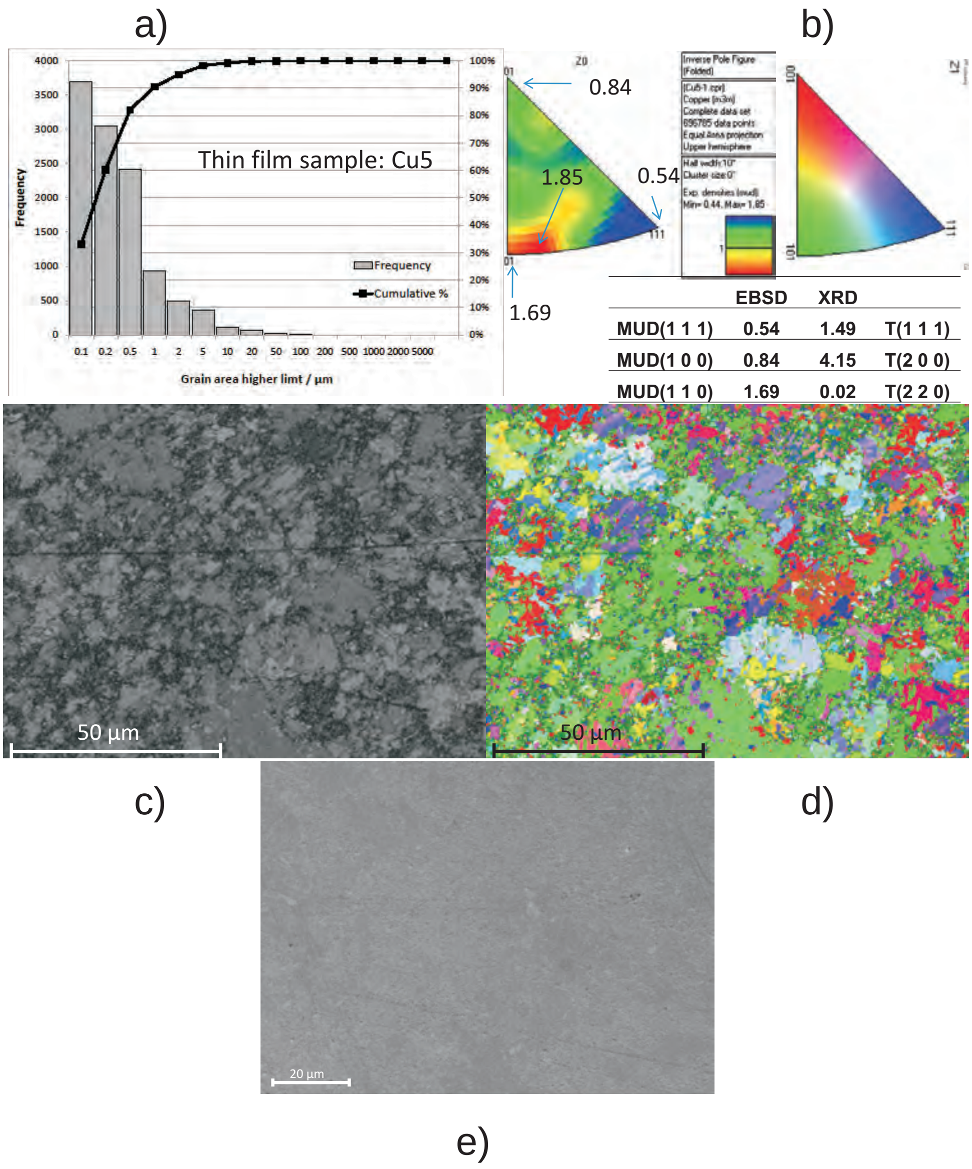

	EBSD	XRD	
MUD(1 1 1)	0.54	1.49	T(1 1 1)
MUD(1 0 0)	0.84	4.15	T(2 0 0)
MUD(1 1 0)	1.69	0.02	T(2 2 0)

Figure A.13.: Combination of results of thin film characterisation. Sample Cu5: a) logarithmic grain area distribution. b) inverse pole figure (color–orientation code) and texture results: inverse pole figure density distribution (MUD factor) and XRD data. c) image–quality map. d) grain map. e) SEM picture

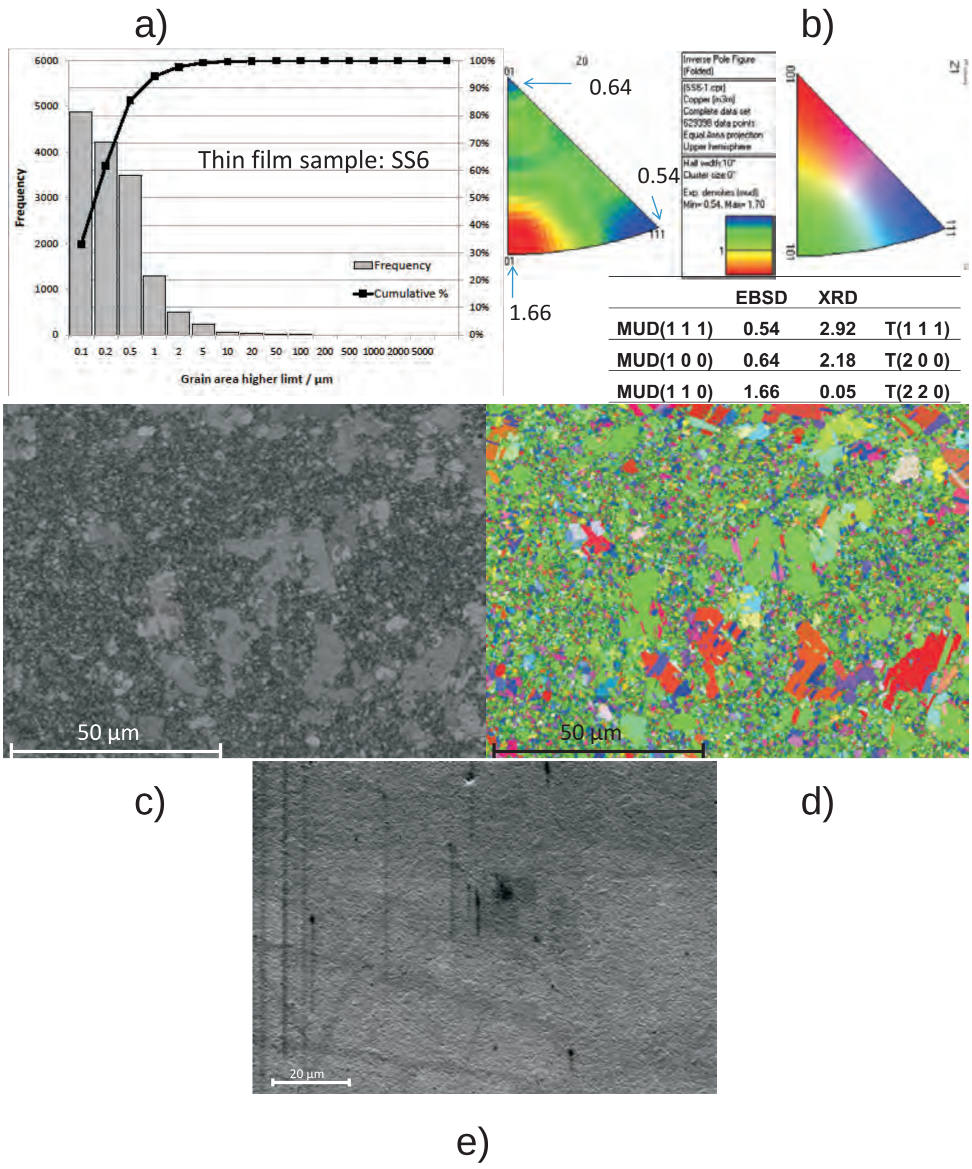

	EBSD	XRD	
MUD(1 1 1)	0.54	2.92	T(1 1 1)
MUD(1 0 0)	0.64	2.18	T(2 0 0)
MUD(1 1 0)	1.66	0.05	T(2 2 0)

Figure A.14.: Combination of results of thin film characterisation. Sample SS6: a) logarithmic grain area distribution. b) inverse pole figure (color–orientation code) and texture results: inverse pole figure density distribution (MUD factor) and XRD data. c) image–quality map. d) grain map. e) SEM picture

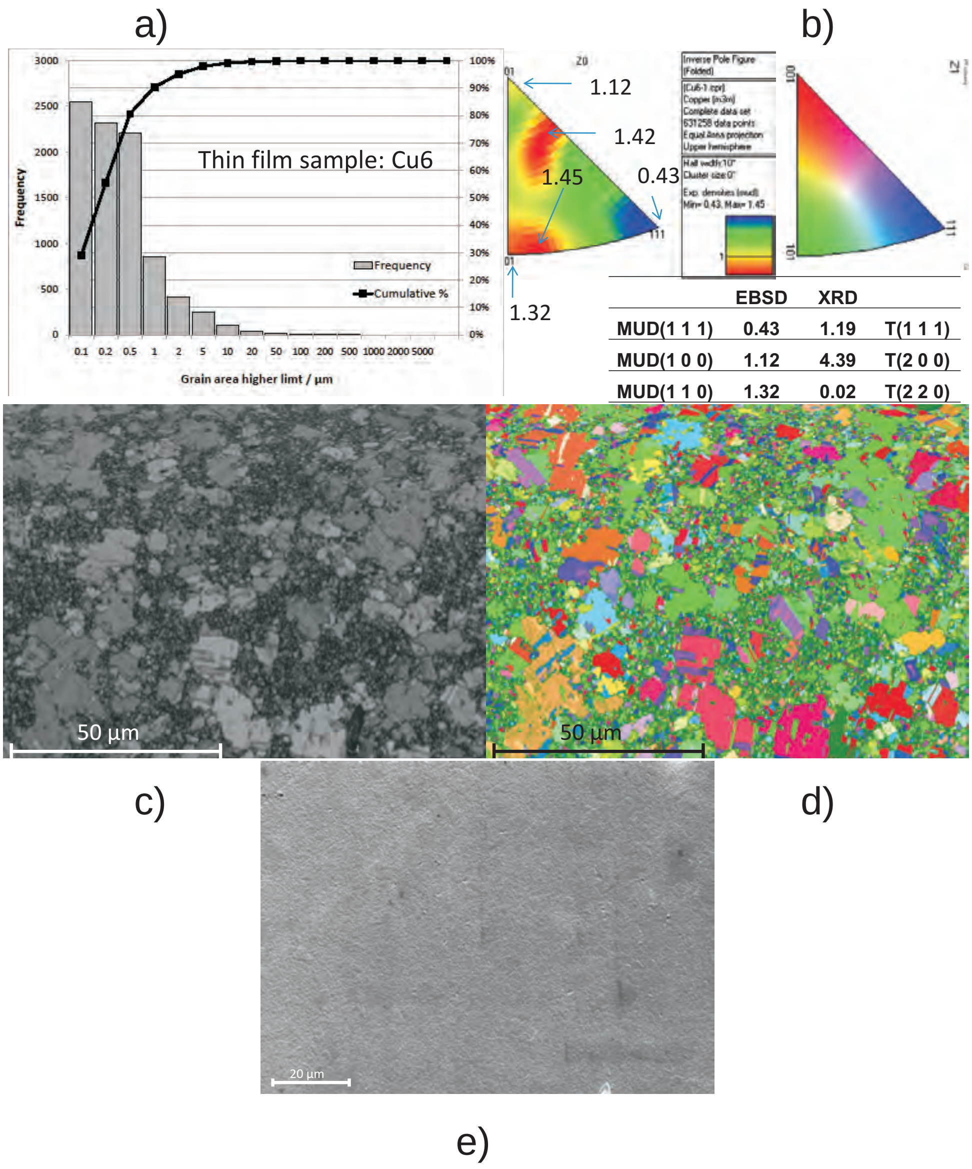

	EBSD	XRD	
MUD(1 1 1)	0.43	1.19	T(1 1 1)
MUD(1 0 0)	1.12	4.39	T(2 0 0)
MUD(1 1 0)	1.32	0.02	T(2 2 0)

Figure A.15.: Combination of results of thin film characterisation. Sample Cu6: a) logarithmic grain area distribution. b) inverse pole figure (color–orientation code) and texture results: inverse pole figure density distribution (MUD factor) and XRD data. c) image–quality map. d) grain map. e) SEM picture